The Development of an In-situ TEM Technique for Studying Corrosion Behavior as Applied to Zirconium-based Alloys

A Thesis

Submitted to the Faculty

of

Drexel University

by

Wayne Harlow

in partial fulfillment of the

requirements for the degree

of

Doctor of Philosophy

June 2017

Dedications

Dedicated to my parents, for their love and support through the arduous PhD process. To Amber, for all of her love and patience as we progressed through this adventure together.

Acknowledgements

The author acknowledges Dr. Arthur Motta for supplying the zirconium samples used in this work, Dr. Craig Johnson for his invaluable help and training for the microscopy work, and the members of the DCG for their support through the PhD process. Especially Andrew Lang for his help with EELS and other TEM, and Matthew Hartshorne for the helpful discussions and being a sounding board for my crazy ideas. The author would also like to acknowledge the DOE NSUF program for supporting this research for the bulk of the work presented here.

Table of Contents

List of Tables

List of Figures

Abstract

The Development of an In-situ TEM Technique for Studying Corrosion Behavior as Applied to Zirconium-based Alloys
Wayne Harlow
Mitra L. Taheri, Ph.D.

Zirconium-based alloys are a commonly used material for nuclear fuel rod cladding, due to its low neutron cross section and good corrosion properties. However, corrosion is still a limiting factor in fuel rod lifespan, which restricts burn up levels, and thus efficiency, that can be achieved. While long-term corrosion behavior has been studied through both reactor and autoclave samples, the oxide nucleation and growth behavior has not been extensively studied.

This work develops a new technique to study the initial stages of corrosion in zirconium-based alloys and the microstructural effects on this process by developing an environmental cell system for the TEM. Nanoscale oxidation parameters are developed, as is a new FIB technique to support this method. Precession diffraction is used in conjunction with in-situ TEM to observe the initial stages of corrosion in these alloys, and oxide thickness is estimated using low-loss EELS. In addition, the stress stabilization of tetragonal ZrO_2 is explored in the context of sample preparation for TEM.

It was found that in-situ environmental TEM using an environmental cell replicates the oxidation behavior observed in autoclaved samples in both oxide structure and phases. Utilizing this technique, it was shown that cracking of the oxide layer in zirconium-based alloys is related to oxide relaxation, and not thermal changes. The effect of secondary phase particles on oxidation behavior did not present significant results, however a new method for studying initial oxidation rates using low-loss EELS was developed.

1 Introduction and Background

As the push for green energy sources in the United States continues, there has been a rejuvenation of interest in nuclear energy as a reliable baseline energy source. This has led to a push for an increase in the efficiency of existing Generation III reactors and for construction and design of new reactors as was indicated in the 2002 Department of Energy's Technology Roadmap for Generation IV Nuclear Energy Systems[1] and more recently discussed in the DOE-NE Light Water Reactor Sustainability Program and EPRI Long Term Operations Program-Joint Research and Development Plan[2]. This is well illustrated by the construction of two Generation III+ AP1000 reactors in Georgia, which were approved by the NRC in 2012 with expected completion dates on 2019 and 2020 for the reactors. These reactors are the first new reactors built and approved by the NRC since the Three Mile Island nuclear accident in 1979.

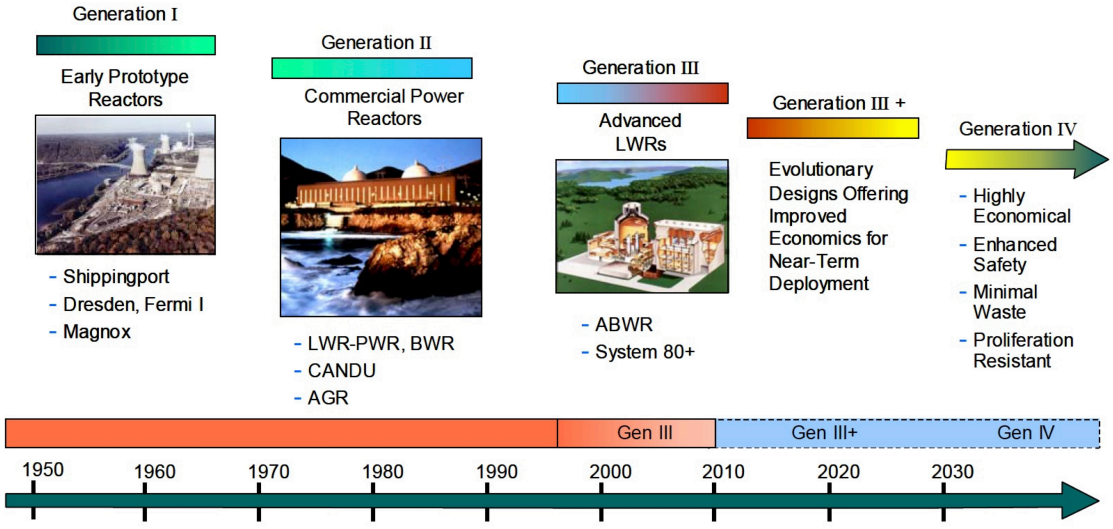

Figure 1: The Generation IV Roadmap as laid out by the Department of Energy[1].

However, in many cases, improved efficiency is the result of a harsher service environment, such as increased temperature, pressures, or water chemistry modification. These harsher in-service environments lead to an increase in material degradation through corrosion, stress corrosion cracking, swelling, and many other mechanisms, all of which limit service lifetime for various reactor components. In the case of fuels, one of the major limiting factors for burn up is corrosion of the fuel rod cladding.

Zirconium-based alloys have a long history of service as the cladding material for nuclear fuel rods, with these alloys serving as cladding materials as early as the 1960's[3]. Initially, stainless steels were used for fuel rod cladding; however, zirconium-based alloys replaced stainless steels, as these alloys still had good corrosion resistance, while also having a much lower neutron capture cross-section. This lower neutron capture cross-section is beneficial because it increases the neutron economy within the reactor core. The success of zirconium-based alloys for use as fuel rod cladding has lead to continuous research and development to improve these alloys, resulting in improved cladding performance.

While a large number of studies have been conducted, and zirconium-based alloys have long served well as fuel rod cladding, the recent Fukushima incident shows the importance of better understand the corrosion behavior of fuel rod cladding and the improvements needed. Although limited information is currently available on this accident, one of the theories about the cause of the explosions that damaged the containment structures revolves around rapid corrosion of the fuel rod cladding that resulted from the reactor cores being flooded with seawater as emergency cooling. Hydrogen is a by product of the corrosion of zirconium-based alloys, and it is thought that the hydrogen released during the rapid oxidation of the fuel rod cladding may have

accumulated in the structures, leading to the explosions that damaged the reactor containment[4]. This is not an unexpected phenomenon however, as the dangers of such a reaction were reported by Oak Ridge National Lab in 1962[3]. In addition, the long-term fuel rod service lifetime is still limited to some extent by corrosion, and corrosion also affects the storage of the fuel rod after it is removed from a reactor.

Finally, as efforts are made to increase nuclear reactor efficiency, a better understanding of the corrosion behavior of these alloys is necessary to help increase fuel service lifetimes and to allow for use in harsher environments that are dictated to achieve these higher burn-ups. In particular, proposed Generation IV reactors are expected to operate at higher temperatures that will accelerate corrosion, which in turn will limit fuel in-service lifetimes[5]. As such, many efforts have been aimed at improving the corrosion resistance of zirconium-based alloys. Almost all of these studies have focused on the long-term oxidation behavior and on the effect of alloying elements. The effect of microstructure has been studied to a limited extent, but only in the context of heat-treatment effects on long-term corrosion behavior. Presented in this thesis is a study of the uniform oxidation behavior of zirconium-based alloys by developing an in-situ TEM technique to observe the effect of different microstructural features on the initial corrosion behavior of these alloys.

1.1 Grain Boundaries and Grain Boundary Engineering

Grain boundaries are well known to have significant effects on a wide variety of material properties, and thus these properties can be controlled with grain boundary engineering.

Grain boundaries are the intersection of two different crystallographic orientations. These intersections are of importance, as the crystal structure is disordered from the matrix at this point. This means that boundaries have significant effects on the properties of a given material. Grain boundaries have been shown to have significant effects on material strength, corrosion resistance, fatigue resistance, and other properties[6–10]. For the purpose of this work, grain boundaries will be grouped into two categories, low angle grain boundaries (LAGBs) and high angle grain boundaries (HAGBs). Boundaries are typically separated into these two categories when the disorientation between the crystals exceeds 15°, as below 15° grain boundaries generally exhibit lower energy, as seen in figure 1[11,12].

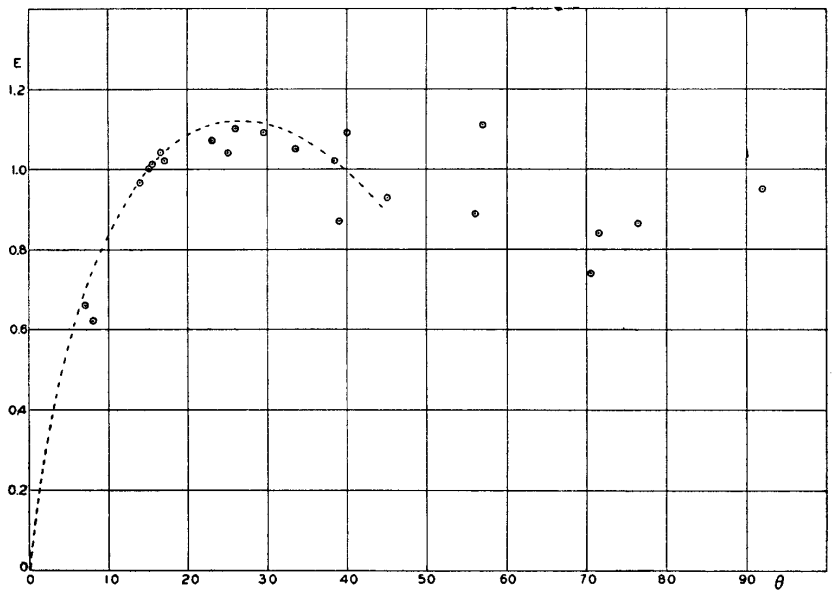

Figure 2 Graph of relative grain boundary energy versus disorientation. Solid line indicates a theoretical curve; points are from experimental data of Dunn. Figure taken from reference [11].

Grain boundary engineering (GBE) is a process first proposed by Watanabe, in which thermomechanical processing is used to control the grain boundary character

distribution within a material, which in turn has significant effects on material properties[6]. The process of grain boundary engineering is well established, with improvement in material resistance to problems such as corrosion, intergranular fracture, stress corrosion cracking, fatigue, and creep[7]. Of particular interest is corrosion resistance, which past work by Allen et. al in Incoloy 800H and Incoloy 617 has shown can be increased by using a proper GBE treatment[13]. Grain boundary engineering techniques that alter microstructure are a viable method for increasing corrosion resistance[7,13–16]. In the case of zirconium-based alloys, there is some evidence that by identifying what effect orientations and grain boundary type has on corrosion, corrosion resistance may be improved through GBE. Past work has shown that oxide growth can be correlated to the orientation of the underlying base metal[17,18]. This work was conducted on thermally grown thin films of pure single crystal zirconia, and showed there were effects arising from orientation, however the effects of grain boundary type were not explored. These effects will be discussed further in the next section. It has also been shown that in some zirconium-based alloys there is a suboxide layer that is to some extent correlated to oxide thickness, which in turn seems to show some relation to the orientation of the base metal[19].

1.2 Corrosion of Zirconium-based alloys

As mentioned above, zirconium-based alloys have long been used for fuel rod cladding material, and this use has led to extensive research into the corrosion behavior of these alloys[3,17,20–23]. In particular, the Zircaloy series of alloys have been the most widely used in reactors, with much research focusing on the oxidation behavior of Zircaloy-2 and Zircaloy-4. Zircaloy-2 and Zircaloy-4 are distinguished mainly by the lower Ni and Fe content of Zircaloy-4[3]. While these alloys possess moderate corrosion resistance,

uniform corrosion, along with the associated hydrogen pick up, remains a life-limiting factor for fuel rod service[24,25]. Zircaloy-2 is commonly used in Boiling Water Reactors (BWRs), where hydrogen pickup is less of a concern than in Pressurized Water Reactors (PWRs), in which Zircaloy-4 is more commonly found. Zircaloy-2 exhibits nodular corrosion as a result of the BWR environment, as opposed to the uniform corrosion more often seen in Zircaloy-4[21]. More recently, the Zircaloy series of alloys is being replaced

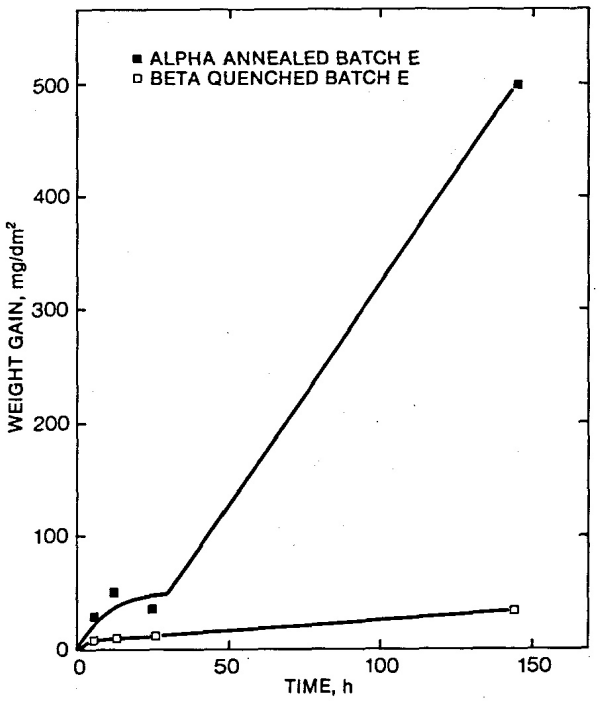

Figure 3: Weight gain versus time graph from Andersson et. al showing the improved corrosion resistance of beta quenched Zircaloy-2

with alloys such as ZIRLO and M5, which have better corrosion resistance due to the additions of niobium[20,26,27].

The in-service lifetime of fuel rods is limited by material behavior, which is very dependent on microstructure and composition. In the case of the Zircaloy family of

alloys, it has been shown that corrosion behavior is dependent on both alloying additions and on base metal phase as well as oxide structure. Past studies have shown that Zircaloys quenched to form beta-phase are more corrosion resistant than traditionally prepared Zircaloys[28–30].

Figure 3, adapted from Andersson et. al shows the improved corrosion behavior as a result of beta quenching in Zircaloy-2[28]. This is the result of a finer secondary particle size that results for the beta-quench heat treatment. The base metal microstructure has also been shown to have significant effects on the microstructure of the oxide formed during oxidation[31]. Studies have shown that crystallographic orientation has an effect on the oxidation behavior of zirconium-based alloys, with the base metal affecting the orientation of the oxide formed[18,32,33]. This is important, as this texturing determines grain boundary type in the oxide, with diffusion of oxygen through the oxide layer to the base metal being a limiting factor for oxidation rate[34–38]. It has also been shown that phenomena connected to oxidation, such as hydride formation, are very dependent on microstructure such as grain boundaries and precipitates, and in-situ TEM can be used to study the initial mechanisms resulting in hydride formation[39]. Hydride formation is a critical failure mechanism in zircoinum-based alloys as this results in greatly reduced mechanical properties, which can lead to significant difficulties not only in-service, but also during the storage of spent fuel[40]. It is directly related to oxidation behavior, because the oxidation reaction in water for zirconium-based alloys releases hydrogen as a byproduct, some of which is trapped in the alloy. As was discussed previously, Zircaloy-2 exhibits greater hydrogen pick up, and this was partially a driving force for the development and use of Zircaloy-4 with its lower Ni content helping to reduce hydrogen pick up by a factor of 3[3]. If oxidation behavior can be improved, an improvement in

hydrogen pick up can be expected because of less hydrogen produced during the oxidation process.

The oxidation behavior of these alloys has been extensively studied by a variety of methods. These methods include microbeam synchrotron diffraction[41–43], transmission electron microscopy (TEM)[32,44,45], scanning electron microscopy (SEM)[30,32,41–43,46], optical microscopy[41,47], and x-ray diffraction[43,46–48]. These techniques have provided an extensive knowledge base for the morphology and structure of the oxides formed on these alloys, including cracking behavior[41,44], crystal structure[41,43,44,46], and the start of breakaway corrosion[5,49].

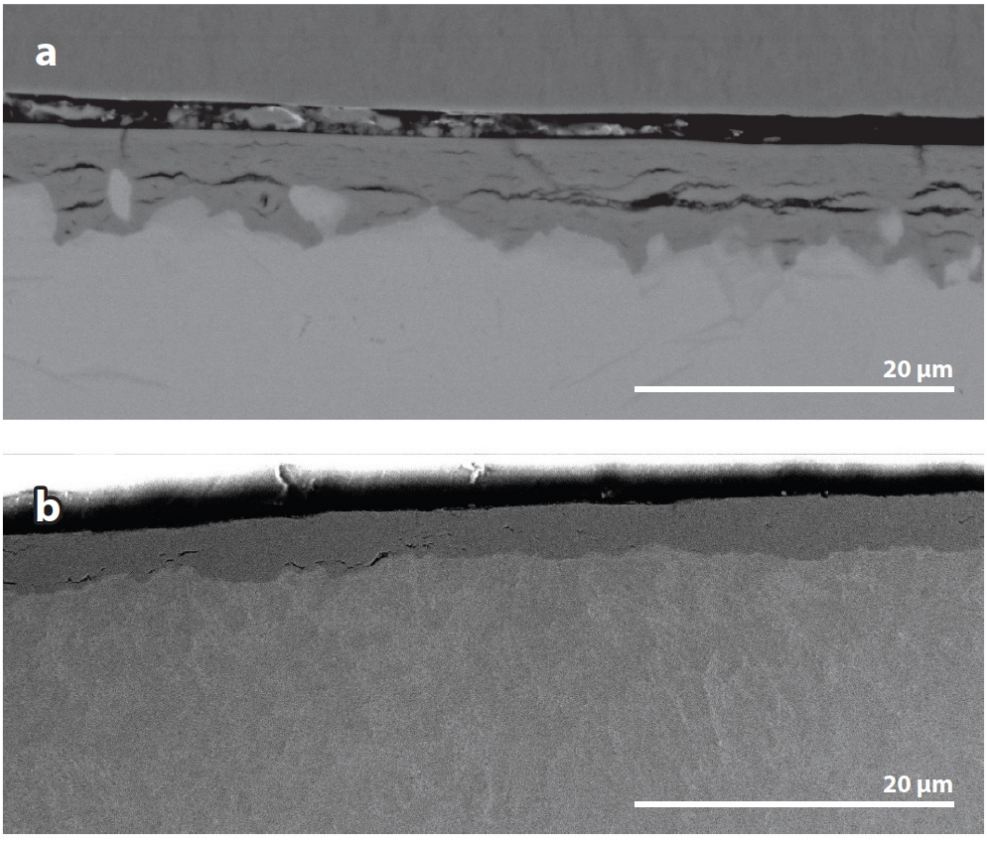

Figure 4: Figured adapted from Motta et. al[50] illustrating cracking behavior of the oxide in pure zirconium(A) and Zircaloy-4 (B).

The majority of these experiments, however, have been done using autoclave or reactor corroded samples, which has not allowed for the study of the initial steps of corrosion. However, this extensive work has allowed for the identification of the rate-limiting step in oxidation in zirconium-based alloys as oxygen diffusion into the base metal using techniques such as NanoSIMS combined with tracer elements of O^{1851}. What is still unclear is exactly which features act to have the greatest effect on oxidation behavior by affecting diffusion of oxygen. In long-term oxidation, features such as oxide cracking, illustrated in figure 4 adapted from Motta et. al[50], significantly influence corrosion rate by providing fast diffusion paths. In figure 4 A, large cracks and the start of delamination of the oxide are readily apparent, whereas in B, the alloyed Zircaloy-4 samples shows greatly reduced cracking and a more adherent oxide layer. While the oxide structure on long-term corroded zirconium-based alloys is known to be composed of both of tetragonal and monoclinic ZrO_2, the structure of the first stage of oxide is not yet known along with the effects on oxidation behavior as a result of the effect it has on diffusion. This information is valuable, as it is thought that the denser tetragonal ZrO_2 may provide a more protective oxide than monoclinic ZrO_2. Some authors cite the denser tetragonal ZrO_2 layer as an explanation for the rate change in oxidation between initial stages showing parabolic behavior and later stages showing cubic oxidation rates. A schematic for weight gain versus time in this manner is shown in figure 5 as adapted from Gosmain et al.

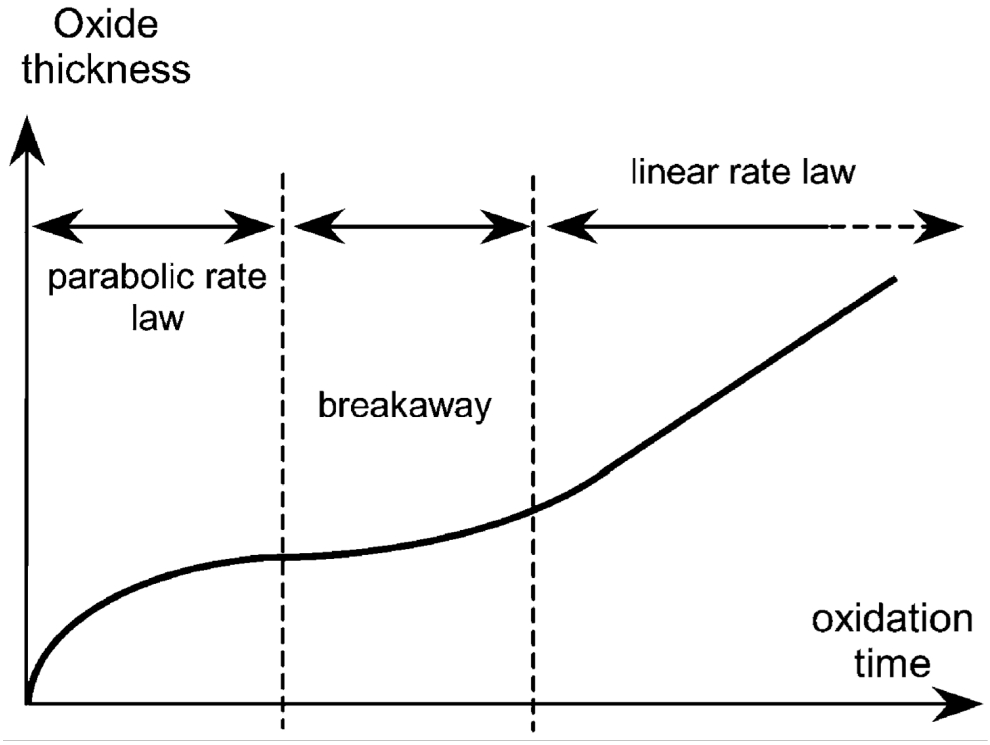

Figure 5: Weight gain verse oxidation schematic adapted from Gosmain et. al[52] illustrating one predicted oxidation route.

Other authors claim that a different oxidation route takes place, with a cyclic oxidation process occurring, where by each time a tetragonal ZrO_2 layer forms, oxidation rate decreases, then rapidly increases again once the tetragonal phase layer becomes too thick and relaxes into monoclinic ZrO_2. This cyclic oxidation behavior has been seen in a variety of long-term tests[41,53–55]. In the figure below, a schematic from Motta et. al[50] of this cyclic type behavior is shown in red versus other zirconium systems, particularly the non-protective pure zirconium in purple.

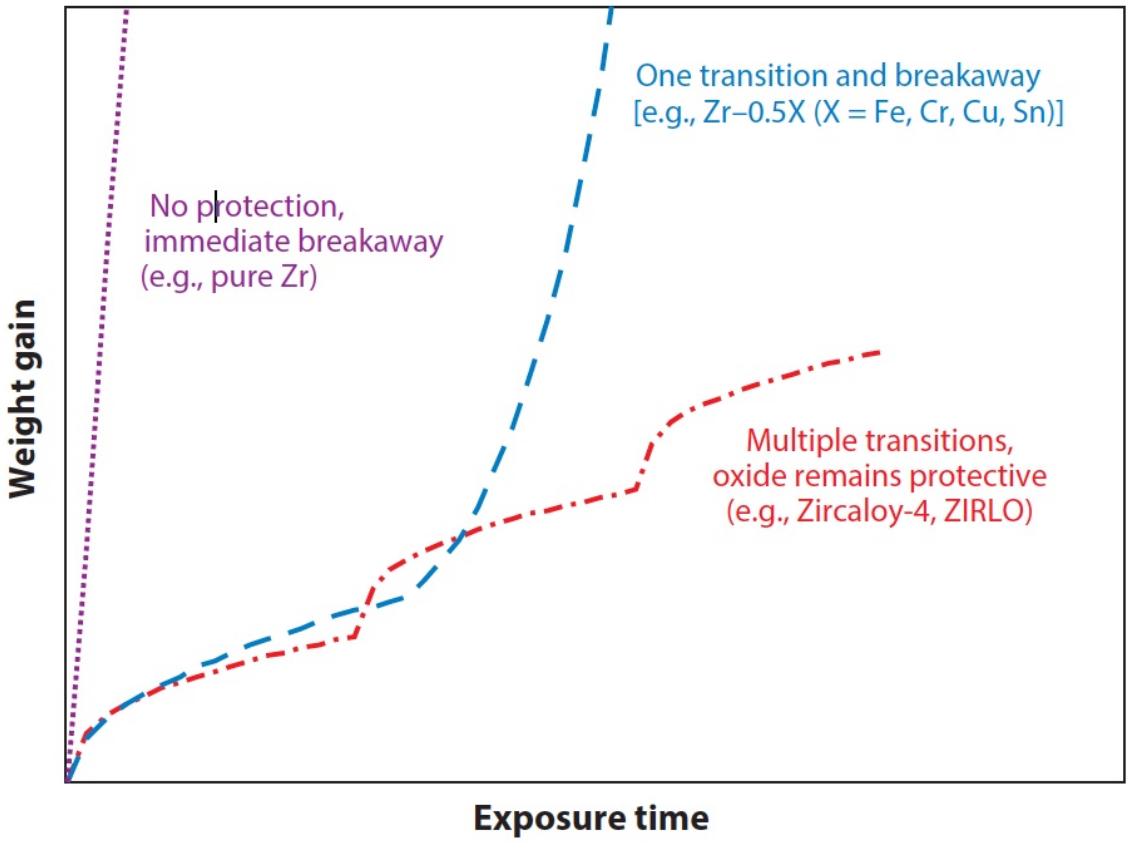

Figure 6: Figure adapted from Motta et. al[50] showing proposed cyclic type oxidation behavior for Zircaloy-4 and similar alloys versus other zirconium systems.

It is known that the oxide structure formed on zirconium-based alloys is highly textured, and that this may effect the corrosion rate of the base alloy[5,36,41,45]. It is thought that the texture in the monoclinc phase is the result of stress minimization, but the effect of this texture on oxidation rate is unknown[5,36]. Changes in oxide texture have also been attributed to the reformation of the protective oxide layer, but how this influences oxidation rate or which phase may be the protective phase is not discussed[41]. More recently, it has been found that more strongly textured oxides provide better corrosion resistance, and there are preferred growth directions in both monoclinic and tetragonal oxides[45]. Ploc complied data from a variety of authors and showed that there is a

correlation between oxide thickness and Zr orientation, with certain directions showing a preference for thicker oxides, however this work was focused on the epitaxial relationship of the oxide to the base metal[18]. Both Ploc and Glavicic revealed orientation relationships between the oxide and the base metal, and more recently, Garner et al found that oxidation rate may be partially controlled by oxide structure[18,31,45].

As time has progressed, a variety of zirconium-based alloys have been produced and tested for long-term oxidation behavior. Some of these alloys, such as those with niobium content have been found to have exceptional corrosion resistance, and have proceeded into use in industry under a variety of names, with ZIRLO and M5 being common. However, the exact effect of alloying elements on oxidation behavior is not well understood. Tin is a good example of a thoroughly characterized alloying addition, and is well known to have a negative effect on corrosion, but is still present in most alloys because of the significant gains in mechanical properties this alloying element provides through solid solution strengthening[56–59]. Recent work has shown using X-ray absorption near-edge structure that the role of tin may be fairly complex, helping to both stabilize tetragonal ZrO_2 but also based on oxidation state, provide additional oxygen vacancies promoting further oxidation[56]. Other work using atom probe tomography has shown that tin segregates to oxide grain boundaries, which combined with the observation above regarding oxidation state, may further enhance oxygen diffusion to the base metal to continue the corrosion process[60]. Other alloying elements, such as iron and chromium, are not as well understood, with significant challenges being presented by the very low alloying concentrations of these elements combined with their precipitation as secondary phase particles. When atom probe is used, there is limited opportunity to have one of these particles in the data set because of the very small sample size. In pure zirconium

samples where there is insufficient iron present to precipitate out, atom probe tomography has shown that iron does segregate to grain boundaries in the base metal, raising the question of this elements effect on oxidation behavior[60].

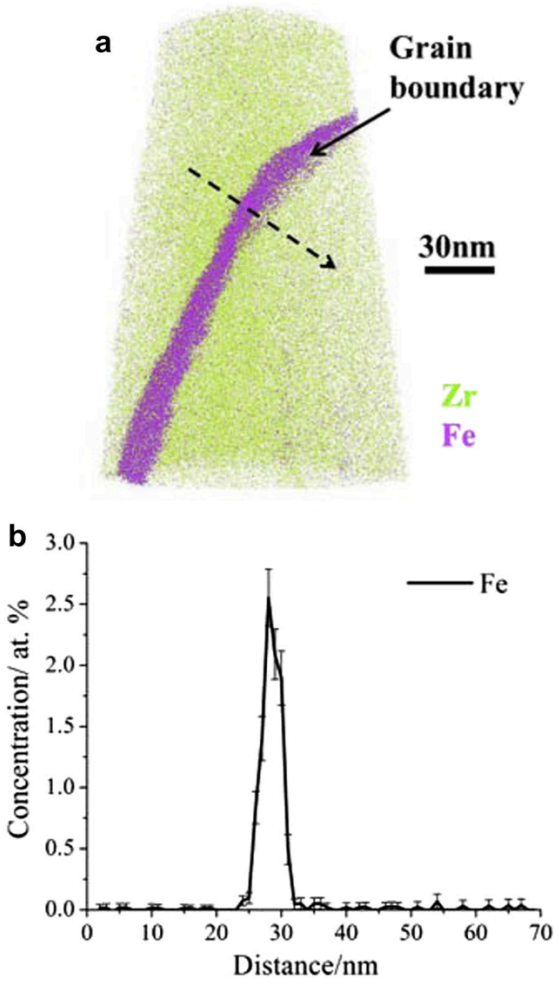

Figure 7: APT image from Dong et. al showing iron segregation in pure zirconium.

Long-term studies of the effect of transition elements have been conducted, but these tests have almost exclusively focused on improving corrosion performance, and not on the exact mechanism by which the performance is improved. Recently, it has been shown that for very long tests, corrosion performance is improved with increasing additions of

iron, chromium and vanadium, but that there is a dependence of performance on a multitude of factors including environment, tin content, and precipitate size[61]. Thus, it is critical that a method for studying initial corrosion behavior and the effect of secondary phase particles on this behavior be developed.

1.3 Environmental Transmission Electron Microscopy

Transmission electron microscopy (TEM) has been a common technique for characterizing materials since its invention in the 1930s. One major limitation of TEM is the requirement for high vacuum in the column in order for the electrons to pass through the sample being examined without interacting with gas molecules and to support the high voltage electron gun. This high vacuum requirement means that samples to be examined must be under high vacuum, which can significantly alter some samples, particularly polymer and organic samples. In addition, great insight can be had into material behavior by applying stimuli to a sample inside the microscope and observing how the sample responds, but high vacuum hinders examination of samples response to much beyond simple heating, cooling, or biasing conditions. Thus, attempts to create an Environmental TEM (ETEM) have been constant since the invention of the TEM, only recently have these efforts resulted in an efficient and workable system. Sharma and Gai have both been leaders in this field, having modified TEMs that were commercially available into ETEMs. This was done through the approach of differential pumping, which was one of the first methods used to attempt to create an ETEM[62]. A schematic of a dedicated ETEM is shown in figure 6, as adapted from Wagner et. al[63].

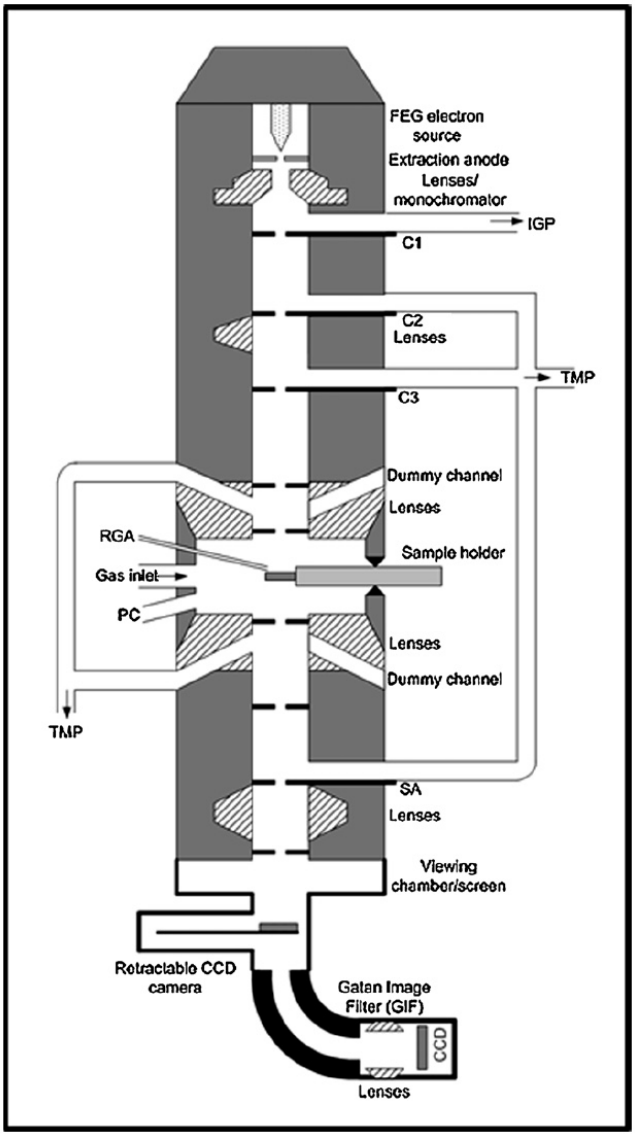

Figure 8: Schematic showing a typical differentially pumped ETEM design. Figured adapted from Wagner et. al[63].

In this method, the sample area is isolated by two pairs of apertures, with the pair closer to the sample having smaller holes, and the pair farther from the sample having larger holes[64–66]. The exact diameter of the apertures used is determined by a combination of the gas pressure that is to be used and the pumping rate[66]. Either a turbo molecular pump or a molecular drag pump is connected between the apertures to provide pumping

to remove gas from the column so that the vacuum needed for the electron gun can be maintained[63,67]. Modifications similar to these had been done previously; however, the modifications made by Gai et. al. were to the entire TEM column of a Philips CM 30T, instead of just modifying part of the column and were considered to be permanent[68]. In addition, the pole piece used in this TEM was custom made so as to allow for differential pumping to not interfere with imaging[69]. These modifications led to the development of the currently available environmental TEM from FEI[67].

Environmental holders have also had a long history of development. Instead of relying on differential pumping as is the case of dedicated ETEMs, environmental holders use the window method to contain the environment to the sample and allow the required vacuum to be held on the TEM column. These holders have two electron transparent windows, one on top and one on bottom, which have to be sufficiently strong to survive the pressure difference between the inside and outside of the cell with only slight deflection. Figure 7 below shows a schematic of a cell type design, and how the system seals from the high vacuum of the microscope column using windows.

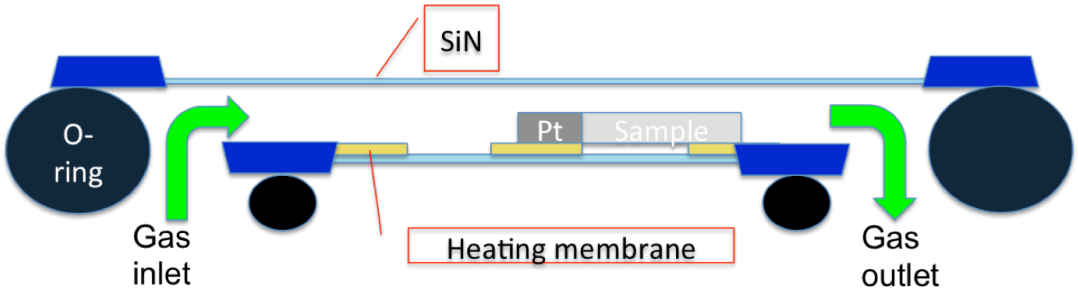

Figure 9: Schematic showing the tip arrangement in a dedicated environmental holder design that allows for sealing from the TEM column vacuum.

These windows are usually constructed of either thin carbon sheets or silicon nitride. Early attempts to construct cells of this design were conducted to study wet biological systems[70]. These attempts proved to have several problems, including window integrity and scattering of the electron beam until too little intensity was present for imaging[64,70]. The widespread use of high energy TEMs, operating at 1MeV solved this problem, but beam damage to the samples being studied was the result[65,71,72]. The use of medium voltage TEMs with the large enough pole pieces to accommodate environmental holders and the use of energy filters, along with the need for liquid in situ capabilities brought renewed interest to environmental holders[72]. This interest led to the development of new holders, using MEMS technology, which allowed for miniaturization of the environmental cell, as well as an increase in durability of the cell[73,74]. In addition, these advances lead to holders which allowed the flowing of liquid, instead of a static liquid environment that had previously been achieved[75]. Early attempts at environmental holders needed glues to seal the cell which had to be irradiated with ultraviolet light or heated to cure, but further development removed this step, although each cell still needs to be vacuum tested prior to insertion in the TEM[75]. The success of these liquid cell systems has encouraged the development of similar gas cell systems, a schematic of which was used in figure 7 to illustrate this type of design. While gas cell systems are not yet widespread, both Protochips™ and Hummingbird Scientific™ have announced commercial gas cell systems in the last few years and E.A Fischione Instruments, Inc. provides custom made solutions, such as presented in the work of Mehraeen et al[76]. The work presented herein is using a custom designed system from Protochips, which helped form a basis of the commercially introduced system.

While both ETEMs and environmental holders have entered the commercial market, each system has its benefits and its drawbacks. Environmental holders can be used with most TEMs, without modification to the TEM, but the fragility of the windows of these holders limits the heating and cooling of the holder. A dedicated ETEM, however, allows for most available holders to be used, including heating and cooling holders, although the differential pumping apertures somewhat limit temperatures that can be used[77]. Environmental holders allow for gas pressures exceeding one atmosphere depending on window materials[65], whereas ETEMs are limited to much lower gas pressures, with most pressures reported being a few torr[72,77]. Environmental holders cannot be as well corrected as ETEMs for electron scattering because of the windows in the holder, and diffraction data is contaminated by signal from windows as well[65]. Both ETEMs and environmental holders suffer from similar problems of gases causing electron scattering, but the use of electron energy loss spectroscopy in an ETEM allows this scattering to be used to determine the composition of the gas in the ETEM if gases are being mixed in the chamber[63]. In the ETEM the use of energy dispersive x-ray (EDS) is not possible, as the detector would be contaminated by the gas in the chamber, but in an environmental holder EDS can be used, depending on holder design, as the gas is contained to the sample holder, however there is signal contamination from the windows[65,72]. Each system is susceptible to column contamination, in the ETEM this is by gases depositing on surfaces[77], and in the environmental holder this is the result of window breakage[64,68].

1.4 Research Objectives

My research was aimed at achieving the following objectives based on outstanding questions in these fields.

1) Can an in-situ TEM technique be developed to study the oxidation behavior of samples prepared from a bulk material?

This was up for debate, as many people feel that this is not a reasonable task for chip-based environmental holder design, as is evident by the abundant literature in nanoparticles in this field, and a dearth of results from samples prepared from bulk materials. Almost all work done in a similar fashion has been conducted using thermally grown thin films, which limit real world application.

2) Does this technique replicate the behavior that has been seen over the last 50 years?

One major question always present in in-situ TEM is whether the results being produced are simply from thin film effects or because of small sample size. In oxidation, especially in a system where oxygen diffusion is a limiting step, there needs to be sufficient oxygen to not change oxidation behavior, which is why an environmental cell type system and not a dedicated ETEM must be used. There is no reason to expect a different overall behavior as far as oxide phases and features, unless the sample is oxidized through thickness, which will allow for sample relaxation and removal of the stress-stabilized ZrO_2 phase. By operating at atmospheric pressure and not low pressure, there should not be effects resulting from the lack of oxygen for the reaction. The kinetics of the process must be accelerated for the purpose of in-situ TEM, however past work in a variety of different mediums including oxygen[78,79], steam[26,27,80,81], water[5,26,43], water vapor[78], air[48,82,83], has shown that changes in oxidation rate have little effect on the overall oxide structure[84].,

3) Using the above technique, where does the oxide nucleate during uniform corrosion in Zirconium-based alloys and what is the morphology of the oxide?

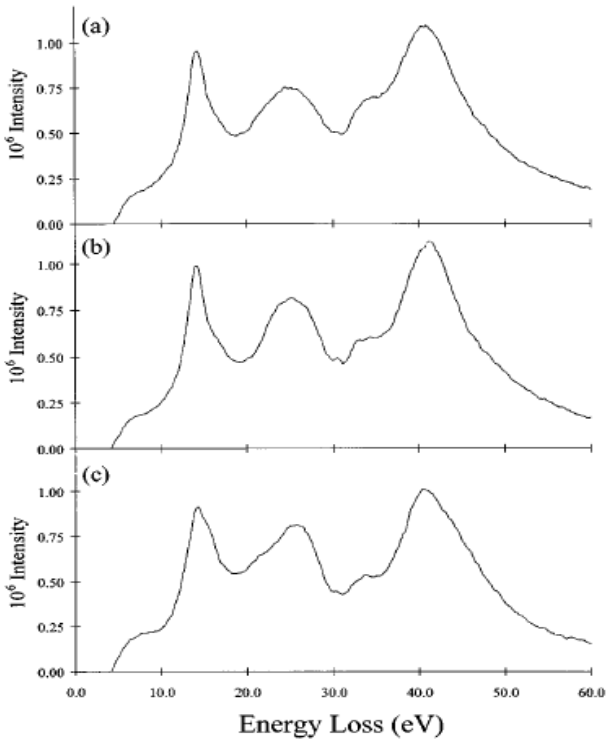

Figure 10: Image showing EELS spectra for a) cubic b)tetragonal and c) monoclinc ZrO_2 phases from McComb, 1996

The expectation is that oxide nucleation will occur at grain boundaries, as these will act as fast diffusion paths for oxygen to enter the metal[85]. In this material system, it is known that the oxidation behavior after initiation is limited by oxygen diffusion to the base metal[34–37], so it is reasonable to expect that the first oxide nuclei will appear at the grain boundaries acting as fast diffusion paths for oxygen into the metal itself. Using HAADF or EFTEM will provide additional contrast that will allow for identification of the nucleation point of the oxide. In HAADF contrast can arise from an increase in sample

thickness (expected as the oxide grows), as well as from atomic number differences in this case between oxygen and zirconium. For EFTEM a specific EELS peak is selected so that electrons of a specific energy are used to compose the image, in this case the energy can be selected based on the electrons that have interacted with oxygen. The exact phase present may either be identified using nanobeam diffraction, or more likely, EELS, with the difference between tetragonal and monoclinic ZrO_2 being small, but still detectable as seen in the figure 8[86,87].

4) What oxide phase is the initial phase, tetragonal ZrO_2 or monoclinic ZrO_2?

Monoclinic ZrO_2 will be the initial phase, as the tetragonal ZrO_2 phase is stress-stabilized[31,45,46,88,89], and the stress to stabilize this phase will be the result of the Pillings-Bedworth ratio of 1.57 for this system[90]. Thus, when the oxide is not yet uniform across the surface with grains impinging on each other to provide the stress, the non-stress dependent phase will be the phase present. Also presented will be a study into the effects of TEM sample preparation on the phase stability of tetragonal ZrO_2, as FIB prepared samples are well known to have stress relaxation[91].

Through my work developing this technique for studying the initial growth of the oxide in bulk metal systems, it maybe possible to identify factors that can reduce oxide growth rate, such as low angle grain boundaries which would allow for better alloy design through grain boundary engineering. In addition, by applying the cross section technique developed as a part of my work, it is possible to compare oxide texture if a large enough sample population is complied. A reduction in oxidation rate of fuel rods could lead to a number of benefits, such as longer in-reactor lifespan, higher burn-ups, and potentially safer storage of spent fuel. Thus, by studying the initial oxide structures and growth

mechanisms, there is great potential for improvements in material performance. To this end, this work has lead to a number of conference presentations and papers, listed below.

Conference presentations-

W. Harlow, M. L. Taheri, "In-situ TEM Study of the Initial Oxidation Behavior of Zirconium under High Humidity Environments," Materials Science and Technology 2016, October 2016

W. Harlow, M. Giordano, P. F. DeCarlo, M. L. Taheri, "Toward Predictive Geochemistry: Time Resolved, High Resolution Studies of Atmospheric Particle Transformations" ACS National Meeting, March 2016

W. Harlow, M. L. Taheri, "Comparison of Zirconium Oxidation Behavior Under Oxygen-rich gaseous and High Humidity Environments via In-Situ TEM" TMS 2016, February 2016

W. Harlow, M. L. Taheri, "In-situ TEM of the First Stages of Oxidation," Materials Science and Technology 2015, October 2015

W. Harlow, M. L. Taheri "In-situ TEM Study of the Initial Oxidation Behavior of Zry-4," Microscopy and Microanalysis annual meeting, August 2015

W. Harlow, H. Ghassemi, M. L. Taheri "Early Stage Corrosion Study of Zircaloy-4 Inside A Transmission Electron Microscope," Annual TMS meeting, Orlando, FL, March 2015

W. Harlow, H. Ghassemi, M.L. Taheri "Phase Identification in Early Stages of Corrosion in Zircaloy-4" 2014 MRS Fall Meeting and Exhibit December 2014

W. Harlow, H. Ghassemi, M. L. Taheri "In Situ TEM Study of the Corrosion Behavior of Zry-4" Microscopy & Microanalysis 2014 August 2014

Papers-

W. Harlow, M. L. Taheri, "Toward 3D Imaging of Corrosion at the Nanoscale: Cross-Sectional Analysis of In-situ Oxidized TEM Samples," In preparation

W. Harlow, A.C. Lang, M. L. Taheri, "Thickness-Dependent Stabilization of Tetragonal ZrO2 in Oxidized Zirconium," In preparation

W. Harlow, H. Ghassemi, M. L. Taheri, "Determination of the Initial Oxidation Behavior of Zircaloy-4 by In-Situ TEM," Journal of Nuclear Materials (2016) 474 126-133

H. Ghassemi, W. Harlow, O. Mashtalir, M. Beidaghi, M. R. Lukatskaya, Y. Gogotsi, and M. L. Taheri, "In situ environmental transmission electron microscopy study of oxidation of two-dimensional Ti3C2 and formation of carbon-supported TiO2," J. Mater. Chem. A, vol. 2, no. 35, p. 14339, Jul. 2014

2 Development and testing of a controlled-environment TEM holder

As the first part of my project, I worked with Protochips Inc. to assist in development of a controlled-environment holder for use with the JOEL 2100 TEM at Drexel University. This system will be based on the existing Protochips Aduro and Poseidon TEM holders, and will follow the environmental cell design mentioned earlier. The custom designed holder used in this work was part of the foundation for the introduction of the Protochips commercial design introduced in recent years.

One of the first challenges for the design of this TEM holder is the selection of materials such it can survive and not be damaged over a large range of environments. This is because this holder is being designed for use running corrosion experiments, and with this comes the obvious environmental hazards to the holder itself. These environments will include various gases, high humidity/ water-vapor environments, and

possibly some liquids. Specific concerns in this area are stress-corrosion cracking in chloride environments, and material degradation under high oxygen environments.

Sample preparation for use with this holder is different than standard TEM sample prep to some extent. Samples had to be made using focused ion beam (FIB), as the E-chip design limits sample size, and the area over which the sample can be viewed. In addition, FIB preparation was non-standard as well, as samples will need to be thinned prior to being placed onto the E-chip, as once on the chip samples cannot be thinned further, as is the case with samples on normal omniprobe grids. Achieving samples thin enough for use via FIB may also prove to be challenging, as the windows on the gas cell will add significant thickness that the electron beam must pass through. Finally, placing samples on a ~50 nanometer thick window will be challenging. E-chip type heaters are not particularly uncommon, however their use outside of nanoparticles and directly deposited thin films has been limited.

Following the delivery of the holder, various experiments were performed, and recommended design changes were accumulated, along with system limitations, which were then passed along to Protochips so that the holder design can be improved before this holder became a commercial product. Experiments included experiments under vacuum, various gas pressures and mixtures, preliminary vapor experiments, and some attempted liquid experiments. In addition to heating experiments, E-chips suitable for biasing were designed and tested as well, as this provides additional flexibility to the environmental holder, making is possible to study device behavior under realistic atmospheric conditions at the nanoscale.

2.1 Delivery and Improvement of a TEM Environmental Cell

The environmental cell developed in collaboration with Protochips Inc. was delivered in January of 2013. The entire system is constructed out of 316L stainless steel with a short run of PEEK tubing so as to be resistant to all environments of interest, including environments containing chlorine. Multiple other materials were considered, including Alloy 600 and C-276 for better resistance to more environments, however due to time and cost constraints, the decision was reached to use easily available and cheaper 316L.

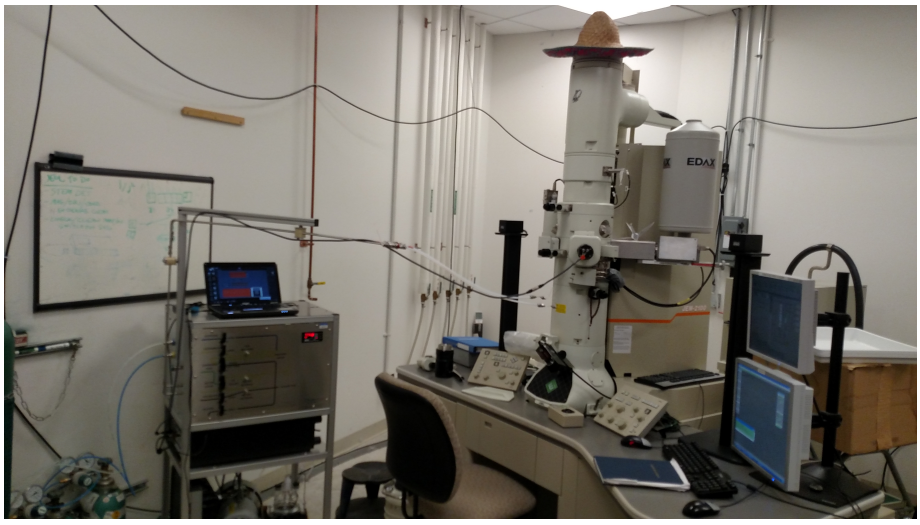

Figure 11: Environmental cell holder as installed at Drexel for use with the JEOL 2100 TEM

The PEEK tubing provides a flexible connection between the TEM holder and the gas manifold, helping to limit vibrations transmitted to the TEM as well as providing and break in the electrical path between the holder and the TEM; both of these help to improve the stability of the TEM holder in the microscope. Within the gas manifold there is a tank system, so gases can be mixed to the desired levels for an experiment. A

system to generate water vapor is available, so that high humidity environments can be simulated as well as gas environments. Figure 11 shows the environmental holder in its current iteration at Drexel.

Quick connects were added between the holder and the gas manifold allow for disconnection of the holder for loading and storage after a few months of use. After approximately a year, gas plugs were acquired that replace the gas lines leading into the holder, which allows for the holder to be used for rapid heating in the TEM column high vacuum and for biasing experiments to be conducted without a second window to seal the cell. In addition, the use of gas plugs allows for precession diffraction to be used for characterization of in-situ samples, as the additional thickness of two windows significantly limited the information that could be acquired. The final version of the environmental cell holder for Drexel was delivered in the summer of 2016. This version included all the improvements from Drexel's suggestions, improved temperature control through a new software program using a feedback loop that references against the calibration file, and a new design of the holder tip ("butterfly") which allows for EDS compatibility. In addition, the existing manifold system was wrapped with heat tape to allow for baking of the manifold system to drive off contaminates in the manifold. In the end, the Drexel system is identical to the now commercially available Atmosphere system, except for the manifold system that is entirely manual controlled instead of software controlled. This allows for greater flexibility in developing new environments, such as highly humid environments, but this does bring significant risks as this also eliminates new safety interlocks the control software provides.

2.2 Initial Testing- MXene

After delivery of the environmental holder, a material system was needed that allowed for simple sample preparation and relatively easy experiments so that a procedure for the use of this TEM holder could be developed, and the users could become comfortable with the holder as well. As such, Yury Gogotsi's research group was conducting bulk oxidation experiments with Ti_3C_2 MXene. This material was an ideal candidate for initial experiments because there was bulk data to which in-situ results could be compared, the material is dispersed in water which allows for very easy sample preparation, and the oxidizing environment was simple; room atmosphere. The objective of these experiments was to replicate the oxidation behavior that was observed in bulk in this material and hopefully identify how and why different morphologies of TiC formed as a result different heating rates.

MXene materials are a new class of 2D material that holds great promise for use in advanced battery systems[92–94]. In the past, much work has been devoted to studying TiO_2 as a possible material for photocatalysis[95–97] and energy storage applications[98–100]. This is the result of the very desirable 3.2 eV band gap of TiO_2 and its good thermal and chemical stability as well as being non-toxic. However, these applications are limited in pure TiO_2 as a result of a wide band gap with a narrow wavelength range for response, the problem of fast recombination of electron-hole pairs, and moderate storage capacity combined with low conductivity. To address some of these problems, much work has been done to combine TiO_2 with carbon, usually through sol-gel or chemical vapor deposition techniques[101,102]. More recently, flash oxidation of MXene materials was proposed as a different single step synthesis method that allows for formation on TiO_2 on carbon in a well-controlled manner[103]. In bulk studies of TiC in a variety of oxygen

pressures and temperatures, it has been shown that the morphology of the TiO_2 produced can be significantly altered by proper control of the oxidizing conditions[104,105]. For MXene type materials, it was shown that anatase TiO_2 particles could be grown embedded in amorphous carbon sheets, but the mechanism by which this occurred and whether or not there were intermediate phases was not known[103]. Through in-situ TEM, the exact mechanism by which this occurs, and whether or not there are intermediate phases could be answered.

In order to study the oxidation behavior of this MXene material in-situ, two heating profiles were used, based on the heating profiles used for the bulk experiments[103]. The first profile was a rapid heat to 950°C followed by 1 minute at temperature, then cooling as fast as possible. The second profile was a slow heating to approximately 450°C at a rate of 0.1°C/second followed by 2 hours at temperature. All experiments were conducted using conventional TEM in conjunction with diffraction. In addition, Raman spectroscopy was used to confirm the information collected following the in-situ experiments. Samples were prepared on E-chips by simply depositing a drop of aqueous solution containing Ti_3C_2 MXene flakes directly onto the heating membrane, and allowing the solution to dry completely. Following this, the environmental cell was sealed, and a static environment of room atmosphere was used as the oxidizing environment.

For the flash oxidation case, the sample was heated stepwise in 300°C increments, with pauses at each step so that focus could be adjusted to account for bowing of the

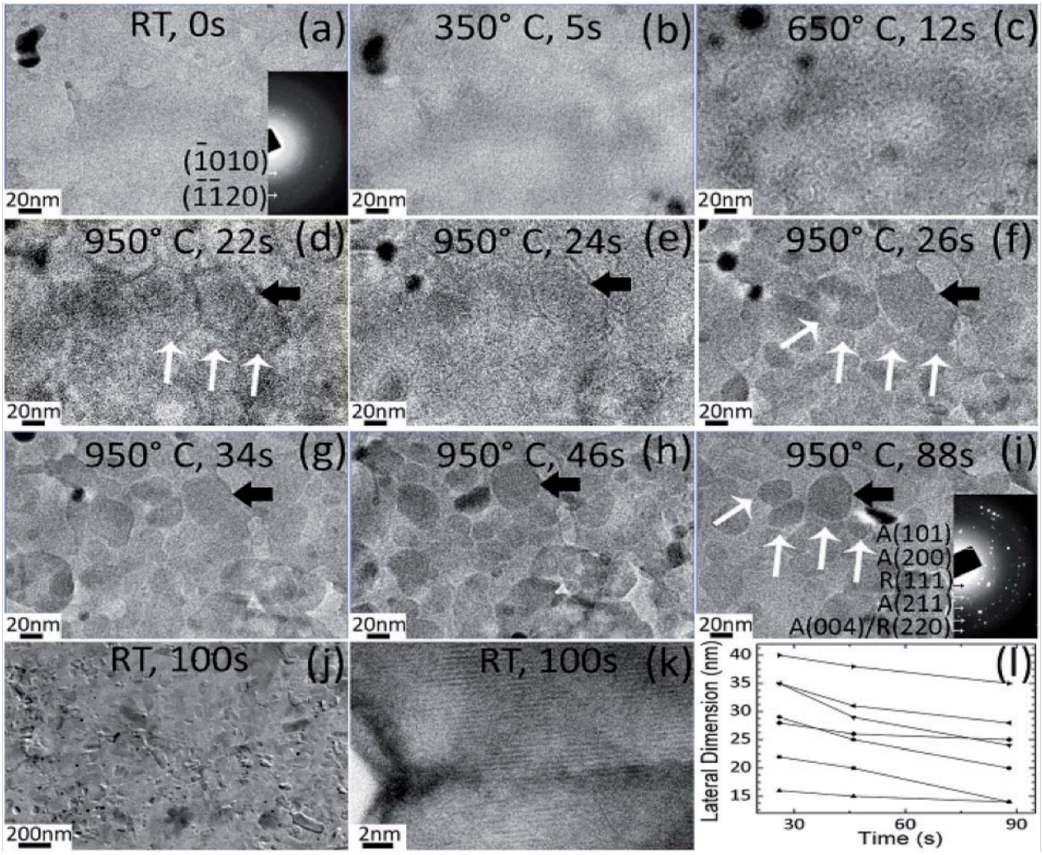

Figure 12: Images showing rapid oxidation of Ti_3C_2 MXene in-situ, adapted from Ghassemi et. al, showing the formation and evolution of the anatase particles (white arrows). Black arrows indicate a specific particle for reference for drift during the experiment.

E-chip membrane. The time for focus adjustment was very minimal so as to limit changes within the sample. When using this rapid heating profile, it was shown that anatase nanoparticles supported by carbon were formed by Ti layers breaking down into large particles, which then further collapse into smaller particles as seen in figure 12. In particular, as can be seen in the progressive images in figure 12, once the particles have formed, as these particles become smaller, the contrast from the particles becomes more defined. This is indicative of the particles shrinking in the planar (x and y) direction, but becoming thicker in the z (beam) direction, thus becoming a 3D type particle instead of

planar sheets. The phase of TiO_2 being anatase was confirmed by both measuring of lattice spacing using high resolution TEM, showing a lattice spacing of 3.8-3.9Å, and through selected area diffraction. In addition, Raman was used for confirmation of transformation to anatase throughout the bulk of the sample.

When the sample was heated slowly to 450°C and held for 2 hours, it was observed that sheets of carbon-supported rutile TiO_2 were formed instead of more discreet nanoparticles. Figure 13 shows an in-situ slow heating experiment, starting with a pristine MXene flake in a, and then showing the progressive changes in the sample during the experiment in b through e.

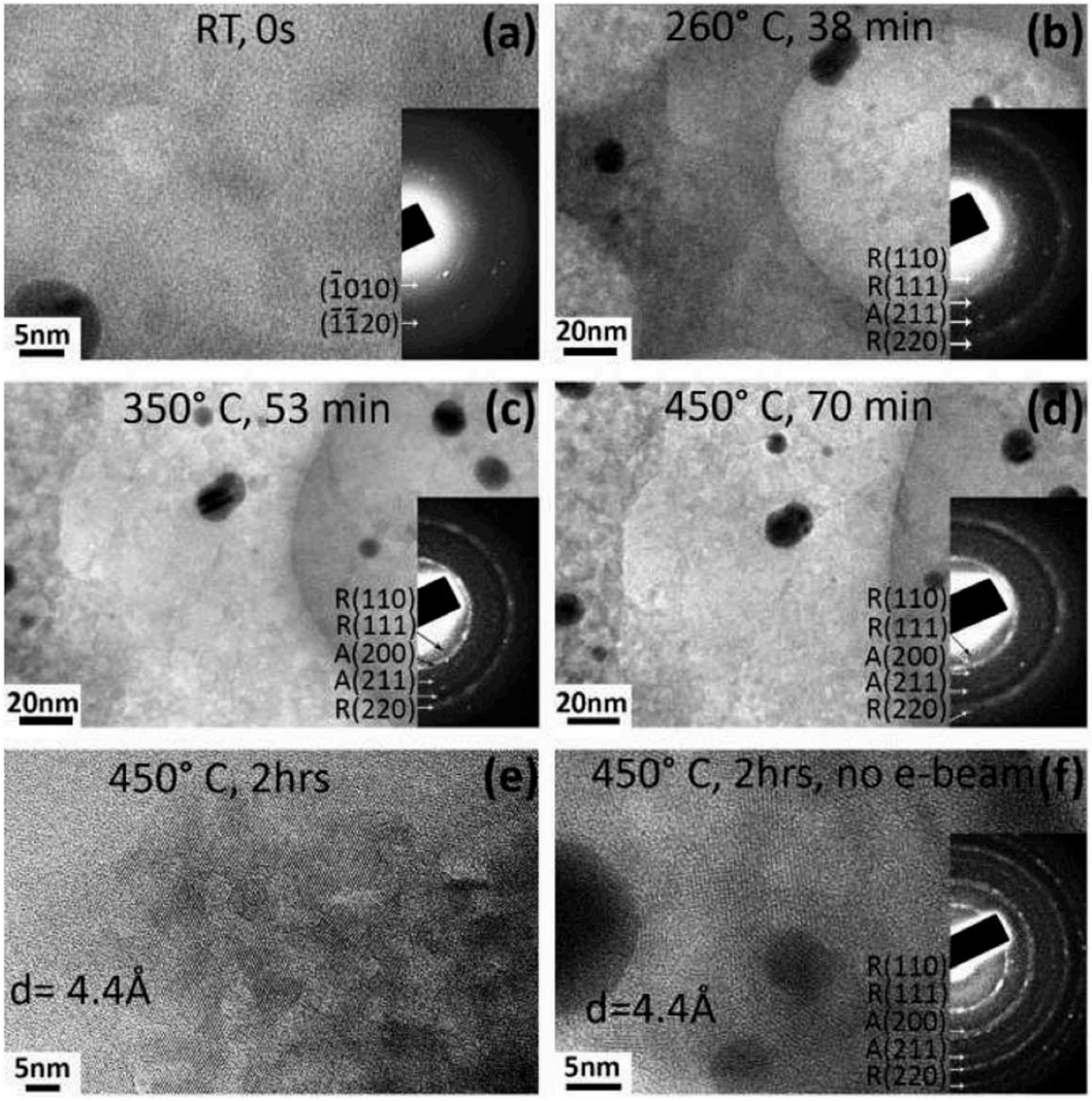

Figure 13: Slow in-situ oxidation experiment on MXene showing the formation of rutile TiO_2, with a)showing pristine sample, b-e) representing the sample during heating, and f) showing little effect of electron beam irradiation to the sample over time as compared to image e). Figure reproduced from Ghassemi et. al

During the course of the slow heating, we see the formation of a granular like structure, but not discreet particles, as is the case for rapid heating. Instead, the sample becomes appears more sheet like in morphology, with a grain like structure. The presence of rutile TiO_2 was confirmed with both selected area diffraction and high resolution TEM, which

yielded a lattice spacing of 4.4Å. Once again, Raman was used to confirm the presence of rutile phase throughout the sample, and that this was not just a local effect observed in the TEM. Due to the long time for this experiment, there were concerns regarding possible electron beam damage to the sample, and whether the energy from the electron beam was affecting the oxidation process by introducing additional heat into the sample. As can be seen in e and f above, there was no observable difference between the area in which all imaging was done during the experiment (e), and an area that was not exposed to electron beam irradiation (f). Further characterization was done using Raman to examine how the different oxidizing paths affected the carbon component of the MXene, and it was found that there were different morphologies of carbon present depending on the path. It was seen that there was less intensity in the D and G bands for carbon in the rapid oxidation case, and these bands were stronger in the slow oxidation case. This shows that as expected, in the rapid heating case, there was insufficient time at temperature for the carbon to reorganize, whereas in the slow heating case; the carbon could reorganize during the experiment, thus resulting in the increased strength of these bands.

Through these experiments, it was possible to propose a path by which oxidation of this MXene occurs during different heating paths. In figure 14 below, a schematic shows the formation path for TiO_2 in each case. For fast or flash oxidation, the Ti layer breaks into small discreet particles (b), which then proceed to shrink in diameter, but grow in the z direction, assisted by the diffusion of the remaining Ti within the sample diffusing to the already formed particles, forming discreet carbon supported 3D anatase particles (c). In the slow heating case, the Ti oxidizes as a sheet, directly forming relatively large particles, with a distinct grain like structure to each sheet (d).

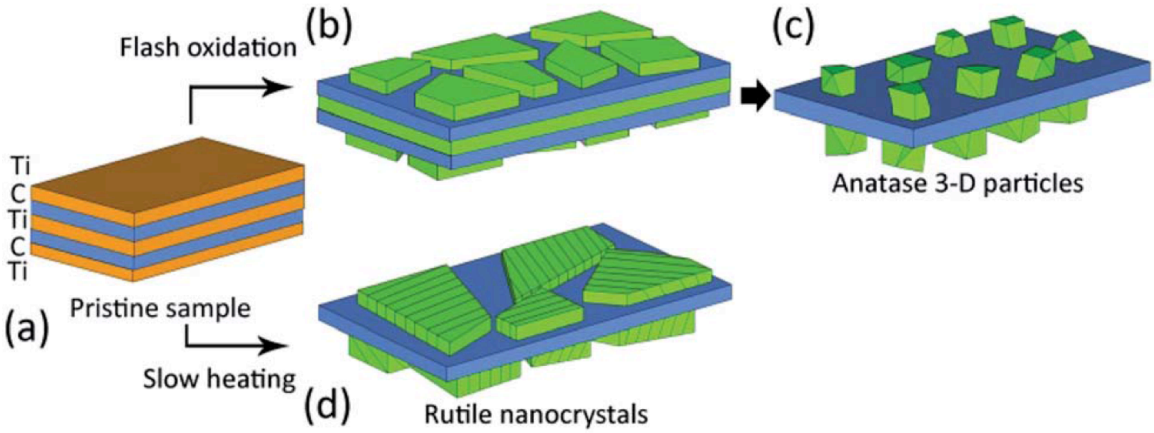

Figure 14: Schematic showing the two different oxidation results possible depending on the applied path. Figure reproduced from Ghassemi et. al

Overall, these experiments allowed us to demonstrate that depending on oxidation path, one can control the crystal structure, the morphology, and particle sizes produced from Ti_3C_2 MXene flakes. In addition, this provides a easy, direct processing route for producing carbon supported TiO_2. This work can be further applied to a wide variety of MXene materials, to change both the produced metal oxide, and the carbon content within the oxidized sample. As a side benefit to producing these insightful results, these experiments provided a good opportunity to become comfortable with the operation of the environmental cell holder without extensive sample preparation, and to learn some of the restrictions of the system. This work was published in June of 2014 in the Journal of Materials Chemistry A[106].

2.3 Holder Qualification for High Humidity Environments

Oxidation experiments in a high humidity environment are of interest due to these providing a closer environment to reality, that is to say the majority of corrosion concerns occur in liquid water, steam, and other high water concentration mediums. However, no TEM holder currently has high humidity capabilities combined with

heating capabilities. Limited studies have been done with dedicated ETEMs, however these experiments come with all the limitations associated with ETEM, especially the limited pressures of <4 millitorr, which is a very low pressure that can significantly affect diffusion-controlled processes such as oxidation. Humidity levels were tested using humidity sensitive salt samples, including sodium chloride, potassium chloride, and potassium sulfate. Other samples, such as soot particle clusters, that are known to collapse and densify in high humidity environments and metal samples were to be used for initial experiments. In addition, the use of liquid inside the environmental cell was explored to see if liquid could be successfully used in the system in conjunction with heat. This would open the door to a large number of experiments in various fields, and in this case we were investigating the possibility of observing the formation of precipitates from a solution under heat.

Interest in conducting high humidity experiments in the TEM has been a long running goal, and currently due to interest in how soot particles deform under varying humidity levels, there is again a push to create a controlled-level humidity system for in-situ TEM examinations of water vapor-particle interactions. Soot particles are thought to play a significant role in global climate, but the exact role these particles play is unknown, especially with respect to how soot particles interact with water vapor[107–110]. It is thought that soot will act as a cloud condensation nuclei or ice nuclei, but how the soot particles interact with water molecules is not well understood. In particular, soot can come from a variety of sources, including internal combustion engines, burning of fossil fuels, and biomass fueled fires, and how each of these sources reacts differently with water molecules needs to be understood. As such, it is necessary to characterize each type of soot for structure, chemical composition, and humidity response. This has been done using

several techniques, such as tandem differential mobility[107,111] and aerosol particle mass analyzers[111], with TEM being used to characterize both particle morphology and provide elemental analysis on the composition of the soot particles produced from various sources[107,109,111–113]. Recently, there have been some efforts to use environmental TEM to study the interactions of soot particles produced via biomass burning with water vapor[112,113]. These studies have shown that soot particles have significantly varying compositions, and that these compositions affect particle behavior with regards to collapse and densification. An outstanding question remains as to the mechanism for particle collapse, and whether the low pressures present in a dedicated ETEM affect the particle collapse behavior.

In order to study soot particle behavior, the first step needed was the qualification of the gas cell type holder for high humidity environments. Qualification was to be achieved using salt particles with well-known efflorescence and deliquescence points, particularly sodium chloride and potassium chloride. The overall goals were to first prove that the gas cell system could be used for high humidity environments, second show that control could be had over the humidity levels, and third that corrosion processes could be conducted under the high humidity type environment. For the first objective, the idea was to simply reach the deliquescence point of the sample and correlate the external humidity level readings to the changes observed in the TEM so any offset could be identified, and do so with multiple sample types for confirmation. The control over the humidity level would be demonstrated two ways, first by reaching deliquescence of the sample and then reducing humidity levels to cause efflorescence, and second by reaching a point slightly below the deliquescence point and holding the sample at that level until dissolving the particle is desired. The final objective of showing the relevance

of high humidity environments for oxidation experiments would be conducted using pure zirconium and comparing oxidation results to those achieved using a controlled gas environment.

In pursuit of the first objective, samples were prepared from sodium chloride, potassium chloride, and potassium sulfate which have well known deliquescence points of 75.2%[114,115] ,84%[114,115], and in excess of 90%[114,116] respectively. These samples were prepared either by grinding the particles to produce small particle diameters, or dissolving the particles in deionized water to form a low concentration, which was then dried onto the E-chips. As will be discussed further during the adventures in liquid TEM, the preferred preparation method was grinding following by aerosolizing the powder and allowing to settle on the E-chip as opposed to the dissolution method. Next, the method of delivery of humidity-controlled air into the environmental cell was developed. A small commercial fog generator was used to create a highly humid atmosphere in a glass vessel, which was then connected via a tee-joint to an air dryer with valves leading to each source of air. This allowed for mixing of the two airstreams to provide the desired humidity level, which was monitored further upstream using a Vaisala HMP-60 temperature and humidity probe run using PuTTY to provide real time humidity level read outs. Air was pulled through the system using the vacuum pump intended for pulling the system down to a low vacuum (~5-10 torr) prior to mixing of the experiment gases. Initially, the humidity system was fed into the gas cell manifold, using the quick connect system similar to the use of dry gases. However, it was found that the additional line length provided by the internal components of the manifold created an extremely long lag time (in excess of 10 minutes) prior to seeing a humidity level change just prior to the TEM holder inlet. Thus, instead of using the quick connect socket to attach the

humid air source and pulling the humid air through the manifold, the connection to the holder at the manifold was disconnected and directly connected to the humid air source. This improved the response time greatly, to within a minute to two minutes to start seeing a change in the inlet air humidity level. Now that the humidity level was found to be changing on the inlet side of the TEM holder, samples were prepared to monitor in-situ while the humid air stream was pulled through.

Initial testing was done first with salt particles, and then a corrosion experiment was conducted to determine the feasibility of using a humid air stream for oxidation experiments. The oxidation experiment will be discussed later in the section oxidation behavior in pure zirconium. Multiple salts were used in order to try and determine the accuracy and response times of the interior of the cell as compared to the external humidity sensor. A significant problem was encountered that many of the salt particles used are beam sensitive, especially to a 200 kV electron beam, so care had to be taken to limit damage to the samples. Thus, snapshots were taken based on the external humidity readings, then the beam was blanked to help limit damage to the samples and ensure any particle morphology change was the result of humidity effects. Initial experiments conducted using potassium sulfate showed that these samples were too beam sensitive to be used during the initial characterization steps, so work focused on potassium chloride and sodium chloride. For potassium chloride, the samples were observed using conventional bright field TEM, and it was seen that the samples did indeed react as expected, starting to dissolve at around 66% relative humidity, and dissolution rapidly accelerating once the deliquescence point of 84% was reached. By 90% relative humidity, the salt particle being observed had completely dissolved, with only an outline of the particle remaining. The series of images taken leading up to the dissolution of the

particle are shown in the figure 13 below. Experiments were also carried out using sodium chloride in diffraction mode so as to identify for certain that the crystalline structure of the salts was changing,

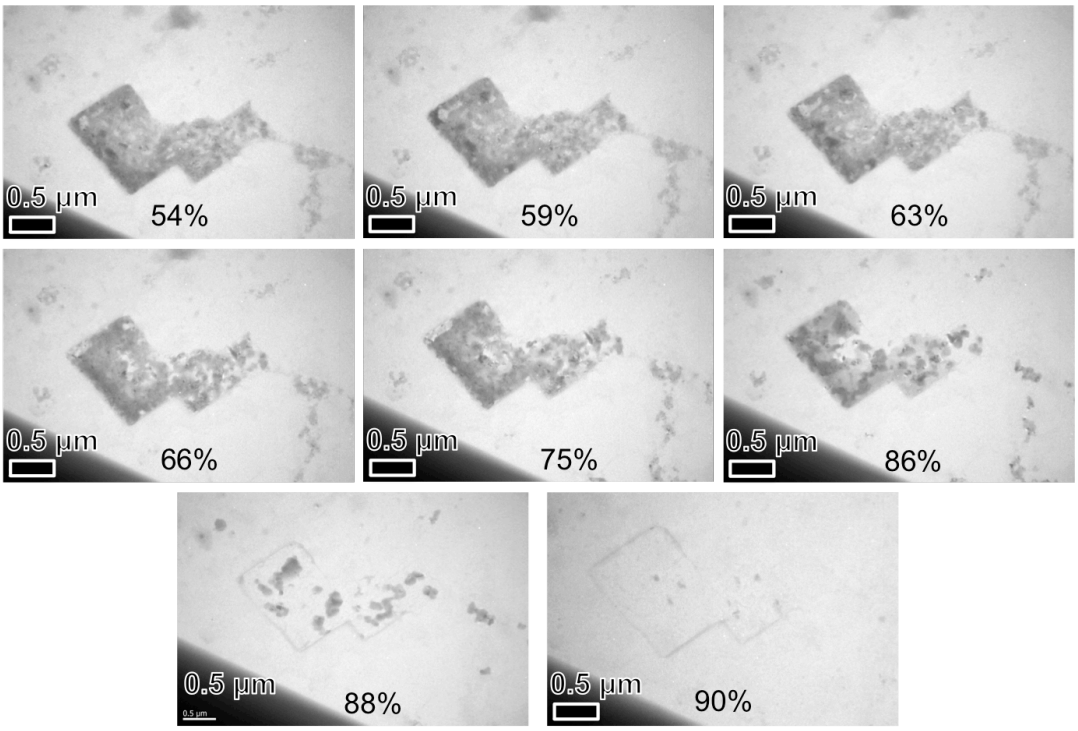

Figure 15: Series of bright field TEM images showing the dissolution of a KCl particle with increasing humidity level. The exact humidity level for each image is stamped on each image.

and the changes observed in potassium chloride were not just the result of beam damage to the samples. The objective of using an additional salt was to reaffirm that these results were reliable using multiple systems. Initially the plan was to conduct both bright field and diffraction experiments on both systems, but due to time limitations this never came to fruition. Diffraction is limited in this TEM holder because of the single axis of tilt, and the limited number of degrees of tilt that can be achieved using the high-resolution pole piece in the microscopes at Drexel. For this experiment, since no heating was conducted

on the sample, the specific particle could be selected for observation using a selected area aperture, however unfortunately, in this case the number of diffraction spots that could be observed in a particular orientation of the crystal in the field of view meant there were insufficient spots to effectively match the diffraction pattern. That said, as shown in the figure above, the objective of the experiment could still be met, as few number of spots

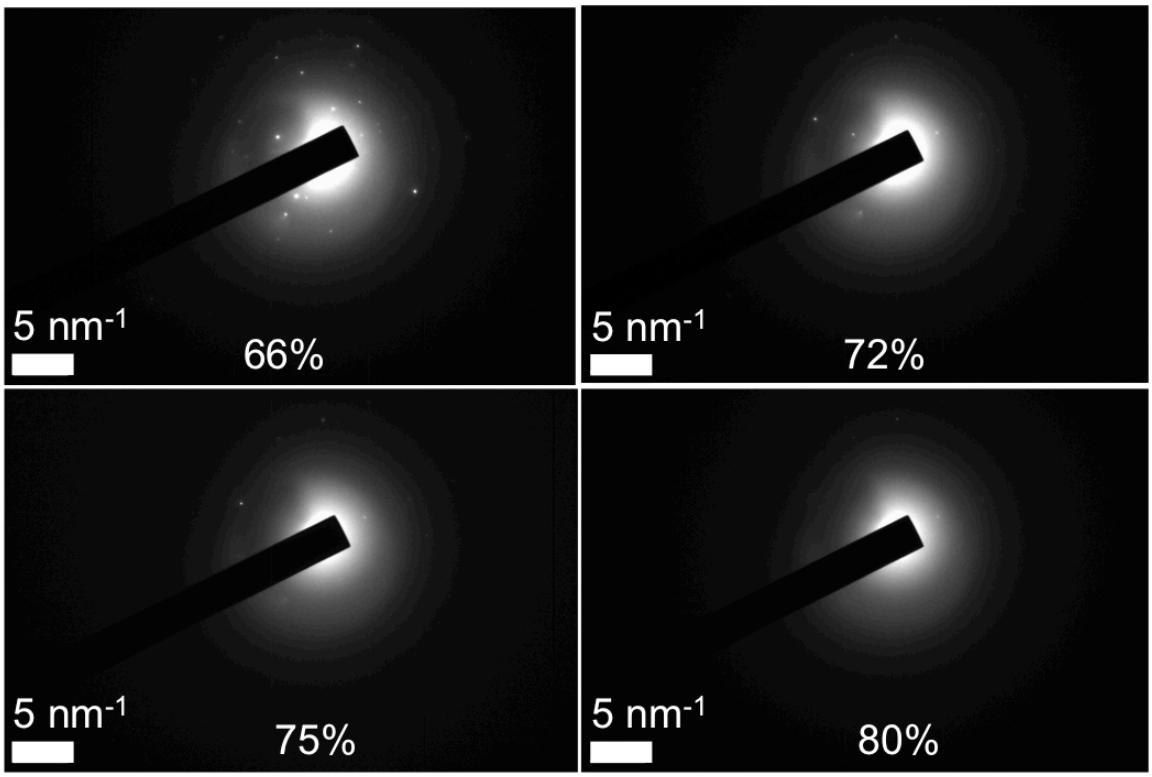

Figure 16: Diffraction patterns taken during an high humidity experiment on NaCl showing the dissolution of the particle as shown by the disappearance of diffraction spots at progressively higher relative humidity levels.

made it easy to determine that the particle was dissolving at each humidity level by spots disappearing during the experiment. As can be easily seen, the expected deliquescence point for sodium chloride was 75.2%, and during our experiment only a couple diffraction spots remain when the pattern was taken right at the time the inlet humidity

level was reading 75%. By the next step of 80% relative humidity, the particle was completely dissolved, with no diffraction spots remaining. These initial results showing the effect of humidity on the salt particles is encouraging for further development of the controlled-humidity system. When compared with previous work done by Wise et al. using an ETEM[115,116], we see that in our system there are some significant differences that need to be further investigated. In particular, once a particle has hit the deliquescence point, we would expect our samples to form droplets, such as those shown by Wise et. al[115], however instead we see just an outline of the particle remaining. In diffraction, we see what appears to be the slow dissolution of the NaCl particle to droplet, but after the experiment we see results similar to KCl, with only an outline of the particle remaining. Currently, the explanation that seems most plausible is that the flow rate over the sample is sufficiently high, and because deionized water is being used, that the ions in the salt particle are being picked up in the humid air stream and being removed from the windowed section of the E-chip.

These experiments have provided a proof of concept for operating this system in elevated humidity environments is both feasible, and has great potential for allowing studies of humidity effects at atmospheric pressures, thereby eliminating one of the major flaws currently present in other studies. However, that said, substantial work remains to be done to make this a routine experiment. The proof of concept shown here was all done prior to the upgrade of the environmental cell system to the butterfly style, and the flow rates with the new system will need to be confirmed and repeatable as some internal changes clearly occurred during the update process. Following this, the system will need to be modified and a large number of experiments conducted in a repeatable system to calibrate valve settings to specific levels of humidity. For the proof of concept presented

here, the humidity level was not well controlled to the level at which specific targeted humidity levels could be attained. Instead, the humidity levels would be controlled to rise slowly allowing for images at each humidity level to be taken, however the response time to lower the humidity level meant that the humidity level would continue rising for up to 15-20% over the desired level before reversal occurred. Once reversal occurred, the humidity level would drop very rapidly, usually bottoming out near ambient conditions. This lack of control meant that reaching a specific humidity level and holding constant was not achieved during these initial experiments. Furthermore, prior to publication, a method needs to be established to humidity level on the outlet side of the TEM holder. Currently, if an identical sensor to the inlet side is installed on the outlet side the humidity level immediately drops to below ambient levels once the vacuum pump is turned on, most likely because of the low pressure the sensor is trying to read values from. In order to solve this, the pressure on the outlet side needs to rise back to atmospheric pressures via airflow through the small holder tip, which will take a extremely long time, and the humidity level will need to be kept constant on the inlet time for this long period of time. Overall, these efforts have laid the groundwork for very substantial contribution to multiple fields by allowing for the study of materials at high humidity levels under atmospheric pressures inside an electron microscope, but considerable further effort will need to be devoted to finalize the development of this type of experiment.

2.4 Liquid Environments

Prior to starting work in high humidity environments discusseda bout, some limited liquid TEM work was attempted using the gas cell environmental holder. Since the gas cell type design is descendent from the liquid style of environmental holder, using

the same chip sandwich type design, there was not expected to be a problem with sealing the liquid in the system. Instead, the concerns were sample thickness and contamination of the TEM holder and gas tubes leading to the holder tip. The objective of trying this type of work was to show that a gas cell type system could also be utilized for static liquid experiments, as opposed to dynamic environments possible in a dedicated liquid holder, and if possible heat the liquids, as during the period of time this was tried there was no commercial solution for heating liquids in-situ. Attempts were made using a gold nanoparticle solution for resolution tests from TedPella, as well as a solution intended to precipitate cobalt carbides[117]. The problems with conducting liquid experiments in a gas environmental cell holder proved to be many fold, and I will outline these problems so future workers can avoid or mitigate some issues. First, sample preparation for liquid experiments using this system is very difficult. In a dedicated system, nanoinjectors are part of the holder design are used to push the liquid into the cell viewing area. In a gas cell, the liquid must be placed directly onto an E-chip using some manner of micropipette. The liquid volume needs to be very small, about 0.5 μL or less, with our best success occurring at around 0.2 μL. A careful balance between too much liquid and being able to break the surface tension of the droplet from the pipette tip must be achieved and is very difficult. If the droplet is too small, the surface tension will not break and no liquid will be deposited or the liquid will evaporate too quickly to seal into the holder. If the droplet is too large, the holder tip will be flooded with excess liquid that needs removed prior to inserting in the TEM and cleaned from the gas lines. Also, if the liquid is polar, such as water, it can be very difficult to separate the droplet from the pipette tip without it sticking to the SiN membrane. If the droplet is not separated from the tip and the tip lifted, the membrane will be broken. In addition, when the polar

substances dry rapidly because of the small droplet size, during final evaporation the membrane will fail most of the time. To combat these problems with polar substances, the E-chip can be plasma cleaned, as this will make the chip hydrophilic. By making the substrate hydrophilic, the liquid will spread evenly across the chip surface instead of balling on the surface. This is also beneficial for closing the holder lid, as otherwise stress is placed on the E-chip membranes when the liquid droplet is taller than the chip spacer. However, this flow of the liquid almost always results in excess liquid in the holder pocket that needs removed prior to insertion in the TEM. Finally, heating is not possible without specially designed chips, as the liquid provides a conductive path, shorting the two electrodes and preventing the resistive heater from heating. Instead, all heating is Joule heating of the sample liquid, and is completely uncalibrated. All problems aside, once these challenges are successfully surmounted, it is possible to use liquids in the gas cell holder, as is illustrated in the image below showing gold nanoparticles in water.

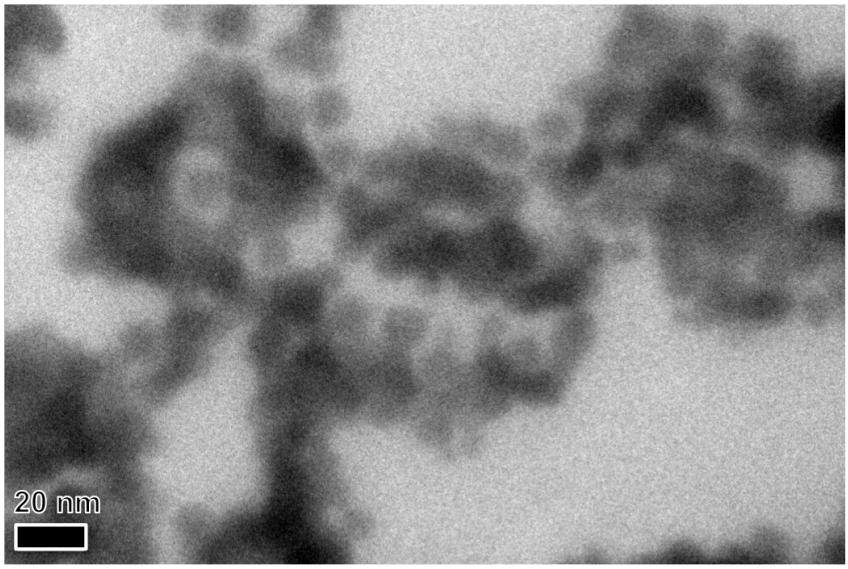

Figure 17: Image of gold nanoparticles in solution using gas environmental cell, illustrating loss of resolution resulting from sample thickness and multiple scattering in liquid.

It should be noted that resolution is greatly degraded as a result of liquid present in the cell. This is where E-chip selection becomes very important, as heating designed chips have 5 μm electrodes/spacers, while liquid designed chips (which also fit the gas holder tip) have a mere 200 nm spacers at each corner, but no heating capability. So in conclusion, while it has been possible to use the gas environmental cell system for liquids, it is highly recommended that if liquid service is required, travel to another institution with a dedicated liquid cell is both more time and cost efficient.

2.5 TEM Sample Preparation

Part of the initial work in this project was focused on utilizing TEM to characterize the as-received Zirconium-based alloys, in both the oxidized and pristine conditions, with the objective of becoming familiar with the microstructural features present in the samples. In the case of the pristine samples, it was recommended that electro polishing be used to prepare the TEM samples, as this should be a simple procedure and provide large regions of electron transparent material. For the alloy in question, Zircaloy-4, many studies have been published using electro polish solutions of 5 percent perchloric acid in methanol, at a temperature of -40° Celsius. It was found that the ideal temperature for the best samples with large thin regions is approximately -38° Celsius, with poor results being achieved if the solution is chilled to -40° Celsius. Liquid nitrogen was used to chill the solution to the desired temperature, and in the case of cooling overshoot; the solution was pumped through the polisher without a sample in place to accelerate the warming of the solution to the desired temperature. Approximately 2 samples could be effectively made prior to the solution warming too much (-36°C) and needing re-chilled for optimal results.

Focused ion beam machining (FIB) is a technique that has been widely adopted in the electron microscopy community for preparing samples for TEM and atom probe tomography, especially site-specific samples targeting features such as grain boundaries. As such, this is a well-developed technique, with samples routinely placed in copper grids, carbon grids, and atom probe supports. Thus, at the start of this work, it was thought that sample preparation via FIB would be easily accomplished. For the initial characterization of the autoclave corroded samples, FIB proved to be an easy and straight forward preparation method once the proper sample geometry was achieved such that the sample had both base metal and oxide present. This was done by mounting a portion of the oxidized sample, cut using a jewelers saw, in epoxy vertically such that the sample could be polished revealing the oxide/metal interface and a TEM sample was made from the interface region.

While FIB proved to be an easy and reliable method for preparing traditional TEM lamella, it quickly became obvious that using this technique was easier said than done when preparing samples for the environmental holder. Other conventional methods of sample preparation for TEM do not lend themselves to this technique, as electropolishing, ion milling, and similar techniques are focused on creating a 3-millimeter diameter sample, with thin regions usually near the center of the sample. The size of the entire heating E-chip the sample is placed on in the environmental holder is approximately 2.5 x 2.5 millimeters, with the region the sample is supposed to be placed on being much smaller. This means that sample preparation via FIB is required for this type of TEM holder.

In-situ manipulation of the samples in the FIB is done using an Omniprobe micromanipulator, with the manipulator movement being controlled by small electric

motors. This makes the manipulator subject to small amounts of drift, and occasional backlash, which with normal copper grids is easily dealt with. However, in the case of the environmental holder, the electron-transparent membrane onto which the sample must be placed is very fragile and the small amount of drift is sufficient to break the electron transparent membrane along with the ceramic heating membrane, thus destroying the E-chip. The fragility of this membrane also means that even a slight accidental touch can ruin an E-chip, so it is very important that the height of the probe be well know at all times. Usually, a good awareness of tip location is easily achieved by using both the electron beam and the ion beam to give the user an almost 3D sense of probe location. Usually, during the normal FIB lift-out procedure, the thick sample is placed vertically on a grid, and ion beam imaging is not a concern. However, in the case of the environmental cell, the sample must be placed horizontally onto the membrane, and this horizontal geometry means that the sample cannot be further thinned once placed on the membrane. As a result of this requirement that samples be thin prior to placement, using the ion beam for another image angle is eliminated as an option since any imaging of the thinned FIB sample with the ion beam will cause amorphization of the sample. Thus, only a 2D electron beam image is available to try and judge the height of the probe versus the surface one is trying to drive the tip to, which while this can be monitored to some extent by scrolling the focus between the tip and the surface, not impacting the tip on the surface is very difficult, especially with the long depth of focus present in an electron beam image.

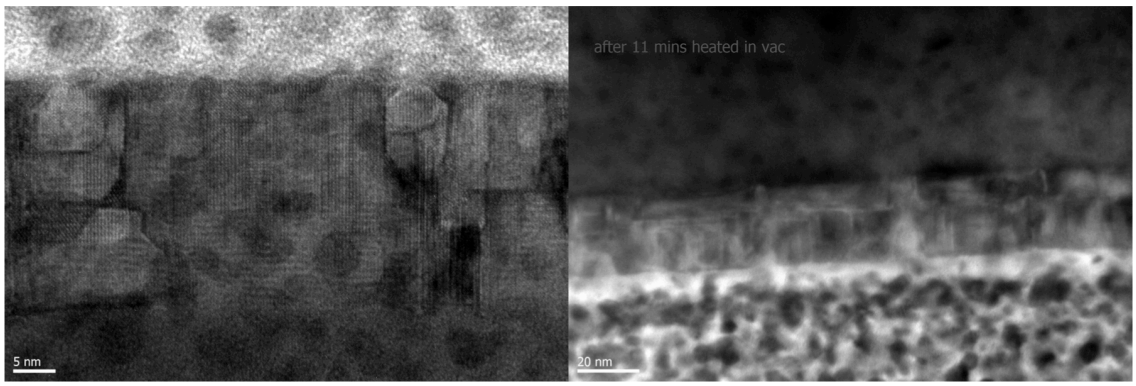

Figure 18: Two images from an LSFO thin film sample showing the effect of window thickness on achievable resolution. Image on left shows the sample with only one window in place with gas plugs, while image on right shows the sample with two windows in place for use with a gas environment.

While discussing the requirement that samples be thin prior to placement, another problem that an experimenter needs to be aware of is the increased thickness provided by the SiN windows means that these samples must be thinner than what would otherwise be an acceptable thickness for TEM. This particular problem is well illustrated in figure 15, which is an $L_{(2/3)}S_{(1/3)}FeO_3$ thin film sample prepared for an experiment using FIB. When the sample is loaded into the holder for the initial heating run in vacuum, only one window is used, and high-resolution microscopy can be done on the sample. However, when the second window is added heat the sample in oxygen, high resolution can no longer be achieved due to the additional thickness of the window.

Moving back to sample manipulation, approximately 8 months of time was spent trying to prepare samples onto E-chips using the Omniprobe micromanipulator in the FIB and overcoming the challenges discussed above. It was found that in-situ manipulation in the FIB using the Omniprobe was not capable of placing these samples, as invariably the chip was broken. This conclusion was the result of trying many different geometries to avoid breaking the chip, including standard lift-out techniques at 0° stage

tilt, attempts at 52° stage tilt, and using an inclined sample stub to make the sample as parallel as possible to the chip. Each geometry was tried multiple times to help eliminate the possibility of operator error being the cause of failure.

For the standard lift-out attempt at 0° stage tilt, illustrated in figure 16 A below, it was found that the sample always impacted the E-chip surface with the bottom surface of the sample, and then trying to get the sample to lay down horizontally from its' vertical orientation resulted in breaking the E-chip. Even if the sample was intentionally cut loose in the preparation trench such that the sample was no longer perfectly vertical, the sample would still impinge on the surface first, and when pushing the sample flat was attempted, the membrane on the E-chip would fail first. This approach had the additional problem that when the sample is cut loose in the trench and allowed to fall, there is no control over how the sample falls. The sample can fall sideways, backward, forward, or tilt up at an angle in the trench. If an attempted is made to control the direction of fall using the Omniprobe to try and influence the direction, there are two typical outcomes. The first outcome is the sample statically adheres to the Omniprobe, and does not fall, which defeats the purpose of trying to cut the sample loose. This does however offer the opportunity to try and move the sample without the sample being welded to the probe, which in theory should make placement easier. However, without a weld to the probe, when the probe is retracted from the camber to move to the E-chip, the sample is almost always lost. The second possible outcome is using the Omniprobe to exert pressure on the sample while cutting to try and cause the sample to fall in the desired manner. Instead, this tends to result in the sample breaking loose and being punted into the vacuum of the chamber when it is almost cut free, and a high chance of bending the Omniprobe tip when it jumps suddenly.

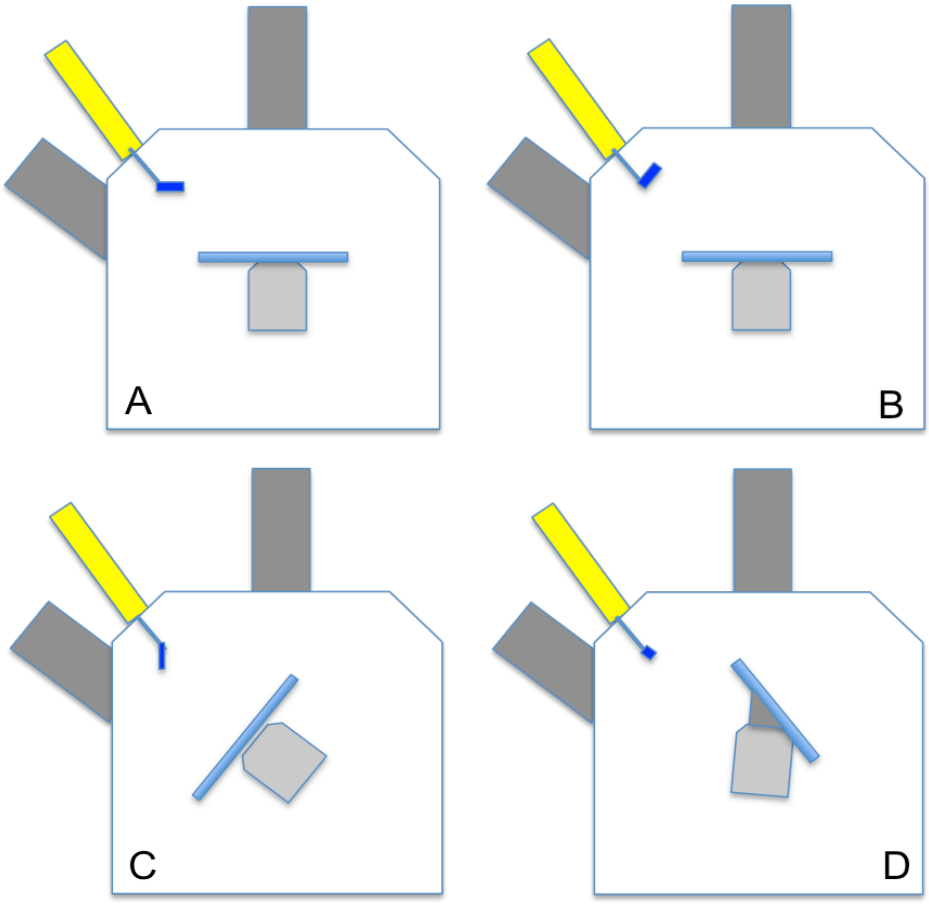

Figure 19: Schematics showing the various geometries tried to achieve success using in-situ liftout to prepare samples on E-chips. A) Shows standard lift-out configuration B) Lift-out at 52° with E-chip at 0° C) Sample at 0°, E-chip at 52°, and D) Sample at 52°, E-chip at -52°

Following the attempts using the standard FIB geometry, tilting the stage in the FIB to 52° such that the E-chip was closer to parallel with the sample was tried as is shown in figure 19B and 19C. This was considered slightly dangerous, as the tilt meant one had to be very sure the probe was well away from the stage when inserted, for fear of insertion causing the tip to crash into the stage. The initial attempt at trying this geometry showed that further thought about sample orientation needed to occur, as all tilting the stage did was allow for the sample to impact the E-chip with the corner of the sample instead of the entire base. To solve this, it was necessary to change the initial

attachment point of the probe 90° to the standard attachment orientation (figure 19C). Now, once again, the entire base of the sample touches the E-chip first, and the sample is initially at a slight angle to the membrane. However, the same problem as encountered before still existed, that when an attempt was made to make the sample flat, the membrane on the E-chip failed before the sample moved flat.

The final geometry to be discussed is the use of a specific stub tilted at 52°. The objective with this approach was to solve the problem of getting the sample parallel to the membrane on the E-chip, since so far this had always been a failure point. As such, it was thought that removing the sample while tilted to 52°, in an orientation rotated 90° from the normal lift-out direction, then placing the sample onto the E-chip which was put on a stub oriented to be -52° would be an optimal solution, as then the sample would start out parallel to the membrane. This arrangement is shown in figure 19D. A special tilted stub was required, as the tilt limits inside the FIB are +60° to -5°, with this requiring a tilt to -52°. This idea showed great potential theory, but in practice, it was found there were some major unanticipated problems. The first was that when the -52° stub is in the FIB chamber, the ion column is shadowed such that it cannot see the area of interest. This means that there is no effective way to cut the sample off the Omniprobe. Second was that the Omniprobe comes in from the same side of the chamber as the ion column, which significantly raises the change of stage collision. This location also means that the E-chip must be placed as close as possible to tip of the stub, because of the limited travel of the Omniprobe. Even so, it was found that the Omniprobe lacked sufficient range of motion to make this a viable approach, with the probe often running out of travel while trying to place the sample.

None of these geometries or combinations of these geometries showed promise, with most attempts resulting in destruction of the chip. These geometry concerns were being addressed prior attempting to solve the problem of removing the sample from the Omniprobe without the use of the ion beam, and the problem of removing the E-chip from any tape used to secure it to a tilted stub. After this length of time and the amount of effort spent, it was time to start looking for an alternative way for moving and placing these samples.

Ex-situ lift-out was a common procedure when focused ion beam microscopes were introduced, especially before the advent of duel-beam FIBs. The technique had been mostly abandoned, as in-situ manipulation is generally considered more reliable, and technology has advanced to make in-situ manipulation easy to integrate into the microscope. However, for the task at hand ex-situ lift-out provides the opportunity for many different geometries not constrained by the FIB chamber, as well as better, more sensitive micromanipulators that are driven by oil instead of motors which helps limit backlash problems. An ex-situ lift-out station usually consists of a micromanipulator coupled to a powerful long working distance microscope situated on an air table for vibration reduction. Samples are moved via a glass rod that is pulled to a sharp tip, using static forces to hold the sample on the rod. Initially, the idea to use an ex-situ system was tested out using a system available at Lehigh University, as the cost of such a system is not insignificant, and given the problems with standard in-situ manipulation a confirmation of success was needed. For ex-situ lift-out samples are prepared completely in the FIB trench, and then cut loose and allowed to fall in the trench. When tested at Lehigh, it was found that this method of manipulation was success, but did have a very low success rate of about 10 percent. This success rate was far superior to the success rate with in-situ

manipulation, and so following this conclusion, the costs of building an ex-situ lift-out system versus purchasing a commercial system were evaluated, and a commercial ex-situ lift-out system was purchased.

While the initial success rate for ex-situ lift-out was very low, it was found over time that there are a few factors that need to be carefully monitored to ensure success. First is the operators skill, as the manipulation skills needed to effectively place samples on the E-chips are very specialized, and the operator needs to have experience working with them to understand the device limitations. Ideally, the operator will first learn to prepare samples and move them to regular TEM grids and standard none-heating SiN or carbon film windows. Second, it is very important to monitor the temperature and humidity level in the area surrounding the ex-situ system, as the effect these factors have on static forces and the resulting success of the system is large. In particular, it is very important

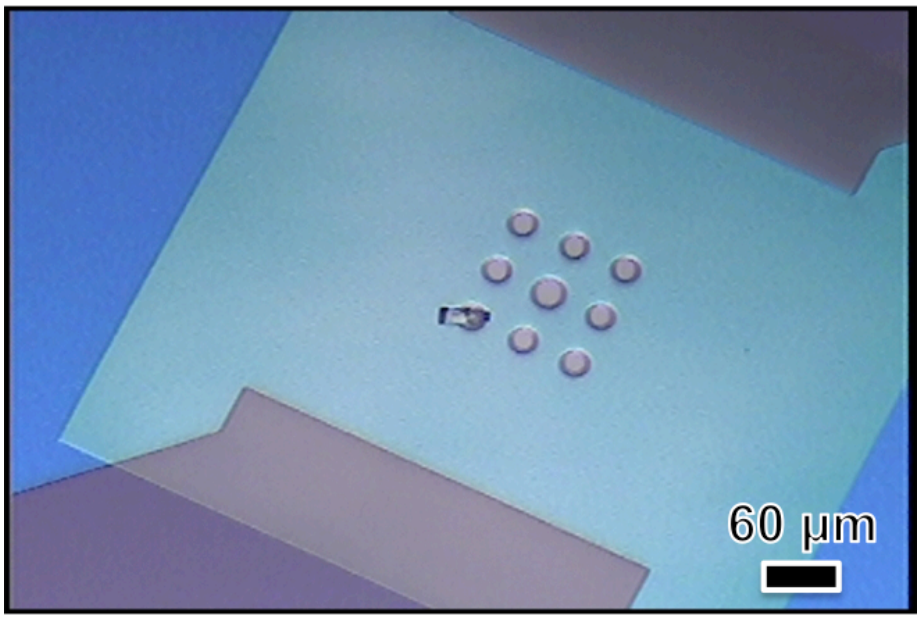

Figure 20: Heating E-chip showing sample placement over SiN windows while bridging SiC heating membrane.

to monitor the humidity levels, as humidity levels below 20% make it very difficult to pick samples up, while humidity levels above ~45% make it difficult to remove samples from the glass rod. While both can be done, entering either of these humidity regimes will significantly reduce the sample placement success rate. The final factor that must be discussed is the E-chips themselves. Each sample needs to be placed over one of the electron transparent windows that are located throughout the heating membrane. The problem with this is care must be taken to not puncture the 50 nm SiN windows, or break the SiC heating membrane. The height difference between the SiN and SiC means that only part of the sample is supported, which reduces the static forces for removing the sample from the glass rod, especially when the humidity level in the atmosphere is too high. Figure 17 above illustrates a heating E-chip, showing the SiN membranes and SiC heating membrane along with a sample placed in the proper location. Another specific problem to these chips is the sample must span across the SiN window, as if the sample does not it is very easy to puncture the SiN window since the SiC heating membrane does not provide additional support for the sample. This must be taken into consideration when making the FIB sample, as a typical 20-μm long sample often has the problem of one side reaching the SiC membrane, but the other corner not quite reaching the SiC on the opposite side. The result of this is the side that is not supported ends up on the SiN membrane, and can puncture the window with the edge or corner of the sample. The particular problem with this is that the puncture is obscured by the sample, and the E-chip will then not seal in the TEM, but instead manifests as a very small leak and is very difficult to diagnose. The final issue that any user needs to be aware of is sample orientation on the glass rod. Because this lift-out technique relies entirely upon static forces, the user has no control over either the orientation of the sample upon picking the

sample up. As such, after the sample has been successfully caught on the glass rod, it is important that the orientation of the sample is determined, and the glass rod rotated such that the sample is parallel to E-chip surface when lowered and the glass rod is above the FIB sample. Failure to do this will either result in the sample being pushed through the E-chip or being flung away when it comes loose from the glass rod. It can sometimes be difficult to determine if the glass rod is above or below the sample by going through focus with the optical microscope. In this case, the best course of action is to try and place the sample down on the surface of the sample it was removed from, assuming the sample is well polished. It will immediately become apparent upon surface contact where the glass rod is in relation to the sample, and there is no risk of breaking an E-chip using this method. It can be a challenged to re-pick up the sample if it becomes flat to the surface however, so this is best done near the FIB trench so that the sample can be pushed back into the trench for easier pick up if necessary. Another problem that can be encountered is the sample flipping up the glass rod, and not being at the tip. This is easily solved by taking the rod to a sharp corner, such as provided by the gold contacts on the E-chip and slowly scraping the rod along the sharp corner which will drag the sample down to the tip of the rod. While this may seem to be many possible problems, in reality once operator skill has improved, success rates of 80 to 85% can be achieved. For the task at hand, this system has allowed for relatively easy placement of samples onto the chips, and is much quicker than similar manipulation inside the FIB.

After samples have been placed on the E-chips, the samples must be attached to the chips to prevent movement during heating, better thermal transfer, and guard against loss of samples during transport between microscopes. The small size of these samples dictates that this occurs in the FIB, as it would be purely a matter of chance to attach the

samples in any other way. As mentioned above, because the samples are already electron transparent when placed, E-beam depositions are required, as I-beam exposure would implant gallium throughout the sample, amorphizing much of it. The parameters used for these depositions have a large impact upon the resulting depositions, as does the gas provided by the GIS. After experimenting with different spot sizes and voltages, the best solution to these depositions seems to be spot size 4 at 5 kV, as this provides a balance between charging problems and deposition quality. Generally, at 10 kV and spot size 3, depositions take much longer, and more drift is experienced, and depositions are lower quality as a result of a less intense electron beam because of the larger electron beam spot size. I have found that when using 5 kV and spot size 4, placing a short 0.5 um x 0.5 um x 0.5 um near but not on the sample prior to starting depositions on the sample helps initial drift problems as well, as long as further depositions are done immediately following this deposition. Waiting for a few minutes prior to starting the next deposition will negate any benefit from the initial small deposition spot. For the depositions following this small initial deposition, the best parameters are ~0.5 um thick and less than 15 minutes in time good attachment to the chip should result. Actual box sizes in x and y dimensions can be changed to achieve the desired deposition time.

When attaching samples to the E-chip, the method of mounting the E-chip for use in the FIB must be addressed. This is a something I did not address in the section of developing a FIB preparation route, as this was never successful enough to warrant investigating this problem. Because of how small and fragile the E-chips are, doubled sided conductive tape normally used to hold samples to SEM stubs is not a good solution, as a 2.5-millimeter x 2.5-millimeter E-chip does not provide much area to grip with tweezers to try and remove from the tape. Slipping with tweezers often results in

brushing the membrane and breaking it, and this is true of both normal and reverse type tweezers. Silver paint cannot be used for attachment, as it leaves residue from the organic carrier, even when dissolved using acetone, which also can contaminate the sample surface and attack the carbon in the platinum depositions resulting in a significant reduction of strength. The concern with residue remaining from the silver paint is that it can prevent the chip from sealing in the TEM holder, while the residue from the acetone can obstruct the SiN windows as well as promote carbon build up in the area exposed to the electron beam in the TEM. The simple solution that I have found to this is to not attaching the chip to the stub, and not tilting the stage, as only the E-beam at 0° stage tilt will be used. However, this is not without drawbacks, as the silicon chip does not have good conductivity to the stub, resulting in charging problems, which are especially prevalent in the large heating E-chips that we were shifting to for EDS compatibility. By polishing a stub down to 1 um diamond solution, then placing the chip and nudging in slightly to seat it on the stub, charging can be minimized to manageable levels, but care needs to be taken to lock the stage tilt in the FIB to prevent accidental activation (F4, lock tilt), and dumping the chip into the FIB turbo pump. Also, one must be sure to lower the sample stage to a working distance of 6 mm prior to inserting the GIS then raising the stage back up to ensure no stage collision since the eucentric point cannot be set without tilting the stage. In theory, a better solution to this problem would be a dedicated stub with an appropriately sized pocket the chip can sit in with a small copper grounding strap that can be rotated onto the gold electrodes to ground the chip, however this would require extensive machine work and would cost an excessive amount of money for custom precision machining to just try and see if this approach worked. This is especially true since the pocket would have to be just deep enough for the E-chip and have a way to

get carbon-tipped tweezers into the pocket for removing the chip as well as having a way to position the grounding strap that is easily moved without slippage and hitting the heating membrane, but stiff enough to provide a good contact.

The final piece of my specialized focused ion beam work was developing a technique for effectively cross sectioning a FIB prepared sample. Currently corrosion is a major threat to infrastructure and has huge costs in terms of both time and money[118]. If initial phases and nucleation sites can be identified to, this better understanding of the effect of microstructure on corrosion behavior will allow for improved modeling and predictions of corrosion performance[25]. In addition, with a better understanding of microstructural effects, improved alloy performance can be achieved through techniques such as grain boundary engineering[7].

In-situ TEM has seen a recent explosion in usage as the introduction of environmental cell and liquid cell holders have opened up opportunities in a large number of fields thanks to the use of MEMS technology, which allowed for miniaturization of the environmental cell, as well as an increase in durability of the cell[73,74]. In particular, the development and commercialization of these holders eliminates the need for a dedicated environmental TEM, dramatically decreasing the entry barrier into environmental TEM work. Recently, there has been an significant increase in work regarding oxidation behavior studied in-situ using environmental TEM[64,106,119–122]. These experiments have been limited to two dimensions effectively; as experiments conducted in-situ cannot be viewed in cross section, which has limited some information regarding phase and oxide thickness. Other in-situ experiments such as nanowire growth and thin film growth may benefit for additional information offered by cross sectioning of in-situ TEM samples. By utilizing focused ion beam machining, which

has long been a common technique for preparing traditional cross-sectional TEM samples from bulk materials[123], it is possible to provide a post mortem cross sectional analysis of in-situ TEM samples.

During in-situ oxidation experiments in zirconium-based alloys, it became clear that developing a technique for effectively cross sectioning a FIB prepared sample was needed. The very important information that was needed was oxide thickness and oxide structure. In the typical TEM situation, neither of these pieces of information are easily obtainable, as the electron beam is passing through the sample creating a two dimensional image. It was important that oxide thickness be known because if the sample reaches through-thickness oxidation conditions, it will allow the relaxation of the oxide, and eliminate any information about the presence or absence of the stress-stabilized tetragonal ZrO_2 phase. The effect of each oxide phase in the oxidation of zirconium and its alloys has been a outstanding question in the field, especially since the tetragonal phase of ZrO_2 only stable under high stress at room temperature[52]. Multiple authors have proposed that an unstable oxide phase may account for the cyclic oxidation behavior seen in long-term oxidation experiments[17]. Other in-situ methods such as x-ray photoelectric spectroscopy (XPS) and synchrotron XRD studies have shown that tetragonal ZrO_2 is the initial oxide layer that forms [37,42] and it has been shown that the tetragonal phase fraction is reduced when relaxation and transformation to monoclinic occurs[124].This relaxation was also seen to allow the formation of cracks in the sample[41,44], which may indicate the formation of cracks in this oxidation system being the result of oxide relaxation. Structure information was important, as the oxides formed in these systems is often characterized by structure, being either equiaxed or columnar[41,43]. So a method to gain

these two pieces of information was critical, and with the proliferation of environmental cell systems, other experiments are sure to benefit from this technique.

Cross sectional samples were prepared from in-situ TEM samples consisting of Zircaloy-4 or ultrafine-grained Titanium. In the case of Zircaloy-4, cross sectioning of these samples provides information regarding oxide thickness and structure. The ultrafine-grained titanium samples provided information regarding microstructural evolution under a simulated induction furnace heat treatment. Zircaloy-4 samples were oxidized in-situ[119] using a Protochips environmental cell, while titanium samples were rapidly heated in-situ using the same system in vacuum, with both sets of samples being placed on the silicon carbide heating membrane of an E-chip. Cross-sections were made using an FEI Strata DB-235 using an Omniprobe Model 100.7 micromanipulator when in-situ lift-out was conducted. Samples moved ex-situ were moved using an EXpressLO lift-out system. Platinum coating was conducted using a Cressington 208HR sputter coater. All TEM imaging was conducted using a JEOL 2100 LaB_2 at 200 kV.

To best compare in-situ samples to ex-situ corroded samples, in-situ FIB samples need to be viewed orthogonal to the TEM beam direction. In order to do this, the sample must be removed from the E-chip on which it is placed for the in-situ experiment, protected from the ion beam, moved and placed on a regular TEM grid, and prepared for TEM. Since the entire sample area is already very small, cross section samples following this method are very difficult to make, and thus when initially preparing samples for these experiments it is recommended to have a minimum of two samples on each E-chip for each experiment in order to increase the chance of success at cross sectioning the samples. To start the cross sectioning process, the E-chip is attached to a

normal SEM stub using double sided conductive tape and loaded in the FIB. After initial alignments, identify the sample locations to be cut loose, and then move to a corner of the heating membrane far from the samples to be cross-sectioned keeping in mind the direction to be moved. Using the 10 pA ion beam aperture, align the ion beam to the electron beam at 52° tilt using the heating membrane corner as a good reference point. Following this, move near to the area of the sample imaging with the ion beam, but do not move over the sample while imaging. When near the sample, take a lower magnification electron beam image to identify where the welds are of the sample to the E-chip (NOTE: it is critical that the magnifications of the ion and electron beams not be linked.) Switching back to the ion beam, very carefully move the stage such that just the edge of the sample and weld are visible in the ion image. Make a small line cut to separate the sample from the welded section, and then repeat this method for each weld on the sample while taking care to not expose any sample to the ion beam. After the samples are cut free from the E-chip, the EXpressLO ex-situ lift out tool should be used to reposition the sample from the fragile SiN/SiC heating membrane area to the solid substrate. In this example, we used the silicon area of an E-chip as a substrate. Samples should be laid flat on the surface in order for the substrate to act as a framework for the sample later.

After movement, the chip should be surface coated using the platinum coater for 60 seconds at 40 mA. For the platinum coat, 60 seconds at 40 mA is sufficient, and no rotation should be enabled for the coat. This coating both minimizes charging of the sample during electron beam deposition and helps to begin attachment of the sample to be cross-sectioned to the substrate. After coating, the SEM stub should be put in the FIB, and an electron beam deposition at 5 kV spot size 4 of depth 0.02 μm, width of 2 μm

should be made over the area to be cross sectioned. The figure 21 below illustrates the cross-sectioning process.

Prior to the electron beam deposition, it is very important to decide the area from which the cross section will be made. On a standard FIB sample of approximately 5 μm height, if great care is taken, two cross section samples can be made, but the samples have to be from the highest and lowest points in the sample so as to successfully lift them out. It is much easier and lower risk to make a single cross section from the center of the sample, but there are a couple trade offs with making a single cross section. By making one sample, you only get to observe one region of the sample, which is about 100 nm in thickness, but it is easier to avoid any damaged regions resulting from cutting the sample loose in the FIB. On the other hand, if two samples are made, you get information from two distinct regions, however the samples are much closer to the damaged regions from cutting the sample loose, and that information may not be very close to region observed in TEM. But, this will result in information from about 200 nm in thickness of the sample in cross section, even though there is a reduction in the length of the area that can be observed because of FIB damage near the sample edges. In some metal samples, having cross sections in two regions may allow for observations of multiple different grain boundaries, whereas a single cross section would limit the number of grain boundaries present.

After making the decision about and placing the corresponding electron beam depositions, ion beam depositions will be used to build up the protection layer to a reasonable thickness. The operator must decide the best of two approaches, either the sample will be laying almost perfectly flat, at which point a 1.5 μm platinum deposition can be made over the entirety of the area of interest and extend over the silicon substrate,

or the sample will not be very flat to the surface at the edges. It is for this case when a small deposition of 1 µm by 1 µm by an appropriate depth should be made so that then when the deposition covering the area of interest over to the silicon substrate is done there is good attachment of the sample to the silicon substrate. After the region or regions of interest have been protected, a normal lift-out procedure is followed, making sure to make the trenches longer than the width of the platinum layer attaching the sample to cross sectioned to the substrate so as to maintain good connection between the substrate and the cross section sample. If two cross section samples are being made, the area between the two samples should be milled to a depth of 6-8 µm depending on the operators judgment using the 3000 pA aperture so as to minimize drift and milling damage to the two samples, then the undercut should be make from the trench side with care to not accidently cut the second sample loose when the first sample is cut free for removal following Omniprobe attachment.

When the sample is moved to the grid using the Omniprobe, the best posts for attachment are those with a V type top, with welds on each side of the silicon substrate to attach the sample.

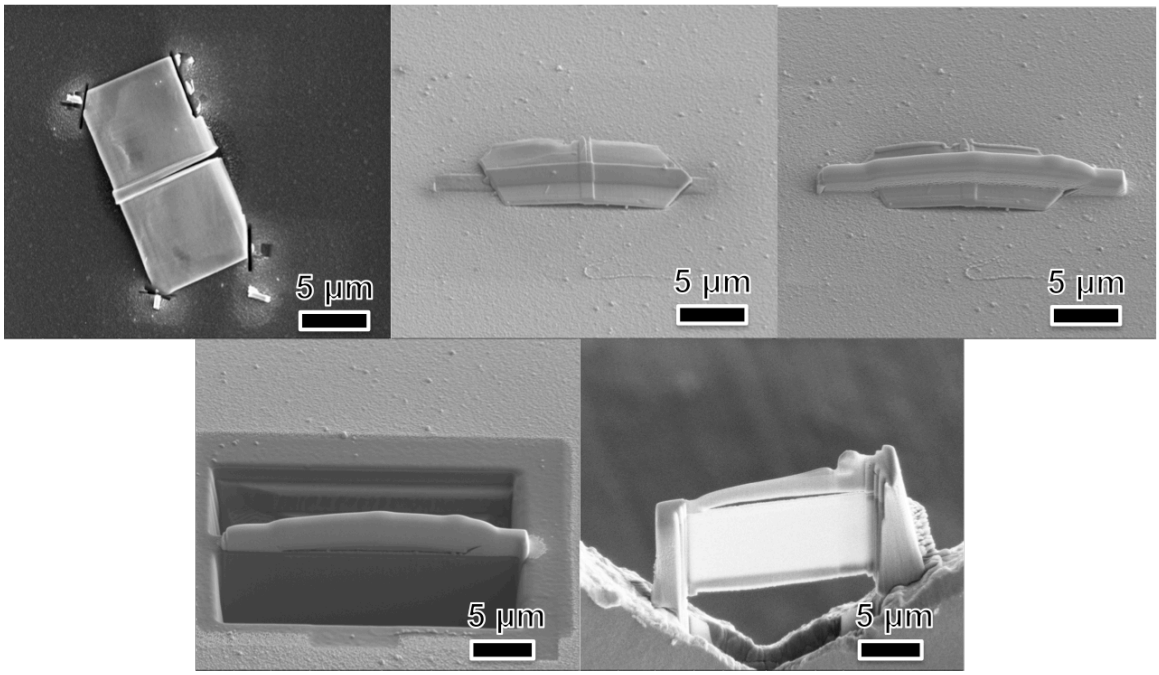

Figure 21: FIB images showing steps to cross-section an in-situ oxidized FIB lamella.

For thinning the sample, minimal depth is needed since only the sample to be cross-sectioned needs to be thinned, and the length to be thinned is slightly shorter than the overall length of the sample so as to avoid damaging the welds to the substrate. Thinning can be done using the 300 pA aperture down to about 500 nm thickness, then further thinning should be conducted using either the 100 or 50 pA aperture. If the substrate below the sample during the thinning process is destroyed, this is not an issue of major concern, since the edges supporting the sample are still well attached and not in the thinning region. After the sample nears final thickness, a low kV clean (5 kV) should be done to reduce damage. The process we used for this is doing 5 degrees tilt each direction from vertical for 2 minutes per side using the selected area box, moving in to 3 degrees from vertical for the same process, and then 30 seconds to 1 minute at vertical, unless the sample appears to need further thinning in which case longer times at the 5

and 3 degree tilts can be used. Through this technique, high resolution TEM information can be acquired from the cross section of a previously prepared TEM sample, which provided much needed additional information regarding in-situ experiments, especially the ability to determine oxide depth and structure.

In the figure 22, an example cross-section sample from an ultrafine-grained titanium TEM sample is shown. This sample underwent a rapid heating experiment, and as can be clearly seen, the sample clearly shows the layered structure of a cross sectioned sample. Top of the sample is the remaining ion beam deposited platinum, followed by the thin electron beam layer, with a

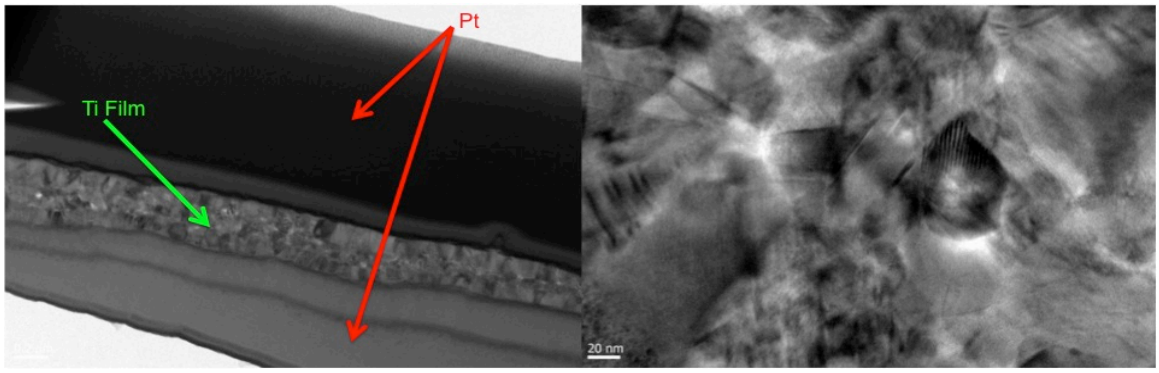

Figure 22: Cross sectional sample made from a FIB prepared lift out from a UFG titanium. Image on left shows cross section structure including the multiple layers of platinum protection. The image on the right shows high magnification of the titanium film area and the many grains present in the UFG sample.

final very small layer produced by the sputter coating process. After this, we see the cross-section of the previous TEM sample illustrating the multiple grains through thickness in the thicker regions of the sample ranging for ~200 nm to 300 nm. Below the cross section, there is some redeposition present in the gap present between the Ti layer and Si substrate as a result of this sample not laying completely flat on the substrate. On

the right, a higher magnification image of this sample is shown to illustrate the low amount of damage caused to the sample during the cross sectioning process.

Figure 23 shows two in-situ oxidized samples of Zircaloy-4 that have been cross-sectioned following oxidation experiments, illustrating the different conditions that can be identified by cross-sectioning in-situ samples. Figure 23A shows the bright field TEM image from the region where the precession diffraction scan in 23B was taken to determine oxide phase and thickness of a sample not oxidized through thickness. This precession diffraction phase map in 23B indicates the oxide layer present top and bottom on the sample is majority monoclinic ZrO_2 with remaining base metal of HCP zirconium between the two oxide layers. Below in figure 23C is a sample that was oxidized in-situ through thickness. In this sample, we see the majority phase is still monoclinic ZrO_2, with minor remaining areas of tetragonal ZrO_2. Furthermore, we see for this sample oxidized through thickness that the oxide structure is columnar in nature (figure 23E), and that there is cracking present in the sample that would run parallel to the oxide-metal interface. In figure 23F, a high-resolution image is shown at one of the crack tips present in the through thickness oxidized sample, with little evident FIB damage. Both of these features would not be visible had the sample not been cross sectioned, and the precession diffraction maps would not have shown the layered structure difference between the sample oxidized through-thickness in figure 23 C-F and the figure only surface oxidized in A-B.

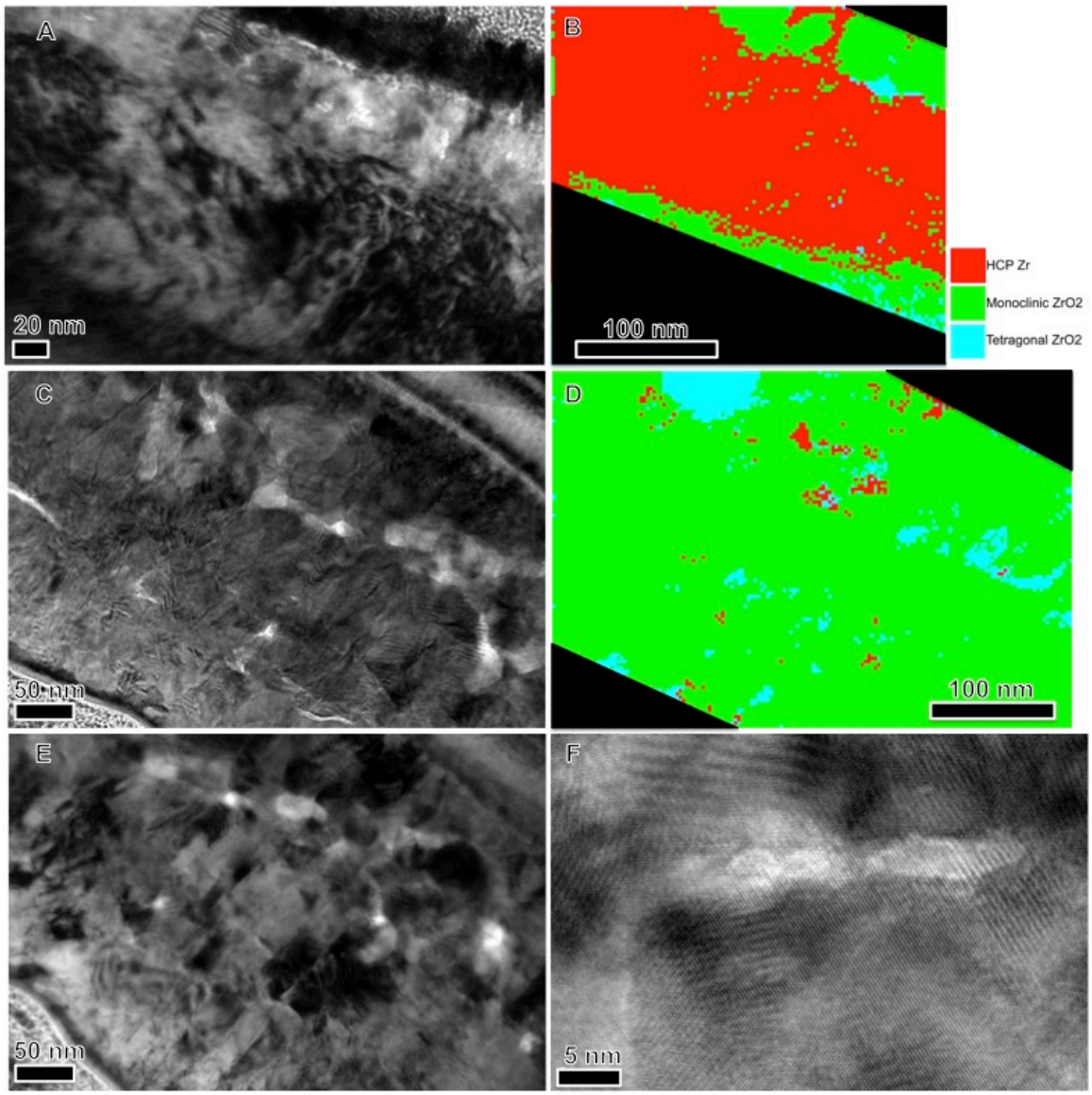

Figure 23: A) Image showing region of partially oxidized cross section sample that precession diffraction scan was taken from. B) Phase map for region pictured in A. C) Region of precession diffraction scan was taken in through-thickness oxidized sample. D) Phase map from region in C. E) TEM image showing columnar grain structure in through-thickness oxidized sample. F) High resolution TEM image of crack tip present in cross section of through-thickness sample.

By using this cross-section technique, it has been possible to refine the in-situ oxidation parameters in such a manner as to capture both partial sample oxidation and through thickness sample oxidation as well as observe the as grown oxide structure. Continuation of this work will focus on targeting specific features in in-situ TEM samples through the

use fiducial marking. This will prove to be a challenging undertaking, as a method will need to be devised that will not interfere with TEM imaging, but is also readily visible in the FIB during the cross sectioning and thinning processes. A simple electron beam platinum deposition slightly away from the area of TEM interest has been considered, but lacks contrast compared to the protective platinum strap laid during the sample preparation process. Utilizing a second gas injection system with a different material may solve this problem and allow for the placement of fairly accurate fiducial marks, which would allow for a site specific in-situ TEM experiment followed by a cross sectional examination of the region with thinning based upon the previously placed fiducial marker.

Going forward, this technique has great potential for allowing the correlation of oxide structure and phase at various points, building a 3D understanding of corrosion as it occurs, which will help improve modeling input to improve alloy design. This technique will serve to bridge the length scale gap between EBSD serial sectioning and atom probe by allowing for the use of TEM to gain similar information to EBSD when used in conjunction with precession electron diffraction and atom probe when EELS is utilized. By utilizing this cross sectioning technique in conjunction with precession diffraction, much finer scale details[125] can be resolved as compared to EBSD[126]. This technique is limited compared to EBSD in the field of view, as a TEM sample provides much less area than is accessible in EBSD, however greater precision is available in TEM. When compared with atom probe tomography, this technique allows for crystallographic information to be gathered as well as elemental information when combined with EELS over a much larger region than with atom probe tomography[127], however elemental resolution as compared to atom probe will be microscope dependent. In zirconium-based

alloys, this technique allows the use of EELS for similar observations regarding oxygen penetration to those made by de Gabory et al. [128] using a combination of EELS and atom probe tomography, however a much larger sample area is available, allowing for observation of the effects of base metal orientation as well as alloying element response. When a sample is oxidized in-situ in the TEM under well-controlled conditions, the change in sample thickness can be measured using low-loss EELS, and then correlated to oxide thickness and oxygen diffusion once the sample is cross-sectioned. Because of this controlled oxidation environment combined with the ability to view the sample in cross section, a better understanding of the formation of the blocky sub-oxide structure described by a number of authors can be obtained[23,60,129]. In addition, the depth of oxygen diffusion can be correlated to the oxidation time and oxygen partial pressure, providing improved insight into the kinetics of this process. If a relatively large grained material is used, the oxide-base metal orientation relationship can also be determined, allowing for improved modeling of orientation effects on initial oxidation rate. By knowing the effect of orientation on oxidation rate, techniques such as grain boundary engineering can be used to improve the overall oxidation resistance of the alloy.

We present a new technique for further analyzing TEM samples that have been used to conduct in-situ experiments, to gain better insight into changes occurring parallel to the electron beam during the experiment. By cross-sectioning TEM samples used during in-situ oxidation experiments, we have shown that these in-situ oxidation experiments replicate the oxide structures and phases present in long-term testing[119], and that this method is not significantly hampered by thin film effects. The process described herein is not limited to just oxidation samples, and is universally compatible with samples used in a MEMS-type holder system. This method opens the door to further examination

of in-situ TEM samples that would otherwise be discarded and helps improve the usefulness of MEMS-type holder systems.

3 In-situ corrosion study of Zirconium-based alloys

After development of the controlled-environment TEM holder and associated sample preparation techniques, I used the holder for studying the initial corrosion behavior of Zirconium-based alloys, specifically pure Zirconium and Zircaloy-4. Pure Zirconium was used to act as a good model system, with no secondary phase precipitates or stress in the matrix, and should also provide faster oxidation behavior. Zircaloy-4 is more representative of the alloys used in-service as nuclear fuel rod cladding as discussed before, and contains several alloying elements and an improved oxidation behavior as compared to pure Zirconium.

Since autoclave-corroded samples are known to replicate the corrosion behavior observed in a reactor environment, autoclave-corroded samples will be used as a standard to which samples oxidized in-situ in the TEM will be compared. This will allow for understanding whether thin lamella can be used to replicate the corrosion behavior observed in bulk scale experiments that are known to replicate in-service behavior. These studies were conducted using autoclave-corroded samples provided by Arthur Motta's group at Penn State University. TEM samples were prepared in both plan view and cross-section from the autoclave samples via standard FIB preparation. These samples were then characterized using bright field TEM, diffraction, and precession diffraction. These results were compared to what is observed using the same techniques on the in-situ corroded samples. It is expected that the structure and the oxide composition can be

replicated in the TEM, although it required extensive work to tailor the oxidation parameters as a result of working with thin TEM foils.

After confirming that a thin lamella can be used to successfully replicate the bulk scale oxidation behavior, the focus of the study was shifted to understanding the initial corrosion behavior of the zirconium alloys. The first challenge that was encountered during this study was the optimization of the in-situ experiment parameters such that the first stages of oxidation can be observed, and the experiment can be stopped at partial oxidation of the lamella. Ideally, these experiments will allow for observation of where corrosion first occurs in the samples, whether this be at grain boundaries, second phase particles, or other locations. This allows for the determination of whether certain orientations are more oxidation resistant than others. High angle grain boundaries allow for fast diffusion, and as such were expected to be the point of oxide nucleation.

Once the conditions have been determined so that oxidation can be stopped at the initial oxidation layer, the composition and structure of the oxide will be studied using EELS, selected area diffraction, and precession diffraction. Attempts will be made using FIB to make cross-sectional samples from the in-situ lamella following oxidation experiments in order to determine the structure of the oxide that is formed during the in-situ experiments. As was mentioned earlier, in autoclave samples oxide structure can be either columnar or equiaxed, with tetragonal ZrO_2 generally being equiaxed while monoclinic ZrO_2 grows in a columnar structure. By making a cross-section of the lamella, it should be possible to see if the structure formed in-situ matches that formed in an autoclave. Due to the sample being very thin for TEM, the structure may not be the same as what is seen in an autoclave, as there will be less stress in the sample to stabilize the formation of tetragonal ZrO_2. In addition, the sample thickness may prevent

identification of columnar versus equiaxed growth. Monoclinic ZrO_2 in an equiaxed structure is expected to be the initial structure, as there will be a lack of stress to stabilize the tetragonal ZrO_2, however oxide growth rates may make this difficult to ascertain.

3.1 Oxidation Parameter Development

The initial focus of my work was on developing a suitable set of parameters for studying the oxidation behavior of zirconium-based alloys at the nanoscale using TEM. Since almost all oxidation studies in this system are conducted in bulk or near bulk, this meant finding a suitable time, temperatures, and oxidation environment for an in-situ TEM study. The alloy used for this development was Zircaloy-4. Dr. Arthur Motta's group at Penn State University provided a pristine sample of Zircaloy-4, along with an autoclave-oxidized sample of Zircaloy-4.

Table 1: Nominal composition of Zircaloy-4

Sn	Fe	Cr	Ni	Zr
1.2-1.7%	0.07-0.20%	0.05-0.15%	<0.007%	Balance

The nominal composition of Zircaloy-4 is given in table 1. The oxidized sample was subject to 225 days in an autoclave at 360°C under 25 MPa of pressure in pure water. One of the first challenges encountered was how to observe the oxidation process, as it

was unknown what the best oxidation and imaging conditions would be. Oxidation conditions for replication of autoclave and reactor oxidized experiments were unknown because of the expected difference in oxidation of essentially a thin film as opposed to a bulk sample. Also, because almost all past experiments in this field were conducted ex-situ, there was little precedent to know what the appearing features should look like. Initial experiments were conducted using conventional TEM, with the thought that changes in contrast would be easily visible due to different diffracting conditions in the new oxides, under an environment of room atmosphere at 1 atm of pressure at 360°C. These parameters were chosen to provide for easily changed imaging conditions, to simplify the desired atmosphere, and to have an identical temperature to both the autoclave samples provided and many bulk studies. Figure 24 shows the results of the

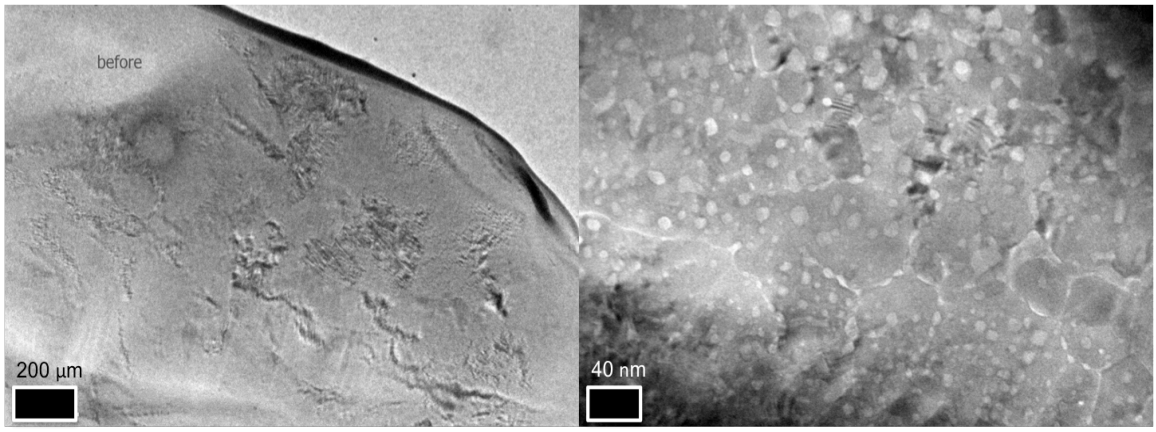

Figure 24: Bright field TEM image of initial oxidation experiments, showing initial pristine condition at low magnification on left, and high magnification after long oxidation time at high temperature on right. In order to evaluate oxide thickness and structure, clearly these samples need to be viewed in cross section.

initial experiment, with a low magnification image taken prior to oxidation, as it was expected that the oxidation process would happen rapidly in this thin film and be easily visible. This turned out to not be the case, as the sample was initial oxidized for 30

minutes at room atmosphere and 360°C, but no evidence of oxidation was seen. At this point, the temperature was increased slowly until 800°C was reached over the course of approximately 3 hours. Since there was still no readily visible oxidation at low magnification as was expected, the sample was cooled, and high magnification images were taken, as seen on the right in figure 24. These images showed that at some point during the experiment, oxidation had clearly occurred, based on the easy with which new grain boundaries or cracks are easily seen in the image, along with small crystals appearing, neither of which were present during the initial characterization of the sample. The presence of oxide was confirmed using selected area diffraction, since the problems with precession diffraction had not yet been solved at this juncture. Furthermore, the oxide structured and phase could not be adequately determined, as cross sectioning of the sample would be required to determine these pieces of information, and this is what drove the development of the cross section technique discussed earlier.

Based on this initial experiment, it was concluded that a significant change in parameters was in order, as 3 hours would be an excessive time to try and study the oxidation behavior over without knowing when the process was occurring. This resulted in a change of gas composition to a 50-50 mixture of oxygen and argon to hopefully accelerate the corrosion process by providing an aggressive environment, as well as ensuring that the oxidation process was not being restricted by a lack of oxygen present in the cell.

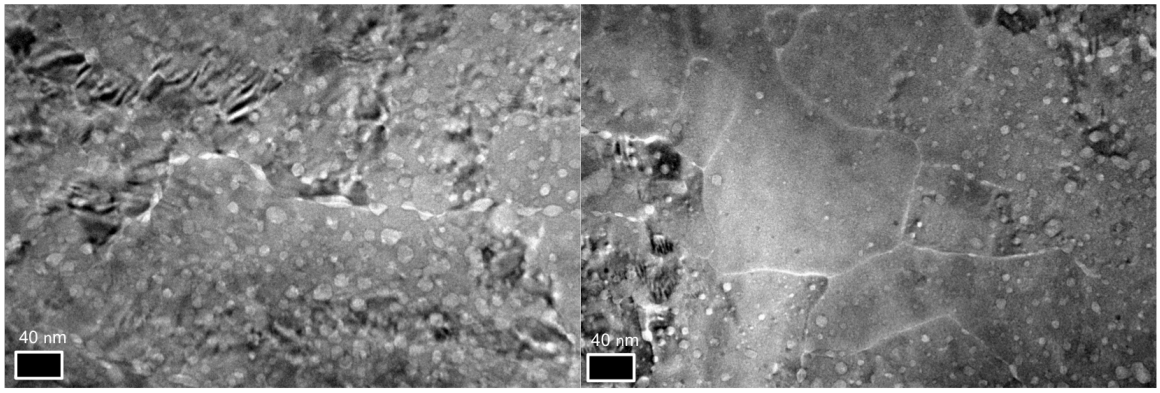

Figure 25: Bright field TEM images following an in-situ oxidation experiment at 800 °C in a 50-50 O_2-Ar gas mixture.

Another experiment was conducted using the new gas mixture with the same conditions as before, and again no significant change to the sample observed at the lower temperatures over long times. Once again, the experiment parameters were altered to increase the oxidation rate in order to hopefully increase the visibility of the process as well as reduce the time to a more reasonable time for an in-situ experiment. This time, temperature was increased to 800°C, and once again no significant changes were observed, until very high magnification was used to examine the sample. As seen in

figure 25 this higher magnification showed what appeared to be a very distinct grain structure having formed in the sample, along with smaller crystal-like spots in the grains. About this time, the problem of doing precession diffraction through the multiple windows was solved by the acquisition of gas plugs for this holder. Precession diffraction was then used to confirm the presence of both monoclinic and tetragonal ZrO_2 in the oxidized sample.

At this point, it was desired to do multiple experiments at these same parameters of a 50-50 mixture of oxygen and argon at 800°C. However, at this point it was found we had a significant problem with experiment reliability. After the initial sample, multiple samples were lost during the course of the experiment, often starting to move in the TEM image, and then crashing the microscope due to failure of the SiN membrane in the E-chips. Why this was happening was unclear, until another sample was heated for a separate set of experiments, and the platinum protective strap was observed during heating. At approximately 700°C, the platinum protective layer began to crystallize, and by 800°C, the layer had completely crystallized and densification into a very thin layer at the top of the sample.

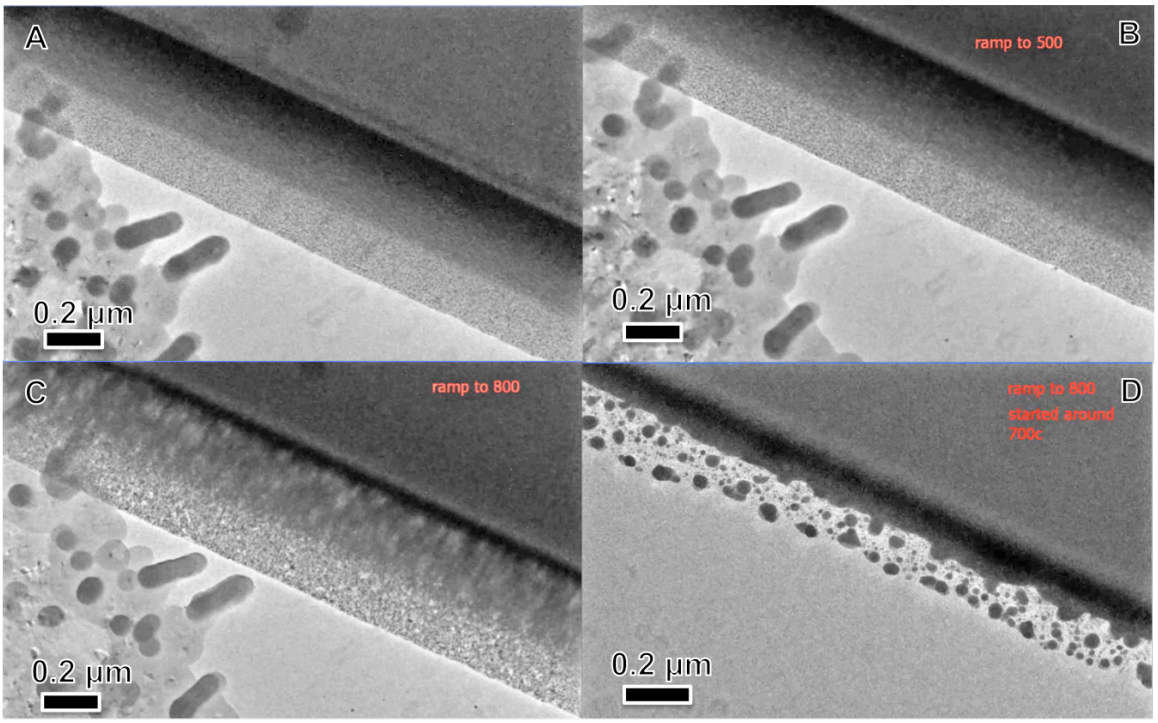

Figure 26: Screen captures showing the crystallization of the platinum protective layer deposited using FIB. A) Shows initial condition of the sample. B) Shows little change after heating to 300°C C) Beginning of the crystallization during heating to 800°C at around 700°C D) Platinum layer during rapid crystallization and densification

This processes is shown in figure 26, ending just before final densification of the platinum layer. Since the samples are attached to the E-chip using the same type of deposition, it became clear that the failure mechanism for the experiments was the platinum welds failing, then the sample moving and touching the already loaded SiN membrane causing failure. As such, the oxidation parameters needed to be adjusted such that this problem could be avoided.

Based on the prior experiments, the environment was kept constant, with the temperature being lowered first to 650°C, as this was well below the crystallization temperature for the FIB deposited platinum but still relatively high so oxidation should happen rapidly and provide the most distinct change in the sample possible. At this

point, my technique for cross-sectioning FIB prepared samples had been developed and tested, so much more information about the samples following oxidation could be accessed. It was found that for the short time desired for the in-situ experiments (~10 minutes), oxidation occurred through thickness, so the temperature was again reduced, drastically this time to 300°C. After multiple experiments at 300°C, it was found that for Zty-4, the combination of this temperature in a gas mixture of 50% argon-50% oxygen was ideal, as samples could be reliably partially oxidized in about 7.5 minutes, with through thickness oxidation occurring in 10 minutes.

Following the establishment of a reliable set of oxidation parameters for zirconium-based alloys, the next major question for oxidation parameters whether they are valid at least a starting point for other material systems. This is an important step in developing this technique, as it will prove the universality of this technique to any bulk metal system. As such, samples of 316L stainless steel were procured and TEM samples were prepared using the previously described FIB preparation method. All samples were prepared from grain boundaries found using ion-channeling contrast in the FIB, however no specific boundaries were chosen for these experiments. The stainless steel system provides a great initial test, as there have been a large number of studies into the oxidation behavior of this material system, with a majority of studies in 304L and 316L, due to its common application in almost every environment. Environments that have been studied include supercritical water[130,131], oxygen[132], air[132,133], and water vapor[134]. Thus, between our experiments and the data available in literature, it should prove easy to identify whether these oxidation parameters are reasonable. As such, the initial experiment was conducted at the same parameters as used above in zirconium-based alloys, 300°C in a gas mixture of 50% argon-50% oxygen. This 300°C correlates well

with some past studies in 304L stainless, such as the work by S. Ghosh et al where the initial oxide structure was examined using in situ contract electrical resistance and electrochemical impedance spectroscopy[131]. While this study does provide a similar temperature, the time used for oxidation was in the hundreds of hours, a timespan not suitable for in-situ TEM. In addition, the alloy I was using was a modified 316L with a higher nickel and chromium content than normal, so as such, during the initial experiments at these lower temperatures, we expected no significant change in the samples. The exact composition of this 316L is given in the table below.

Table 2: Composition of modified 316L provided by Carpenter Technologies for corrosion testing

Element	Ni	Cr	Mo	Si	Mn	C	P	S	Fe
wt%	14.74	17.41	2.82	0.45	1.85	0.024	0.014	<0.001	Bal.

This did indeed prove to be the case, that there was no discernable oxidation after approximately 20 minutes at temperature. In order to rapidly identify the appropriate temperature, the temperature was then raised to 600°C, which is in the mid range of the temperatures used in this field, below that used by Kim et al[134], but above that used by Sun et al[130]. The result of this temperature increase was a remarkably fast oxidation of the TEM specimen, which occurred in a few seconds of time prior to reaching the 600°C set point. Thus, I revised my oxidation parameters for the next sample to be 400°C, above the initial temperature of 300°C where no oxidation was visible, and below 600°C, where oxidation occurred too quickly for good observations. This change in temperature proved to be ideal for observing oxidation, as the sample oxidized over a period of 11 minutes, including time to reach temperature and time to cool back to room temperature.

Following this experiment, the samples were examined in the FIB to examine the surface morphology and compare the results to common ex-situ experiments.

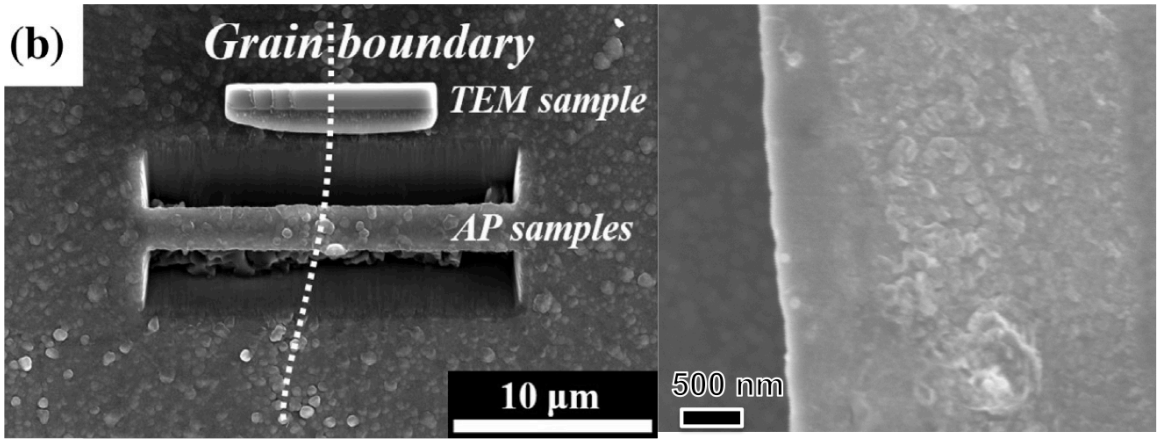

Figure 27: Image comparing in-situ TEM oxidized FIB sample(right) to an autoclave oxidized sample from the work by Kim et al. (left) showing the very similar oxide structure seen in the two cases.

As seen in the figure above, the morphology of the in-situ sample compares very well to the ex-situ work of Kim et al, with very similar appearances of a blocky oxide structure uniformly coating the base metal surface. While ideally the oxide structure would be correlated using precession diffraction to confirm phases, unfortunately the high level of diffraction that is given off by stainless steel means that any procession diffraction scans taken simply show the base metal, not the oxide, as is discussed later. It should be noted that the oxide texture is much finer in the in-situ sample, however this is to be expected, as the in-situ sample is a FIB lift out that was oxidized for a much shorter period of time. The ex-situ sample to which I am comparing was oxidized for 30 minutes at 700°C, where as the in-situ sample was only oxidized for a little over 10 minutes at 600°C. Overall, this experiment served to provide us with a good validation for our oxidation parameters. The fact that one can resolve a reasonable set of in-situ oxidation parameters

within a couple of experiments bodes well for the future of this technique in a variety of systems. Soon, this same technique using these parameters will be employed to look at the initial oxidation behavior in high entropy alloys, where in-situ TEM will prove to be valuable in understanding how the precipitation of various phases during oxidation affect the overall oxidation of the alloy.

3.2 Imaging Conditions for in-situ Oxidation Experiments from Bulk Metals

During the course of the oxidation parameter refinement, changes in imaging conditions were conducted so that the oxide could be better observed. In TEM, there are many different possible techniques to try, including bright field, dark field, diffraction, high angle annular dark field, and energy filtered TEM. Only the first 3 techniques were available for most of my work, with the last two techniques becoming available in mid 2016. Every technique relies on contrast from different mechanisms, and one of the major challenges presented by in-situ oxidation is that the oxide forming on the sample surface will grow in a direction parallel to the beam. In addition, the oxide forming will most likely have an orientation relationship to the base metal, so the diffraction contrast will be limited by how significantly the crystal structure of the oxide varies from the base metal. Finally, as a result of heating the sample, there will be drift of the sample within the microscope that will need to be compensated for. All of these factors added together make for a very difficult imaging situation, with each imaging condition being limited by different factors.

Dark field imaging requires a proper tilting of the specimen such that the image generated is from a specific spot in the diffraction pattern. For the in-situ oxidation case,

one must be able to correctly guess the orientation of the oxide that will grow on the base metal, in a specific area and tilt the sample as well as align the selecting aperture correctly for gathering one specific spot while also accounting for the bending of the sample/window during heating that occurs during the experiment. Drift also plays into account here, as when selecting where it is guessed the oxide spot will appear, the diffraction from all other spots is filtered out, resulting in no image with which to compensate for drift during the experiment. In the end, for an oxidation experiment in these zirconium-based alloys, where little is known about the exact initial oxide-metal relationship, dark field TEM is a literal shot in the dark, with low chance of success.

Selected area diffraction is a technique that is commonly used for crystal structure and identifying phases within a material. For the task at hand, on the surface this seems like an ideal technique, as one of the fundamental questions to be answered is what phase and orientation first form during oxidation. However, this technique is once again limited because of the in-situ experiment. First, for the best information, the sample needs to be tilted to a zone axis, which may be difficult or impossible depending on the sample and the single tilt axis available in the environmental holder. Next, the problem of drift again comes into play, as the sample cannot be observed while recording diffraction information. It is easy to tell the sample is moving, as the diffraction pattern changes as the beam crosses various boundaries, but there is no indication of which direction the sample is traveling, or at what rate. In addition, this is complicated by the formation of the oxide, because the question arises of is the shift in the diffraction pattern the result of oxidation, or drift? Since often diffraction patterns are difficult to match on the fly at a guess, this problem is very significant. Finally, if a diffraction pattern is later analyzed to show both oxide and metal present within the sample, it only tells that both

phases are present, not location. As such, a pattern could show oxide, but there is no way of knowing if the oxide is on top or on bottom of the sample, let alone if the oxide is preferentially forming on one side of a grain boundary versus another.

Bright field TEM is the most widespread TEM technique, with an image being created from the diffracted electron beam, including the central spot. As such, this technique is allows for a complete image of the sample, not just specific areas, as is the case with dark field. On the positive side, this means it is easy to compensate for sample drift during the experiment. However, this also means that there is information being generated from the underlying base metal, which can provide stronger signal than the growing oxide, masking the oxide from providing contrast in the image. To help limit this problem, high contrast apertures can be inserted. These apertures limit the number of diffraction spots used to generate the image, and with the Zircaloy and pure Zirconium samples it was found the best contrast was generated using the 3rd high contrast aperture, which is the next to smallest aperture. This aperture limited the diffracted spots used to generate the image to the most central spots in the pattern, and significantly helped with the ability to observe the oxide formation. That said, this did not completely solve the problem of having good contrast throughout the growth process, as the base metal still provided a large amount of signal relative to the oxide, and it was seen in the videos recorded of the oxide growth that as the oxide grew, it appeared to come into contrast, and then snap out of contrast suddenly. I attribute this appearance of contrast to the oxide starting out as an amorphous layer on the base metal, but once the oxide is thick enough to form a crystal, it assumes an orientation related to the base metal orientation, and then contrast is lost because the diffraction from the underlying base metal is much stronger than the diffraction from the oxide, and with the two phases having similar

orientations, there is little to differentiate the two phases. That said, bright field TEM provided the best contrast for most of the experiments conducted when using the 3rd high contrast aperture.

High angle annular dark field and energy filtered TEM both became available in mid 2016 with the commissioning of the JEOL 2100 FEG at Drexel with ultrafast electron energy loss system installed. As such, limited work was done with both of these techniques. Each technique provides a unique opportunity for information with regards to corrosion behavior. In the case of energy filtered TEM (EF-TEM), an image is generated based on electron selected for a specific amount of energy lost, indicating that those electrons interacted with a specific element. This allows for the generation of images showing how the distribution of specific alloying elements changes over time during oxidation. The problem with this technique is again that much of the signal generated is filtered out, with only a small subset of the signal being used to form the image. This is compensated for by rastering the beam over the sample multiple times to generate enough signal to create an image. In the case of in-situ TEM, this leads to poor time resolution, since each image takes a couple of minutes to generate. Thus, for the best results using this technique, the experiment tends to move away from true in-situ to more of a freeze frame type experiment, with short periods of heating to the sample, then cooling the sample and generating an EF-TEM image. In addition, this technique is reliant upon electron energy loss, which means the quality of information is very dependent upon the thickness of the sample. Ideally, for quantitative information, sample thickness needs to be less than 1.5 mean free paths in the sample being studied. The complications of trying to use this technique combined with the environmental cell will be

covered further during the section on studying the secondary phase particle effects in Zircaloy-4.

High angle annular dark field (HAADF) is a technique that relies on atomic mass and thickness to generate contrast. Contrast is generated using in-elastically scattered electrons, which is why this technique is very sensitive to mass and thickness. For in-situ corrosion experiments, this seems to be possibly ideal, as the sample will both increase in thickness, and the oxide will contain oxygen, which has a different weight than the base metal zirconium. The challenges are how much signal is generated via each mechanism, does the signal add or subtract, and how does gaseous oxygen interact compared to oxygen on the surface of the sample. This is also a scanning technique, however this technique just requires acquisition of a frame, not several frames to generate an image, as is the case with EFTEM and is thus a better choice of real time monitoring of a sample. Further discussion of this technique and its relation to oxidation experiments will be had in the section on secondary phase particles in Zircaloy-4

The final major challenge for imaging that was encountered with the in-situ oxidation experiments is determining if the sample has been oxidized through thickness. Since the oxide grows parallel to the beam, and in transmission there is no way to determine where signal is coming from, it is impossible to determine oxide thickness directly during an experiment. This is of importance because the tetragonal ZrO_2 phase is stress stabilized, and if the sample is oxidized through thickness there is some question as to how this may affect the stability of this phase. In addition, to see possible boundary and segregation effects, there needs to be base metal from the original sample remaining. Thus, it was necessary to develop the cross-section technique discussed above by which the final oxide thickness in the TEM sample could be observed. By using the technique I

have developed, it is possible, as seen in figure 24, to look in cross section at the TEM sample and determine the phases present in the sample, and to some extent the structure of the oxide present on the base metal.

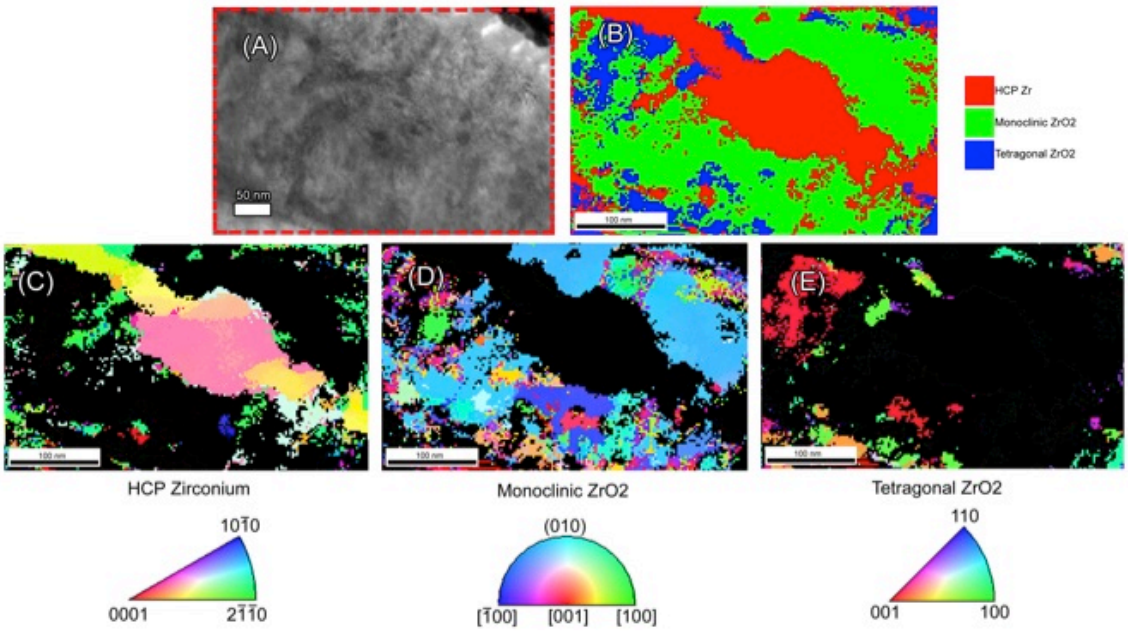

Figure 28: (A) Bright field TEM image showing the area of the cross sectioned sample from which the precession diffraction scans were taken. (B) Phase map generated from precession diffraction showing the almost complete oxidation of the sample in the region. (C) Orientation map for HCP zirconium. (D) Orientation map for monoclinic ZrO_2. (E) Orientation map for tetragonal ZrO_2. Figure is reproduced from Harlow et. al[119].

This technique was invaluable for refining the parameters for in-situ oxidation experiments as now the oxide thickness could be observed, and precession diffraction used to characterize oxide. This technique also provided a positive identification mechanism for oxidation, even when the imaging conditions during the in-situ experiment appeared to show little oxidation, as once cross sectioned it is easy to identify oxide versus base metal as illustrated in figure 28 since there is no longer competing information sources for generating the TEM image. In addition, it is also being used to look for texture within the oxide formed during the experiments, as orientation

information is available from precession diffraction. However, it is possible that if the sample is thinned too much, stress may be relieved and the tetragonal ZrO_2 may no longer be a stable phase as will be discussed in a later section.

Precession diffraction also encounters some limitations for studying in-situ oxidation behavior and conducing phase identification; with the cross sectioning technique discussed about helping remove these shortcomings. When a sample is oxidized in-situ, the layered structure mentioned above comes into play, with the final layering being window, oxide, metal, oxide, window. Figure 29 shows a schematic of the beam path and resulting diffraction patterns.

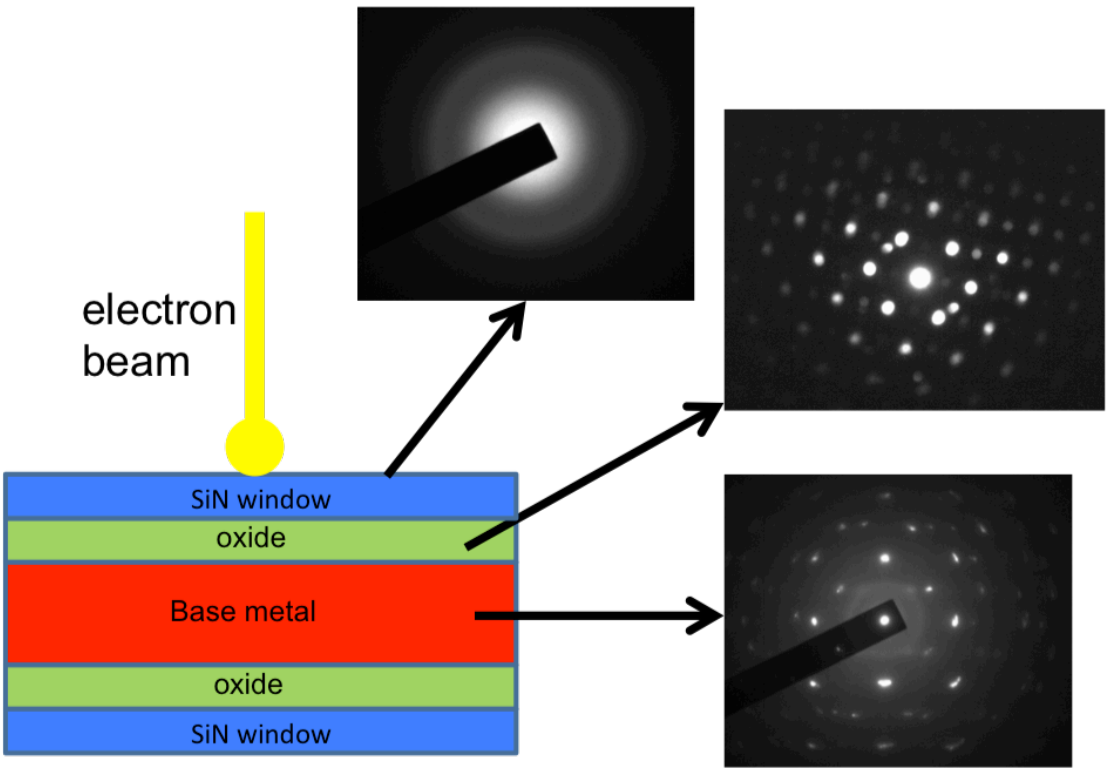

Figure 29: Schematic showing the multilayer problem for precession diffraction indicating the multiple different diffraction patterns that will end up overlapping.

As was discussed previously, the use of gas plugs for the TEM holder allows for removal of one of the windows, removing that pattern. However, there still remain multiple diffraction patterns, and the precession diffraction matching is not equipped to differentiate multilayered samples at this juncture. Instead, the software picks what it believes the strongest pattern is, and matches that pattern. Thus, in my work going forward, while plan view precession diffraction is presented, it is often further confirmed using cross sectioning of the sample.

3.3 Comparison of In-situ and Ex-situ Oxidation

After development of suitable oxidation parameters and imaging conditions, my studies shifted to confirming that in-situ oxidation using thin foil TEM samples did not differ radically from bulk autoclave oxidation samples. This work was conducted using Zircaloy-4 samples, the same samples used above for the development of the oxidation parameters.

3.4 Introduction to Zircaloy-4

Zirconium-based alloys have long served as nuclear fuel cladding, because of their resistance to corrosion and low neutron capture cross section [3,17,20,21]. The Zircaloy series of alloys in particular have been the most widely implemented in reactors, with much attention focused on the oxidation behavior of Zircaloy-2 and Zircaloy-4. Zircaloy-2 and Zircaloy-4 are differentiated mainly by the lower Ni and Fe content of Zircaloy-4[3]. While these alloys do possess moderately good corrosion resistance, uniform corrosion, along with the related hydrogen pick up, remains a life-limiting factor for fuel rod service[24,25]. Zircaloy-2 is mostly limited to use in Boiling Water Reactors (BWRs), where hydrogen pickup is less of a concern than in Pressurized Water Reactors (PWRs), in which Zircaloy-

4 is more commonly found. More recently, the Zircaloy series of alloys is being supplanted with alloys such as ZIRLO and M5, which have increased corrosion resistance due to the additions of niobium[20,26,27]. As the push to increase nuclear reactor efficiency continues, a better understanding of the oxidation behavior of these alloys is required for prolonged fuel service and for use in harsher environments that are dictated to achieve higher burn-up. In particular, Generation IV reactors will provide higher temperatures that will accelerate cladding corrosion, which will limit the achievable burn-up and thus efficiency[5].

The in-service lifetime of fuel rods is limited by material behavior, which is very dependent on microstructure and composition. In the case of the Zircaloy family of alloys, it has been shown that corrosion behavior is dependent upon both alloying additions and on the base metal phase. Past studies have illustrated that Zircaloys that are beta-quenched have superior corrosion resistance as compared to traditionally prepared Zircaloys[28–30]. Other studies have shown that crystallographic orientation has an effect on the oxidation behavior of zirconium-based alloys, with the base metal influencing the orientation of the oxide formed[18,32,33]. Grain boundary engineering techniques that change the microstructure are a viable method for increasing corrosion resistance[7,13–16]. In zirconium-based alloys, it has been shown that phenomena connected to corrosion, such as hydride formation, are heavily influenced by the microstructure such as grain boundaries and precipitates, and in-situ TEM can be used to study the initial mechanisms resulting in hydride formation[39]. The base metal microstructure has also been shown to have significant effects on the microstructure of the oxide formed during oxidation[31].

The oxidation behavior of these alloys has been extensively studied by a wide variety of methods. These methods include microbeam synchrotron diffraction[41–43], transmission electron microscopy (TEM)[19,32,44,45], scanning electron microscopy (SEM)[30,32,41–43,46], optical microscopy[41,47], and x-ray diffraction[43,46,47]. These techniques have provided an large knowledge base for the morphology and structure of the oxides formed on these alloys during corrosion, including cracking behavior[41,44], crystal structure[41,43,44,46], and the start of breakaway corrosion[5,49]. A wide variety of oxidation environments for zirconium-based alloys have been studied as well, including oxygen[78,79], steam[26,27,80,81], water[5,26,43], water vapor[78], air[48,82,83], with only changes in kinetics of oxidation being noted, and all studies showing similar oxide structures and appearances. The vast majority of these experiments, however, have been conducted using autoclave or reactor oxidized samples over long periods of time, which has prevented the direct study of the initial steps of corrosion. As such, while the oxide structure on corroded zirconium-based alloys is known to be composed of both of tetragonal and monoclinic ZrO_2, the structure of the initially formed oxide is not yet known. It is known that the oxide structure formed on zirconium-based alloys is highly textured, and that this may significantly affect the corrosion rate of the base alloy[5,36,41,45]. It is thought that the texture present in the monoclinic phase is the result of stress minimization, but how this texture affects oxidation rate is unknown[5,36]. Changes in texture of the oxide have also been attributed to the reformation of the protective oxide layer, but once again the effect on oxidation rate is not discussed[41]. More recently, it has been found that more strongly textured oxides provide better corrosion resistance, and there are preferred growth directions in both monoclinic and tetragonal oxides[45]. By studying the initial growth of the oxide in zirconium-based alloys, it may be possible to identify factors that lead to a

slower oxide growth rate, such as low angle grain boundaries which can be increased in number through grain boundary engineering[13]. If the oxidation rate can be reduced through grain boundary engineering, this will allow for a fuel rods to have a longer in-reactor lifespan, leading to higher burn-ups, and potentially safer storage of spent fuel. Thus, by studying the initial oxide structures and growth mechanisms, there is great potential for improvements in material performance.

In this section, I present a new method for studying the early onset of oxidation in Zircaloy-4. In-situ TEM results are compared to those obtained for the same alloy using an autoclave method, which is typically employed to study the long-term oxidation behavior of Zircaloy-4 and thus known to replicate the oxidation behavior seen in-reactor. Through the use of precession electron diffraction, selected area diffraction, and bright field transmission electron microscopy I show that this new method can be used to reasonably replicate the oxidation process that occurs in an autoclave. Precession electron diffraction allows for determination of grain orientation and boundary angle, which when coupled with in-situ TEM that provides the possibility of observation of the effect of these microstructural features on oxidation. In addition, this technique can be used to study the effect of alloy composition on oxidation behavior, including the effect of secondary phase particles. By controlling the environment, it is possible to achieve partial oxidation, allowing for the study of the initial oxide structures and texture effects during oxidation in addition to the in-situ observation of the sample.

3.5 Experimental Methods

Cross-sectional TEM lamellae were prepared from a pristine sheet of as-received, cold-rolled, stress-relieved alpha phase Zircaloy-4 (Zry-4) using a conventional focused-

ion beam lift-out technique [135] conducted using a FEI DB-235 and subsequently transferred to a Protochips environmental holder heating platform, known as a "E-chip", using an ExpressLO ex-situ lift out system. Samples were then attached to the platform using e-beam tungsten or platinum deposition in the FIB to secure and enhance the heat transfer from the E-Chip heating element during oxidation experiment. Lift outs from bulk material were made at random from the Zry-4 sheet, due to a combination of relatively small grain size, which ensured several grains within each sample and the difficulty of good EBSD in zirconium-based alloys[136] making targeting of specific boundaries very difficult. Through the use of precession diffraction, orientation information for the sample is readily available without the use of EBSD. During sample preparation, care was taken to minimize gallium damage from the FIB to the sample by placing a protective top strap of either platinum or tungsten over the region on interest, and a final clean up step following thinning was conducted using 5 kV gallium beam. These samples were also made a thick possible while remaining electron transparent for TEM, so as to help limit thin film effects on oxidation as well as through thickness oxidation. In addition, in-situ samples were compared to autoclave oxidized bulk samples to confirm similar oxidation behavior to bulk. Finally, a SRIM calculation was done for a 30kV ion beam at 0°, which gave an ion range of 16.7 nm. Figure 30 illustrates the sample preparation route for in-situ FIB samples, the image on the left shows sample after standard FIB preparation cut free for ex-situ lift out, ex-situ lift out to an E-Chip in the center, and final sample preparation through FIB deposition on the right.

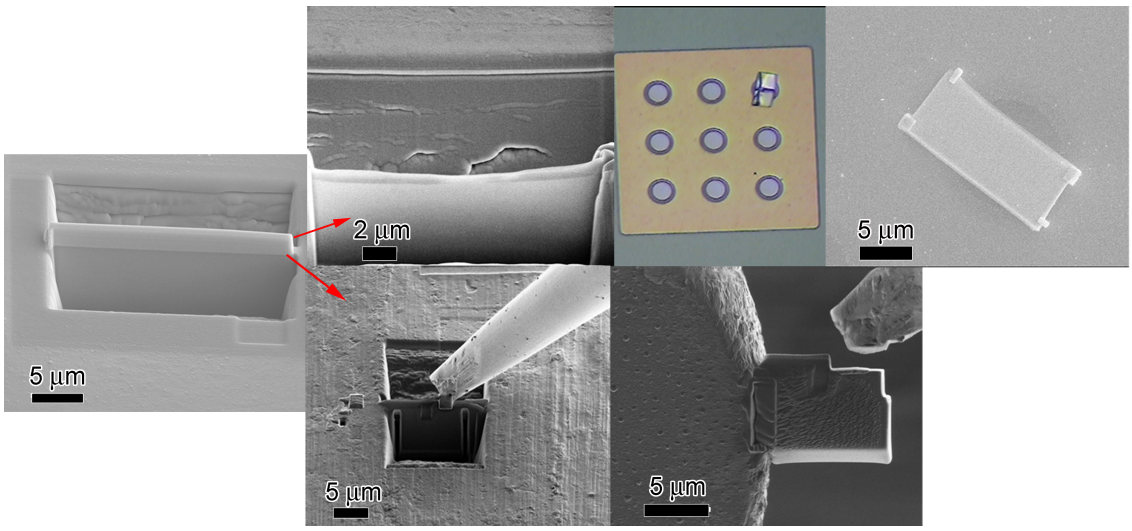

Figure 30: Top images show ex-situ sample preparation; sample is made and loose in FIB trench, sample is placed on E-chip, then attached to E-chip with electron deposited Pt. Lower images show standard FIB preparation as used with the autoclaved samples. Figure is reproduced from Harlow et. al[119].

For comparison to in-situ TEM, an autoclave-corroded sample of Zry-4 provided by Arthur Motta, which had been oxidized during a previous study for 225 days at 360°C [49], was prepared using conventional FIB lift-out techniques.

3.6 In-situ Characterization

The initial condition of the pristine samples of Zry-4 showed a large amount of deformation in the microstructure, with a random distribution of grain boundaries. This was confirmed using precession diffraction, as seen in figure 31, which shows bright field TEM images of a pristine sample before the oxidation experiment along with the corresponding phase map and orientation map generated using precession diffraction. The phase map confirms that pure HCP zirconium is the dominant phase throughout the sample, as expected for an un-corroded Zry-4 sample.

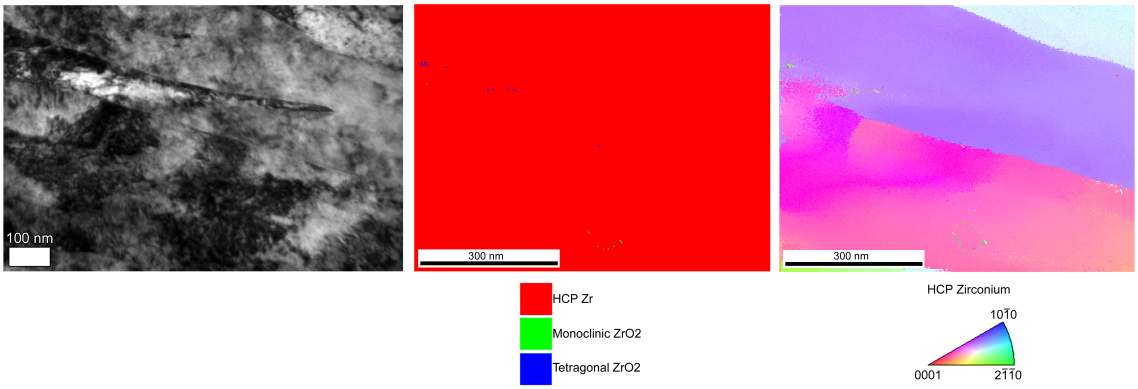

Figure 31: **Bright field TEM, orientation and phase maps from precession diffraction showing the starting sample condition. Figure is reproduced from Harlow et. al**[119]**.**

Since FIB lift outs were taken at random from the bulk sample, the boundaries present in the Zircaloy-4 samples were of a random distribution, with the orientation map showing an example of the multiple boundaries captured within a sample.

During the oxidation experiment, it was seen that the sample increases in thickness as oxide forms, reducing contrast in the TEM image.

Figure 32 Snap shots from an oxidation experiment conducted at 650°C, showing (A) the start of the experiment, (B) midpoint of the oxidation with small oxide grains forming and a loss of contrast in the base metal microstructure, and (C) the final state of the sample showing small oxide grains obscuring the underlying microstructure. Figure is reproduced from Harlow et. al[119].

Small grains formed during the experiment, with the microstructure of the underlying sample remaining stable, although difficult to discern due to decreased contrast. Figure 32 shows snapshots of an in-situ oxidation experiment and illustrates the appearance of small oxide grains, as well as the decrease in contrast resulting from increased thickness. The initial sample condition is shown in (A), image (B) shows the midpoint of the experiment, with contrast starting to be reduced and small oxide grains beginning to dominate, and at the end of the experiment on the right (C) it can be seen that both contrast is reduced to almost nothing in thicker areas of the sample, and the underlying microstructure of the base metal is obscured by many smaller oxide grains formed on the sample surface. It is clear that the sample oxidized over the course of this experiment, as many smaller grains can be seen in the final image (C). This is to be expected during the oxidation process, based on the work of many past researchers who report small grain sizes in the oxide during corrosion[44,45,137,138]. Figure 33 illustrates the oxidized sample after heating under presence of oxygen where clear changes in morphology can be

observed. Following the oxidation experiment, precession diffraction was used to create a phase map of this region of the sample, as seen in figure 33. It was seen that the oxide formed as a mixture of monoclinic ZrO_2 (green), tetragonal ZrO_2 (blue), and some base metal of pristine HCP Zr (red) possibly remaining.

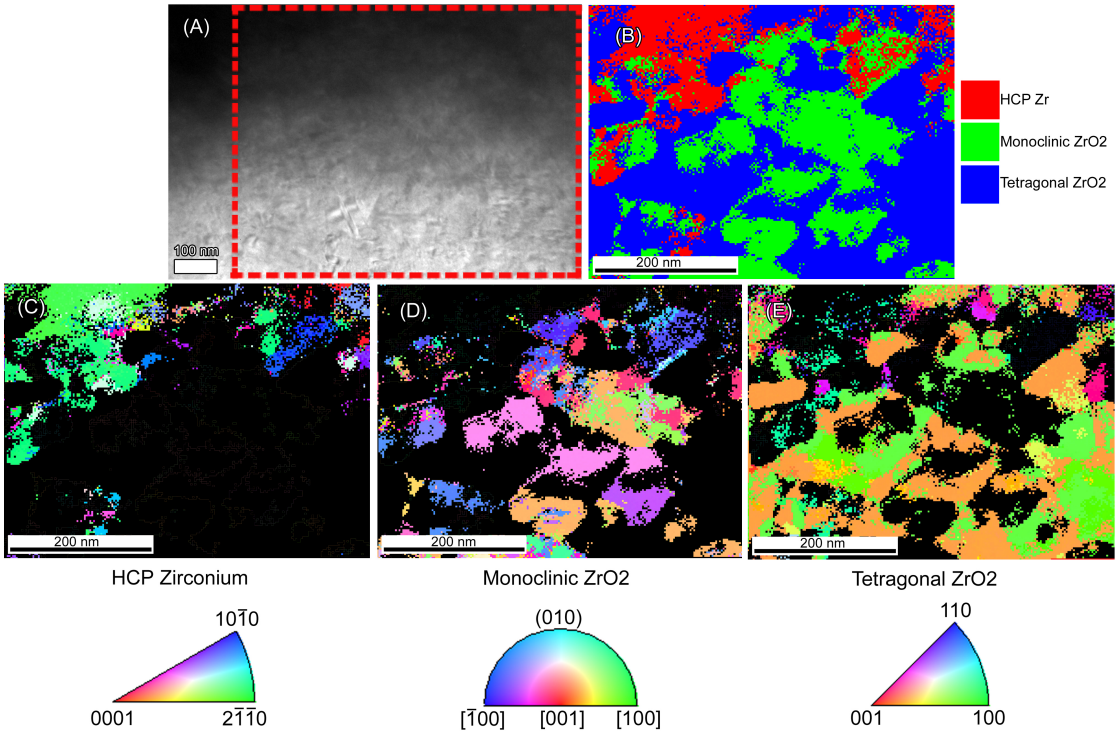

Figure 33 Bright field TEM image on the left shows the region over which the phase map on right was generated. The phase map shows the sample to have mostly oxidized to form monoclinic ZrO_2. This sample was oxidized at 650°C. Figure is reproduced from Harlow et. al[119].

Past work done in both autoclave and rector oxidized samples from a variety of authors confirms that the majority phase expected following oxidation is monoclinic ZrO_2, as this is the stable phase of ZrO_2 at room temperature, along with a limited amount of tetragonal ZrO_2[5,41,44,45,138]. However, past work utilizing both XPS[37] and synchrotron x-ray diffraction[42] indicate that the initial oxide layer may be composed of a

majority phase of tetragonal ZrO_2. As is seen in figure 33(E), the in-situ experiment agrees well with these studies, showing what appears to be a relatively high concentration of tetragonal phase. Orientation maps created using precession diffraction, as shown in figure 33, indicate that there is some evidence of texture in the tetragonal ZrO_2, however it appears that the monoclinic ZrO_2 does not show a strong texture. However, there is not a sufficient sample size for conclusions on oxide texture. As for the HCP Zr base metal, most of the remaining base metal is of one orientation, indicating there may be orientation effects on the rate of oxidation, which is expected based on the work on Ploc[18]. In addition, samples oxidized in-situ were compared to autoclave oxidized samples to confirm the similarities in oxidation behavior and oxide structure.

3.7 Comparison of in-situ and autoclave samples

Autoclave oxidized samples were studied using the same methods as the in-situ samples to provide a direct comparison. As such, Figure 34 shows a phase map (B) and corresponding bright field image (A) for the ex-situ oxidized sample (autoclave-corroded) to compare to the in-situ samples.

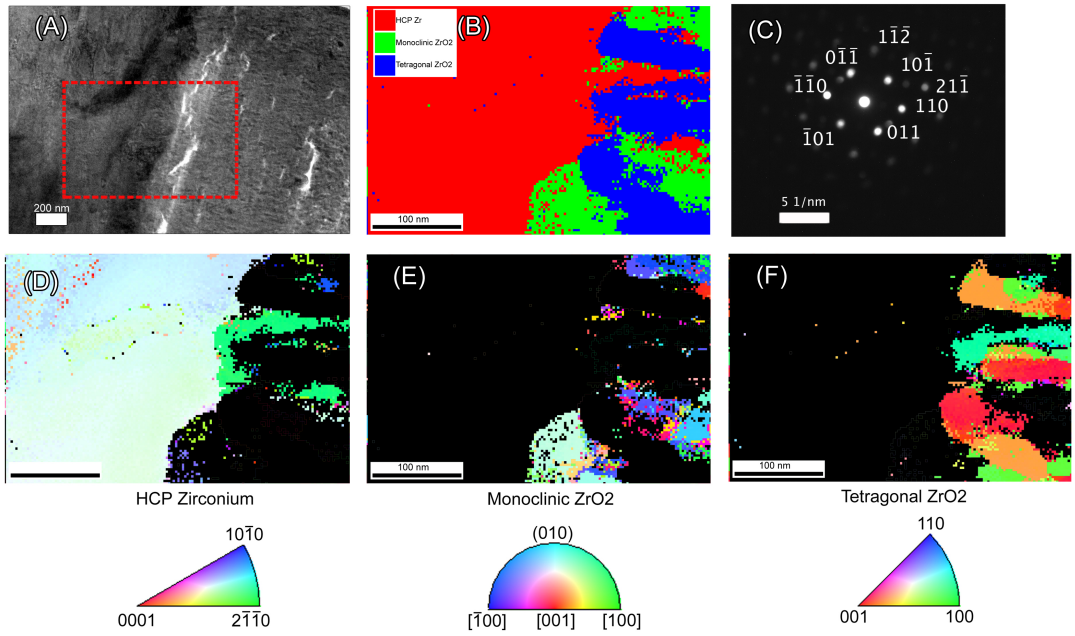

Figure 34: Analysis of an autoclave-oxidized sample at the oxide-metal interface. (A) Bright field TEM image showing the precession diffraction area. (B) Phase showing phases present in the precession area.. (C) Nanobeam diffraction pattern taken from the autoclave sample showing the presence of monoclinic ZrO_2. (D) Orientation map for HCP Zr (E) Orientation map for monoclinic ZrO_2 (F) Orientation map for tetragonal ZrO_2 all from the precession area in (A). Figure is reproduced from Harlow et. al[119].

The phases present in the autoclave corroded sample correspond well to the results from the in-situ samples, showing a distribution of the two oxide phases, monoclinic ZrO_2 with areas of tetragonal ZrO_2. Small columnar grains of ZrO_2 are visible growing from the base metal, which again shows good agreement with what was

seen for the in-situ experiments. This shows that the oxidation process being observed in the TEM is similar to the oxidation process that has been well studied in long term autoclave and in-reactor tests by a variety of authors[17,41,44,45,138]. The orientations seen in the in-situ sample also mimic the orientations present in the autoclave sample, with some texture present in the tetragonal ZrO_2 (figure 34F), and little to no texture present in the monoclinic ZrO_2 (figure 34E). In figure 34D, the underlying base metal shows only one orientation; this is most likely due to a small scan size.

3.8 Cross-sections of in-situ samples

When a cross section of an in-situ TEM sample oxidized at 800°C was made, it was seen that the sample had oxidized through the complete sample thickness (figure 35A-E). The phases present in the oxide were found to be a mixture of tetragonal and monoclinic ZrO_2, as see in figure 35B. The structure formed during the oxidation appears very similar to the oxide structure seen in the ex-situ sample (figure 34). Samples that are oxidized through thickness also show the distinct cracking behavior parallel to what would be the oxide-metal interface expected in this system, and also show the appearance of columnar type grains. Using the same technique, a cross section sample was made from the lamella oxidized at 650°C (figure 35F-J) and this sample appears to have been mostly oxidized, but small regions of pure unoxidized HCP zirconium remain within the sample in some regions. It should be noted that when characterized via precession diffraction in plan view (figure 33), this sample shows mostly oxides as the phases present, due to the stronger diffraction from the oxide as compared to the remaining base metal. In the standard plan view in-situ experiment geometry, the TEM beam passes through the sample. In the case of an oxidized sample, as was previously

discussed, this results in diffraction information being collected from multiple distinct layers in the sample: the top oxide surface, the base metal, the lower oxide surface and the SiN window background. During precession diffraction analysis, the strongest diffraction pattern is the matched or "chosen" for a given acquisition spot; in a typical oxidized sample, the oxide diffraction patterns are stronger and brighter than that of the base metal diffraction patterns in this system, and thus the diffraction analysis- both phase and orientation- is a reliable method to obtain a qualitative view of total oxide formed on the sample. When cross-sectioned (figure 35 F-J), it is possible to observe the remaining base metal in the sample and the overall distribution of oxide relative to the base metal. Strain relaxation during cross sectioning can occur, and is discussed in detail later in this section.

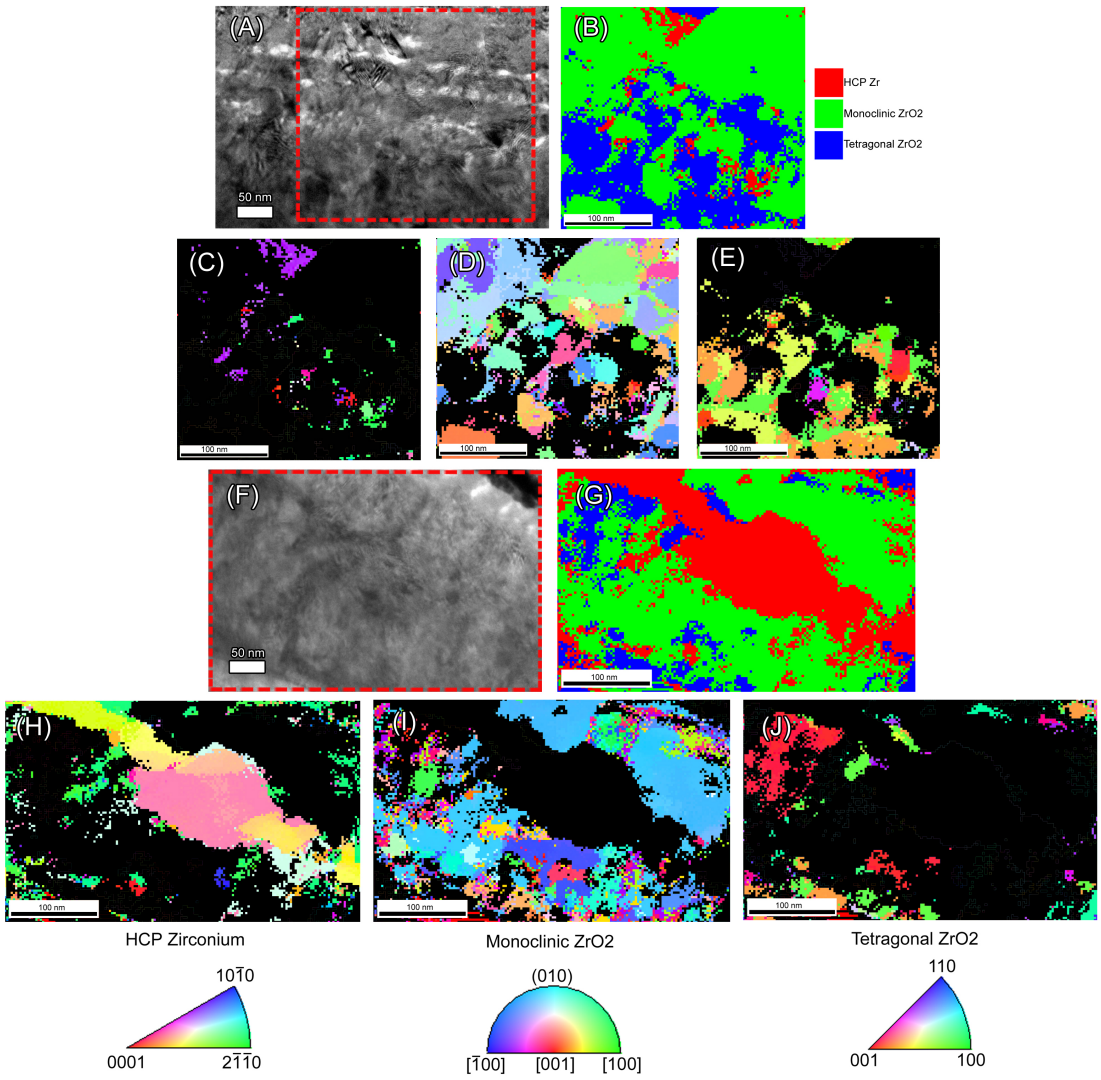

Figure 35: Cross sections from FIB lift outs oxidized *in-situ* at 800°C (A-E) and 650°C (F-J) and the corresponding phase and orientation maps for the bright field TEM images. (C) and (H) Orientation maps for HCP Zr. (D) and (I) Orientation maps for monoclinic ZrO_2. (E) and (J) Orientation maps for tetragonal ZrO_2. Figure is reproduced from Harlow et. al[119].

The vast majority of the oxide consisting of monoclinic ZrO_2 with small localized areas of tetragonal ZrO_2 corresponds well with previous studies done in bulk oxidized sample[42,44,45]. In addition, the phases and orientations that are identified in the cross sectioned sample also correspond well with those found in the autoclave-oxidized

samples. Figure 36 shows a phase and orientation maps for an autoclave-oxidized sample in a region far from the metal-oxide interface. When compared to the cross-sectioned in-situ sample in figure 35, it is easy to see the presence of similar oxide structure as well as orientations. In the case of the plan view sample shown in figure 33, it is thought that the higher amount of tetragonal ZrO_2 is the result of this being the initial oxide layer forming, which is expected based on past studies using XPS and synchrotron XRD[37,42]. As seen in figure 34, near the oxide metal interface, there is a higher incidence of tetragonal ZrO_2 as compared to far from the interface as is seen in figure 36. The use of phase mapping via precession electron diffraction to identify tetragonal and monoclinic ZrO_2 was recently shown by Garner et al. to be reliable, and showed minor amounts of tetragonal ZrO_2 within the oxide layer of a autoclave oxidized sample[45]. The presence of a minor amount of tetragonal ZrO_2 may be the result of the thin TEM foil not allowing for sufficient stress to accumulate, in turn stabilizing this phase. Platt et al, have showed this behavior in recent work via finite element modeling that among other factors, relaxation in the oxide promoted the transformation of tetragonal ZrO_2 to monoclinic ZrO_2[139]. We have seen a similar behavior when the phase maps between the plan view of the in-situ sample and the cross section of the in-situ sample are compared. The cross section sample is thinned in such a manner that the sample can relax, resulting in a lower fraction of the stress-stabilized tetragonal phase as compared to the plan view of the same sample.

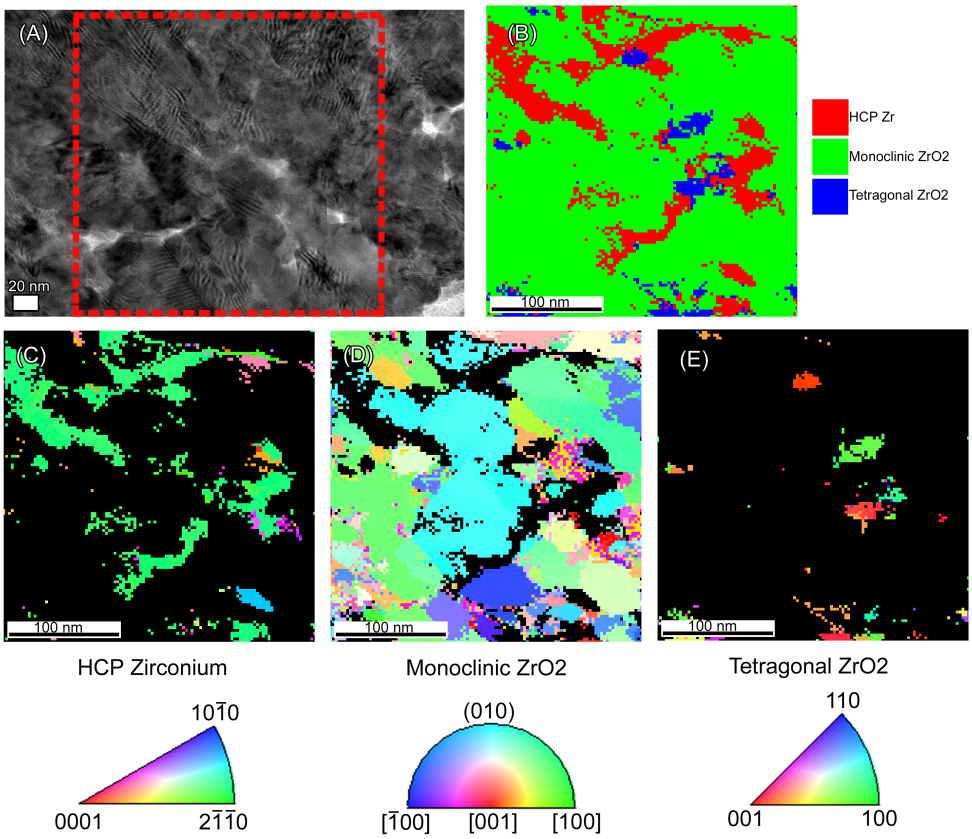

Figure 36: (A) Conventional TEM image of an autoclave oxidized sample far from the oxide metal interface showing the region over which precession diffraction was taken. (B) Phase map showing a majority phase of monoclinic ZrO_2. (C) Orientation map for HCP Zr. (D) Orientation map for monoclinic ZrO_2. (E) Orientation map for tetragonal ZrO_2. Figure is reproduced from Harlow et. al[119].

This stress stabilization of the tetragonal phase has also been shown by XRD and synchrotron studies, with the tetragonal phase fraction being reduced when relaxation occurs[124]. Other studies have shown that small amounts of tetragonal ZrO_2 will remain after preparation of a TEM foil[42,45], but it is difficult to determine the amount of stress required to stabilize this phase.

The partial oxidation that occurred in the sample oxidized at 650°C reveals a possible dependence of oxidation on crystallographic orientation, as expected based upon

previous work done on bulk alloys and thin film zirconium samples[18,31,81,140], and future work will focus on better elucidating these effects. Ploc, using an agglomeration of data from various authors, showed that when oxide thickness is shown versus Zr orientation certain directions show a preference for thicker oxides, however this work was focused on the epitaxial relationship of the oxide to the base metal[18]. Both Ploc and Glavicic revealed orientation relationships between the oxide and the base metal, and more recently, Garner et al found that oxidation rate may be partially controlled by oxide structure[18,31,45]. Additionally, the crystallographic texture of the initial oxide formed on the surface of the base metal can also be determined using the cross section technique presented above, which may offer insight into whether an oxide is protective or non-protective. At this point there appears to be a texture to oxide, as the orientations seen in figure 32 show, which is expected based on the work of Li et al. Gong et al. and Garner et. al. [36,45,81]. In particular, the monoclinic oxide appears to show a (010) type texture. Further work needs to be done to examine the texture in the oxide grown using the in-situ method and its effect on oxide growth, and a much larger sample size is needed for definitive conclusions.

While in-situ TEM provides a good method for studying initial oxide formation, there are some limitations to this technique. It is limited to early stage oxidation because of sample size, particularly sample thickness. In addition, when using in-situ TEM, the environment that can be used is limited by the TEM holder capabilities, such that pressures of only up to one atmosphere of pressure can be reached, and hot liquid environments are not currently viable, although experiments in high humidity environments are starting. Autoclave oxidized samples are much better for the study of long-term oxidation behavior and of the associated kinetics of oxidation. However, this

technique provides a good method for study of the first stages of the oxidation process because of its high spatial and temporal resolution.

3.9 Conclusions on Autoclave versus In-situ

Through the use of environmental TEM combined with precession diffraction techniques, it was shown that the bulk scale corrosion of Zry-4 in an autoclave can be successfully replicated on the nanoscale inside the TEM. It was seen that Zry-4 forms both monoclinic and tetragonal ZrO_2 structures that appear similar to the structures seen in autoclave samples. This structure compares well with the oxide structure seen in literature, and the initial phase also corresponds to the initial oxide layer seen on autoclave-corroded samples. Thus, in-situ TEM can replicate the corrosion behavior of this alloy and elucidate the effects of texture, grain, and grain boundary orientation on the corrosion performance of this alloy. Moreover, the environmental cell design used for this experiment offers great flexibility, and can be used to study a variety of materials under extreme environments at the TEM scale. This design allows for studies in oxidation of thin films, hydride formation, catalyst studies, and boundary effects on corrosion processes.

3.10 In-situ Oxidation of Pure Zirconium

Following the development of experimental parameters for Zircaloy-4 and the work showing that in-situ TEM is a viable method for oxidizing samples without having clear thin film effects changing the structure of the oxides formed, the next step was to observe the formation of oxide during the in-situ experiment. As was discussed briefly above, it had been found in the course of the other experiments that observing oxide formation in Zry-4 in-situ was not possible in a quantitative manner, and even a

qualitative evaluation was very difficult to conduct with certainty. As such, the best option for further observations of in-progress oxidation was to move a simpler system. Pure zirconium lacks the complicating secondary phase particles of Zry-4, and also was not cold worked, as was the case with the Zry-4 samples we were provided with. The lack of cold work means that there were many fewer dislocations within the samples, allowing for much better imaging of the sample with hopefully better contrast as a result of lacking diffraction from a high number of dislocations. One might ask why not simply anneal the Zry-4 to remove the cold work, and there are several reasons for this in our case. At Drexel we do not have a suitable vacuum furnace for annealing these samples without oxidizing them, we were provided with a very limited amount of pristine sample (a 1 inch by 1 inch corrosion coupon), and by annealing this sample it would no longer be a one to one comparison with the autoclaved sample as we would have changed the heat treating conditions. Thus, for all these reasons, it made sense to move to a pure zirconium if the samples could be acquired. Due to the prevalence of pure zirconium samples disintegrating during autoclave testing, these samples took much longer than expected to be acquired. Once the samples were acquired, oxidation conditions for the pure condition had to be found, and testing for the ability to observe oxidation progress began.

Pure zirconium is often used as a control sample when autoclave tests for corrosion behavior are conducted on various zirconium alloys[32,48,78,140,141]. However, these samples are commonly destroyed during long-term tests as a result of their high oxidation rate combined with the spalling of the oxide layer. These concerns are limited for our in-situ TEM experiments, with instead the concern being oxidizing the sample through thickness. As such, the expectation was that initially the same conditions would be used as with Zry-4, however a shorter time would be used to prevent through thickness

oxidation. Initial tests showed that this was indeed the case, and that times of 10 minutes at 300°C lead to through thickness oxidation. Since the objective of this set of experiments was to identify the possibility of observing oxide growth in-situ, this simply limited the total experiment time to less than 10 minutes. It was found that imaging conditions used for earlier Zry-4 conditions of bright field TEM with the third high contrast aperture were still the best conditions available (as expected), but the change in

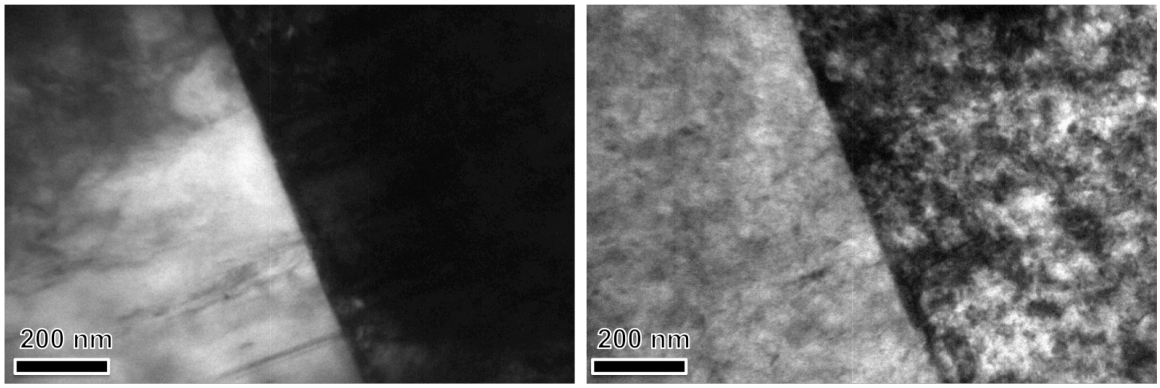

Figure 37: Before and after images showing the drastic change in appearance of a pure zirconium sample oxidized in-situ at 300 °C. Image on the left shows the pristine condition with a very clean microstructure while on the left after the experiment the formation of oxide grains has added to the contrast significantly.

sample material only slightly benefited the objective of observing oxide nucleation. During the experiment, there was little noticeable change, however if the images prior to oxidation and following oxidation are compared as in the figure below, drastic changes in the sample are easily visible. While these changes are easily visible before and after, how the occur during the experiment makes identification of oxidation initiation difficult. When the sample is being heated to temperature, some drift occurs, which can be compensated for by moving the sample stage. However, the windows in the gas cell system also flex when heating, and this changes the diffraction condition by a small

amount, making it very difficult to track certain features. In the above figure, this is an ideal case whereby a diffraction condition was achieved where there is a huge change in contrast between the two grains' diffracting conditions. During the video of this experiment, once sped up to 10x speed, it is clear that oxidation is not occurring until a temperature near 300°C is reached. Once this temperature is reached, the image almost immediately changes to look similar to the final image shown above, indicating rapid oxidation. An additional experiment was conducted at 150°C to attempt to slow down the oxidation process to a speed at which the initiation point could be observed, however after 10 minutes at temperature in at 50-50 oxygen argon gas mixture, precession diffraction as well as bright field TEM failed to show any significant signs of changes attributable to oxidation. At this point, work on gas environments for oxidation of pure zirconium was stopped, as there did not appear to be significant gains to be had as compared to previous experiments in Zry-4, and other imaging conditions such as HAADF and EFTEM were on hold pending the installation of the new JEOL 2100F microscope.

Instead, work focus shifted to developing high humidity environments as discussed previously. For oxidation studies, pure zirconium was an ideal candidate for proof of concept, as sample preparation was easier than Zry-4 and evidence of oxidation was much easier to see as compared to the dislocation heavy Zry-4. In addition, the lower oxidation resistance of pure zirconium provided benefits for observing oxidation. Initial tests were conducted at the same temperature of 300°C as previous oxidation experiments, but the gas environment was changed to a high humidity level to investigate the possibility of using high humidity environments to simulate more realistic corrosion behavior. As such, after the tests discussed previously using various salts to show the

presence of humidity within the sealed chip, the first tests were done with the expectation of no reaction until a high temperature was reached. This sample was heated to 300°C for 9 minutes, and then brought back to room temperature and cross sectioned to look at oxide thickness and structure. As shown in the figure 38, A and B, the sample clearly

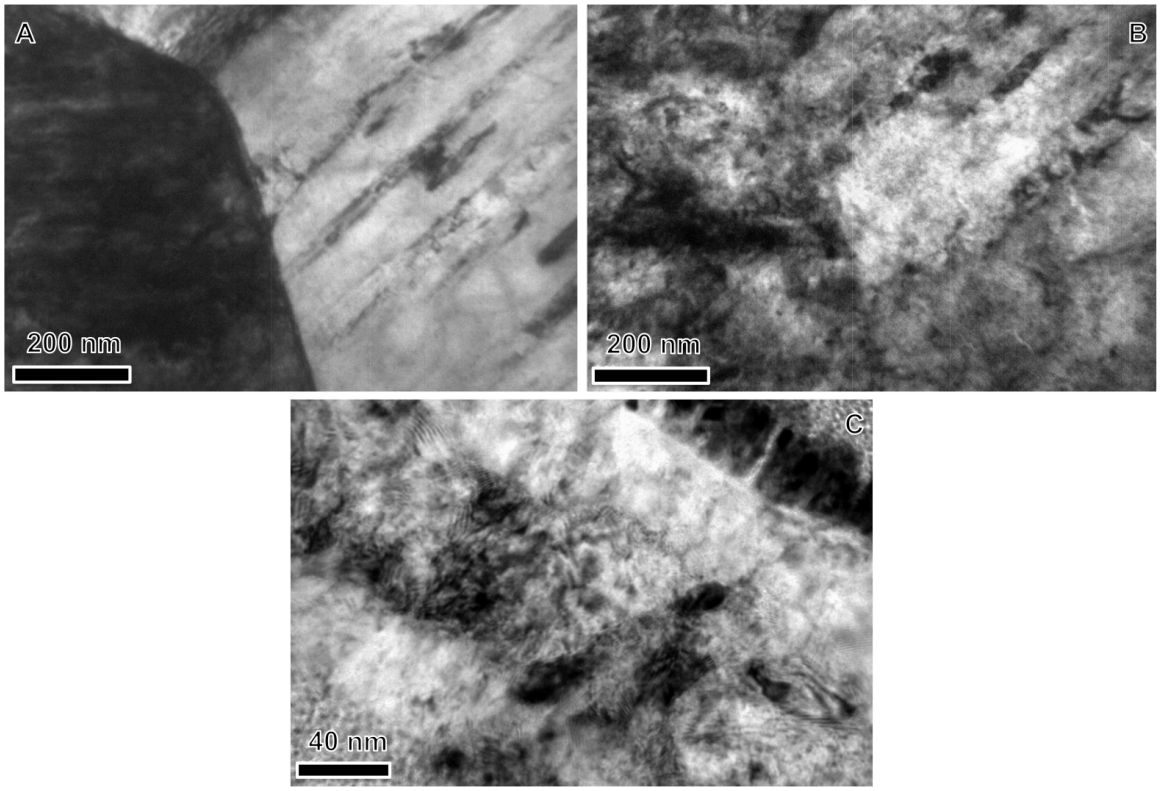

Figure 38: Oxidation experiment conducted on pure zirconium in a high humidity environment. A) Pristine sample condition showing a triple point of 3 grain boundaries meeting. B) Same area as A after 9 minutes at temperature showing clear oxidation. C) Cross section of the same sample with clear layers of oxide, then base metal, and oxide again.

oxidized under these condition, with the triple point present in A being almost completely obscured in B after the oxidation experiment. It was found that the sample had clearly oxidized with definitive layers within the sample when it was cross-sectioned as is shown in C, with the sample consisting of from top right to bottom left: a protective FIB deposited platinum layer, sputter coated platinum layer, oxide layer, base metal, bottom

oxide layer, and platinum/re-deposition layer. Unfortunately, this sample met an untimely demise prior to confirmation of these observations using precession diffraction, but based upon the images taken and the expected oxide structures, this sample clearly had a significant oxide layer. Following this experiment, this was repeated after improvements were made to the humidity inlet system for the holder. During this experiment, video was recorded during the initial time to raise the humidity level within the cell, as the previous experiment had shown some signs of changes, but these were not readily identifiable without video that could be sped up to make changes more obvious. It was found after the experiment that during the long period of time it took to reach a high level of humidity within the environmental cell, if the video is sped up to 10x, it appeared that some changes were taking place within the samples, and that these changes looked very similar to those seen in the videos of the more corrosion resistant Zry-4 in dry

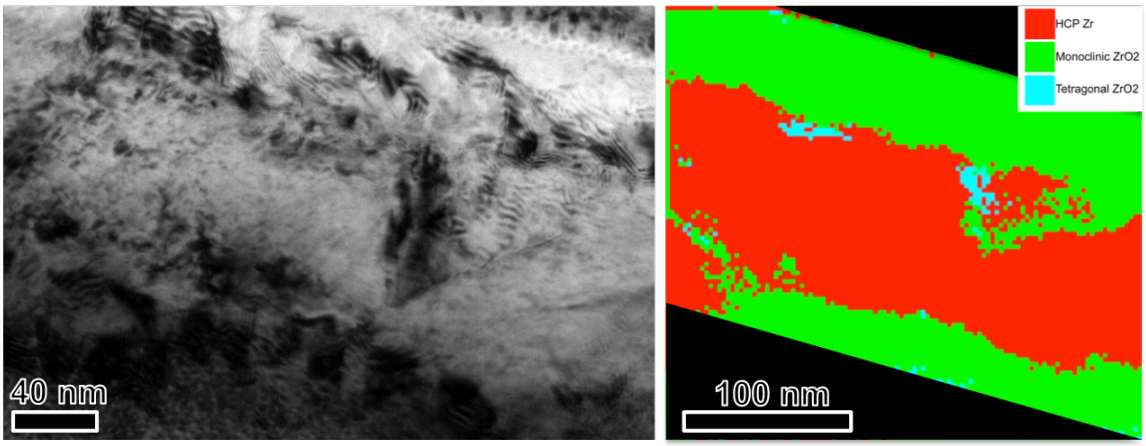

Figure 39: Image on left shows the cross-section of a pure zirconium sample oxidized in-situ under a high humidity environment for 5 minutes at 300°C and the area from which the precession diffraction map on right was taken. As can be clearly seen, the sample is oxidized with a majority of the oxide phase being monoclinic ZrO_2

gas at longer time steps. This sample was oxidized at 300°C for 5 minutes, and when cross sectioned it showed a small oxide layer of approximately 20 nm, with a significant amount of base metal remaining. Precession diffraction scans taken after the sample was cross-sectioned confirmed that the sample did have a significant oxide layer consisting of mostly monoclinic ZrO_2 approximately 20-40 nm thick depending on the region. The oxidation of the sample at room temperature in the highly humid environment is of interest, as these samples have shown to be stable in a dry gas environment for several minutes up to at least 150°C in other experiments. Understanding why oxidation occurs more rapidly in the highly humid environment could be crucial to understanding the overall oxidation mechanisms in zirconium-based alloys. While at this time we do not have enough information to draw solid conclusions regarding this behavior, it is the suspected that the driving force for this reaction may be the dissociation of the water molecules by the 200 keV electron beam, resulting in a monoatomic oxygen which would be able to rapidly diffuse into the zirconium matrix and start the oxidation process. This process should be easily checked in future experiments by making multiple samples and exposing them to the same conditions, but only imaging one sample with the humid environment present. If only the imaged sample shows changes, it can be known for certain that the electron beam is playing a role in oxidation, either through local sample heating or dissociation of the water molecules in the atmosphere.

In conclusion, in-situ oxidation of pure zirconium occurs more quickly than Zircaloy-4, which is expected based on many years of literature and forms the oxide phases and structures similar to those in autoclaved samples in both dry gas and high humidity environments. However, from our experiments to this point, the increase in rate cannot be quantified, as oxidation is not truly readily visible in plan view, and these

samples were lost during the cross sectioning process. In our experiments, we have shown that while the cleaner microstructure of the pure zirconium as compared to the Zry-4 helps to improve imaging in the before and after cases, but unfortunately it does not shed additional light on oxidation processes while they are occurring in a dry gas environment. That said; using this material we have shown that oxidation experiments can be successfully conducted using high humidity levels which will better simulate elevated temperature water/steam environments. In addition, these environments show the potential for room temperature oxidation experiments in this system in future work, which may allow for the use of different TEM techniques such as selected area diffraction or dark field imaging as a result of the limited drift which occurs because of the lack of thermal gradients resulting from heating. Going forward, after final development and calibration of the humid air system, revisiting this material using these techniques may provide significant information into oxide nucleation points and initial oxide structures.

3.11 The Effects of Secondary Phase Particles on Oxidation Behavior

As has been discussed at length earlier, it is known that the corrosion resistance of zirconium-based alloys can be significantly altered using minor amounts of alloying elements. There have been great advances in oxidation resistance with alloys such as ZIRLO and M5, however the exact effect of alloying elements on oxidation response is not well understood. This is well illustrated by the continuing research in this field, including recent articles such as the work of Chollet et. al using synchrotron x-ray diffraction to investigate to try and look at the effect of secondary phase particles (SPPs) on oxidation in irradiated Zircaloy-2 [22]. Zircaloy-2 was one of the first zirconium-based alloys for nuclear service[3], and there is still not a good understanding of how SPPs affect

corrosion performance. As such, I was encouraged to shift away from humidity development and try to investigate SPP effects on oxidation in Zircaloy-4 by my committee.

Since oxidation conditions and the suitability of in-situ TEM were well established, the remaining challenge to study SPP effects was to find imaging conditions and/or analytical methods to provide information about the oxidation process. A JEOL 2100F with a Gatan image filter (GIF) was installed and commissioned just prior to the decision to focus on SPP effects, so this opened up the options of HAADF, EFTEM, and EELS for different techniques than what had previously been used. In addition, the final upgrade to the environmental cell was an adaption to a "butterfly" type holder lid that allowed for proper take off angle so the holder was EDS compatible. With these advancements in the available equipment and techniques, there was a chance that some information about SPP effects could be gained. Since the objective was to look at simply SPP effects, the first question to be answered was whether or not samples will SPPs could be prepared using the elderly FIB at Drexel. Samples were first prepared using conventional lift out techniques to identify if site specific preparation was needed as the lack of a backscatter electron detector in the FIB at Drexel limits phase contrast from particles as small as the average SPP in Zircaloy-4. It was found that samples could be effectively prepared without specific targeting; although it was also found there are some caveats to this. As shown in the image below, the average size of the SPP in the Zry-4 being prepared was between 50-200 nanometer range.

Figure 40: TEM image showing three secondary phase particles in the range of 50-200 nm.

This meant that the sample had to be extremely thin for good imaging of the SPPs, which as will be discussed further, comes into conflict with the added thickness of the windows in the environmental cell.

After it was found samples could be prepared with SPPs, progress moved on to addressing the in-situ experiments. Precession diffraction was not used to characterize the samples, as the objective was to look at SPP effects, and without knowing the expected crystal structures precession diffraction cannot be used to provide phase information. The experimental plan was to monitor the sample during the experiment using STEM techniques, either ADF and HAADF or brightfield and HAADF. EELS, EDS and EFTEM, which take several minutes to acquire, would be used before and after the experiment. By running the samples in this manner, the information regarding the best technique could be quickly found, and each sample would have significant

characterization done. Samples were oxidized at the previously determined conditions of 300°C in a 50-50 oxygen-argon dry gas mixture.

Initial characterization was attempted using EFTEM on the JEOL 2100 FEG. After the verification of the presence of SPPs in a region that could be easily imaged using bright field TEM, EFTEM was used to try and identify the SPPs. The maps, which are shown in figure 41, were made over the region that showed a definitive SPP. These maps were made to show iron, chromium, and tin.

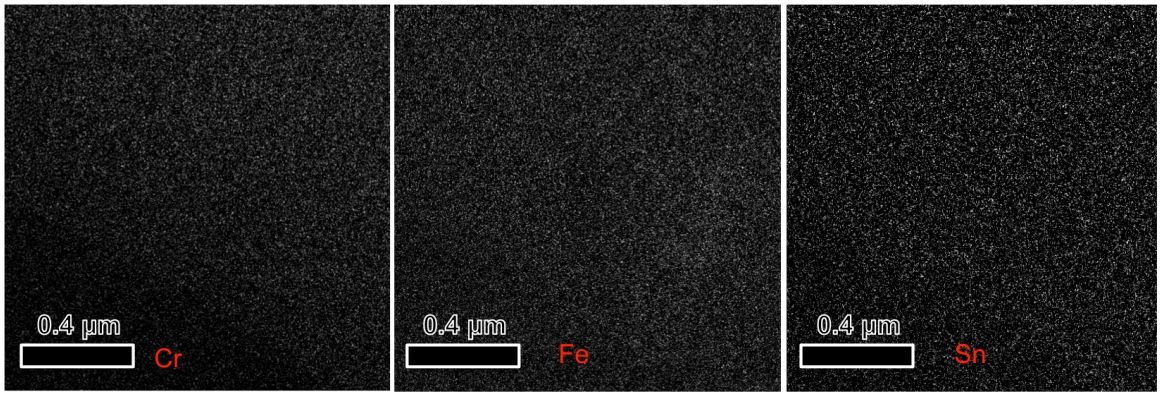

Figure 41: EFTEM maps for Cr, Fe, and Sn in a region known to contain a SPP showing only noise.

As can easily be seen, no definitive information was recorded, only noise. This was unexpected, as the SPP was easily visible, and the answer was found when a thickness map of the region was conducted. For reliable analytical information to be recorded using electron energy loss, the sample thickness needs to be less than 1.2 mean free paths (mfp)[142]. This sample, when measured via the log-ratio method[143] utilizing low-loss EELS, measured at 0.7 up to 1.25 mfp, so the sample would excellent... normally. However, because we are conducing this experiment in an environmental cell, the beam also passes through the SiN windows, which add an additional 1.25 mfp to the sample.

Thus, total thickness is equal to 1.95-2.5 mfp, rendering quantitative EELS and EFTEM impossible, even for what would normally be a stellar example sample. As such, the experiment proceeded using HAADF and annular dark field (ADF) to monitor the sample during the experiment. Nothing substantial was recorded during the experiment as far as contrast for the growing oxide, and the experiment was repeated with a new sample using HAADF and bright field STEM at a higher magnification to best show the sample behavior. It was found that while a SPP could be isolated for examination during the in-situ experiment, almost immediately upon reaching temperature there was a massive change in the sample resulting in a loss of contrast and focus in STEM mode. The images shown below were taken before and after the oxidation experiment to illustrate the massive change within the sample that required reduction of magnification.

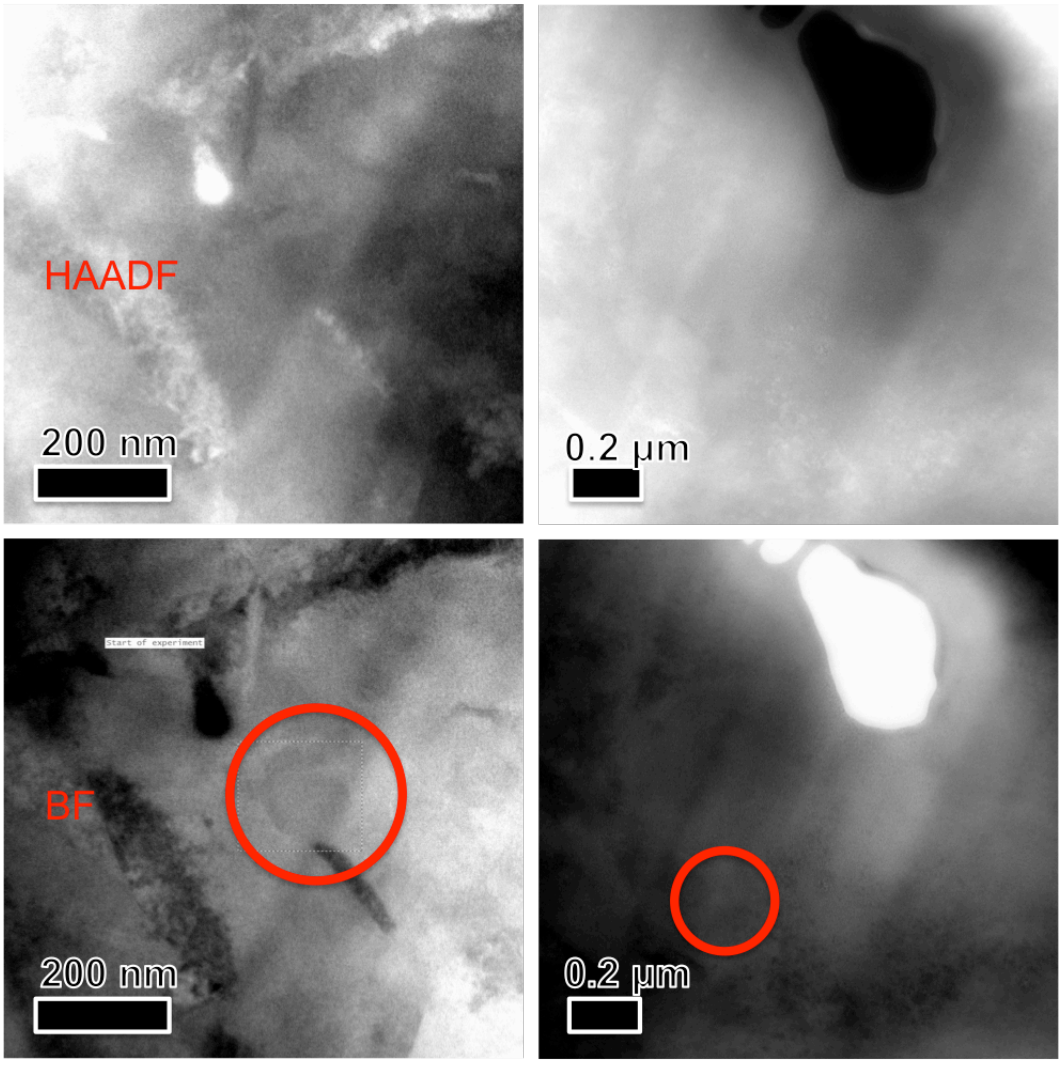

Figure 42: HAADF (top) and Bright field STEM (bottom) images before oxidation experiment on the left, and after on the right.

The interesting part of this massive change was the fact there was little occurring during the heating of the sample, but almost instantaneously upon reaching 300°C this change occurred. Sample thickness was found to have increased greatly, by about 0.65 mfp as measured using low loss EELS, which explains the large change in contrast and focus. The best explanation for this rapid change is most likely sample thickness. In order to be able to easily distinguish the SPPs in these samples, the sample needs to be extremely thin. By being very thin, this means there is a very large surface area of oxygen to

interact and little distance it needs to diffuse for the oxidation reaction to occur. Thus, once a critical temperature is reached, the sample almost instantaneously transforms into oxide. Prior samples most likely did not show this behavior because sample previously used for in-situ oxidation experiments were prepared with the philosophy as thin as necessary, and thick as possible, so as to increase the amount of time prior to the sample be oxidized through thickness.

In the end, little information regarding the effect of SPPs on oxidation behavior was gained through these experiments, however the use of EFTEM, EELS, HAADF, ADF, and EDS were explored for characterization during in-situ oxidation. It was found that all of these techniques are very limited in usefulness, and that this is almost entirely the result of overall thickness the electron beam passes through. While a very good sample can be prepared that would normally be excellent for these techniques, once the additional thickness provided by the SiN windows of the environmental cell are added, the overall thickness becomes too large for analytical techniques because of multiple scattering, and changes to the sample are too small relative to the overall contrast in techniques such as HAADF.

3.12 Effect of Alloying Elements on Initial Oxidation Rate

Following the failure of in-situ characterization of SPP effects in Zircaloy-4, it was decided to attempt to compare the initial oxidation rates of Zry-4 and pure Zirconium using low loss EELS to assess the effect of alloying elements on overall initial oxidation rates. Doing this type of experiment would allow for possible kinetics of the oxidation process via measured thickness versus time as well as direct comparison of the rates of first stage oxidation. This would indirectly provide information regarding the effect of SPPs

on initial oxidation behavior. In addition, in other materials systems it may be possible to establish the effect of precipitates on oxidation rate if the precipitates are large enough. Finally, as mentioned several times before, there is little information regarding the first stages of corrosion behavior in zirconium-based alloys, as almost all work has been conducted either via autoclave or in-pile testing. For a direct comparison, multiple samples of each material were prepared, and oxidized at the same time in-situ in the TEM with multiple heating steps. Thickness measurements were taken between heating steps to identify sample thickness, since the there were multiple samples to measure, measurements could not be conducted with heating occurring as sample thickness would be changing over time.

For this experiment, 2 samples from Zircaloy-4 were prepared along with 3 samples from pure zirconium. In each case, at least one sample was left somewhat thick for normal TEM imaging, so that if the thinner samples were oxidized through thickness the data would show this instead of appearing as a plateau of protective behavior. Since this would be the first experiment of this type, and it was expected that the oxidation rate of pure zirconium would be much quicker than Zry-4, the initial oxidation parameters were to be lowered to 150°C to make sure multiple thickness measurements could be made prior to through thickness oxidation.

In order to fully characterize this experiment, thickness maps were first made at atmospheric pressure in a room air environment, then at low vacuum (~7 torr), and finally at atmospheric pressure in a 50-50 oxygen-argon environment. By doing this, it allows us to characterize the effect of gas environment on thickness measurements. It was found that the average change in measured thickness was from 0.3 mfp to 0.18 mfp when going from a atmosphere of gas to a low vacuum (7 torr) condition. Between the two

atmospheric conditions, the average change in measured thickness was 0.1 mfp, with the 50-50 oxygen-argon mixture giving a thinner measurement. The results of this test indicate that gas pressure does have an effect on the thickness as measured using the log-ratio method, so it is of the utmost importance that for reliable data, all thickness measurements be recorded using the same environment.

After characterizing the effect of various gas environments on thickness measurements, the samples were heated to 150°C for 80 seconds at 5°C per second, and cooled back to room temperature at the same rate. Thickness maps were then taken on each of the samples. It was found that there was no significant change in the thickness, with changes less than 0.1 mfp for all samples. At this point, in the interest of time (and because the holder started to leak), the temperature for oxidation was increased to 300°C to increase the corrosion rate. The first time step done was 60 seconds at temperature, followed by thickness mapping, then another 90 seconds at 300°C for a total time at temperature of 150 seconds.

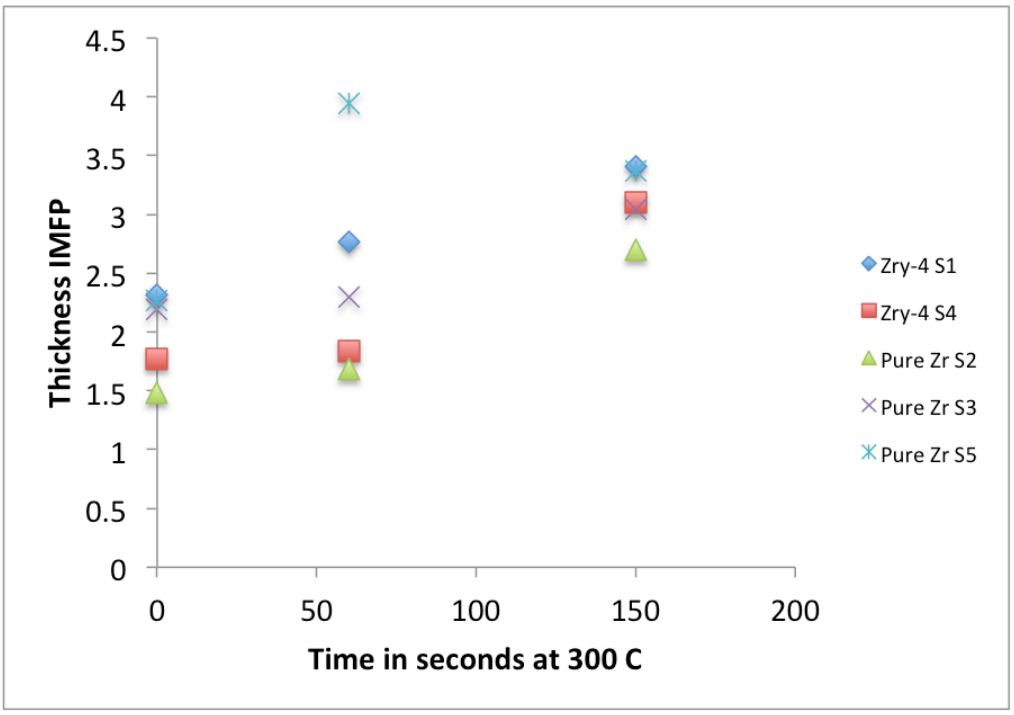

Figure 43: Thickness in inelastic mean free paths versus time at 300°C for pure zirconium and Zircaloy-4.

As shown in the graph above, thickness rapidly started to increase, however there is some scatter within the data. While there is the need for further experiments to reduce scatter in the plot, it appears that this method will provide good insight into the initial corrosion behavior, with some samples showing what appears to be a cubic type corrosion response. What is especially interesting in the data so far is there does not appear to be a significant difference in initial behavior between the pure zirconium and the Zry-4. If further data confirms this trend, evidence will point toward the corrosion behavior being controlled by alloying elements and how they stabilize or destabilize the tetragonal ZrO_2 phase as opposed to having a direct effect on initial behavior by forming a protective oxide layer based on alloying element composition.

In conclusion, studying the effect of SPPs in Zircaloy-4 proved to be a very challenging problem, however after much work a path forward has been created that offers the opportunity for great advancement in knowledge of the first stages of oxidation. While many analytical techniques cannot be used because of thickness effects caused by the two window environmental cell, other techniques have shown the potential for good information. By using low-loss EELS to measure thickness using the log-ratio method, information can be gained at small time steps regarding oxide thickness, and can be repeated to create a oxide thickness curve for oxidation rate. Moving forward, this technique will allow for the study of several different effects on oxidation. In larger grained materials where there is a single grain boundary in the field of view being measured, the effect of orientation and possibly the grain boundary on initial behavior can be studied. For other materials with larger precipitates, it is possible that the oxidation rates of regions near and far from precipitates can be investigated to look for evidence of protective behavior. In the larger sense, this also allows for the collection of new data in the zirconium field, as small FIB samples can be prepared from irradiated materials, placed on a chip with a non-irradiated sample, and the corrosion response as an effect of real neutron damage can be recorded.

4 Stress Stabilization of Tetragonal ZrO_2

During the course of the in-situ corrosion experiments, it was found that on sometimes there were very different results from Nanomegas scans taken in plan view of the samples following oxidation, and scans taken from similar areas that had been cross-sectioned. This was a very confusing problem to encounter at first, until I realized that the samples that showed good agreement in the Nanomegas data between the plan view

and cross-section were those that had been oxidized through thickness. At this point, there were two possible causes, the first being that by oxidizing the sample through thickness, we removed the layered structure from the sample, meaning that no longer would the beam be interacting with two layers of oxide and the remaining base metal, but with only the remaining oxide. The second option is that by oxidizing the samples through thickness, this allowed for relaxation of the stress within the oxide, which based on literature, means that the tetragonal ZrO_2 phase will no longer be stable. If this is indeed the case, it calls into question many years of data trying to explain and quantify the percentage of tetragonal ZrO_2 in the oxide layer using TEM, as through sample preparation this could significantly change the percent of tetragonal ZrO_2 if the sample relaxes.

4.1 Background

Zirconium-based alloys have long been used for fuel rod cladding material and, as a result, extensive research into the corrosion behavior of these alloys has been previously conducted[3,17,20,21]. One long-standing debate has been the quantification of the oxide phases formed during corrosion; studies have found the presence of two distinct oxide phases: a tetragonal phase and a monoclinic phase. One particular question revolves around the role of tetragonal phase of the oxide and how the stability and protectiveness of this phase relates to the cyclic oxidation behavior of zirconium alloys. It is well known that over long-term tests, zirconium alloy samples experience oxide cracking, which may be detrimental to oxidation performance[34,54,144]. The cyclic oxidation behavior seen in these long-term tests has also been attributed to the formation, relaxation, and reformation of the tetragonal oxide phase[41,53–55].

These phases have been characterized using a wide variety of characterization techniques, including x-ray diffraction (XRD)[43,46,47], microbeam synchrotron diffraction[22,41–43], Raman spectroscopy[145], and transmission electron microscopy (TEM)[19,32,44,45,119], and studied with a variety of theoretical methods[55,139]. The relationship between the distribution of each oxide phase in the oxidation of zirconium and its alloys has been a long-standing question in the field, especially since the tetragonal phase of ZrO_2 is not stable at room temperature except under high stress[52]. Several authors have postulated that an oxide phase may account for the cyclic oxidation behavior seen in long-term oxidation experiments, as the stabilization/destabilization of the oxide phases could account for changes in oxidation behavior[17]. Several in-situ x-ray photoelectric spectroscopy (XPS) and synchrotron XRD studies have shown that tetragonal ZrO_2 is the initial oxide layer that forms [37,42]. However, it has also been shown that the tetragonal phase fraction is reduced when relaxation and transformation to monoclinic occurs[124]. This fits well with the theory that the tetragonal phase acts as the protective phase; the reduction of tetragonal phase due to relaxation correlates well with the abrupt increases in corrosion rate seen in long-term studies. Thus, much effort has been devoted to studying this problem and attempting to draw conclusions regarding the effect of the oxide phases on corrosion behavior.

The appearance of the tetragonal phase in the oxide formed on zirconium during oxidation has long been attributed to the stress present in the oxide. When considering how good a protective passive oxide layer is on a metal it is common to use the Pillings-Bedworth ratio, which has been calculated to be 1.56 for this oxide/metal system[145]. This implies that this coating has the potential to be protective, but it also implies that there will be a high compressive stress in the oxide film. Recently, studies by Platt et al have

looked at the stress stabilization of the tetragonal phase via finite element modeling and showed that the transformation from tetragonal ZrO_2 to monoclinic ZrO_2 could indeed be the result of relaxation of the oxide[139]. Previously, Garner et al.[45] and Harlow et al.[119] showed that using precession electron diffraction is a reliable method for identifying tetragonal and monoclinic ZrO_2 phases. In this work, we describe a systematic study of the thickness dependence of tetragonal phase fraction in ZrO_2 using TEM and precession electron diffraction, and find that the stress stabilization of the tetragonal phase is confirmed using this methodology. Our findings also provide a foundation for the study of how TEM sample thickness is likely to affect the amount of tetragonal phases observed within an oxidized sample via precession electron diffraction and electron energy loss spectroscopy. Ideally during this study, precession electron diffraction was also going to be used to quantify the amount of strain in the base metal immediately below the oxide-metal interface in order to provide better insight into how much stress is necessary to stabilize the tetragonal phase of ZrO_2, however, as will be discussed later, the challenges presented by sample thickness prevented this portion of the study.

4.2 FIB preparation

In order to test the theory that the sample relaxes and reduces the amount of tetragonal ZrO_2 present changes, a method of sample preparation was needed to control sample thickness. I concluded that the easiest approach to address this problem was to create a FIB sample that had multiple thicknesses within it, as this also eliminates the concern the sample being from a different area changing the composition. As such, the samples prepared for these experiments were prepared from via standard FIB techniques on 30 um-long samples, with the lift-out being taken top down into the oxidized pure

zirconium material, such that when viewed from the side there was a layered structure of platinum, oxide, metal. Each sample was thinned such that there were 5, 5 micron wide windows, with thickness varying from ~300 nm to as thin as possible (~30 nm), with the remaining 5 microns near the edge of the sample being sacrificed to attach the sample to the grid. Multiple samples were constructed in this manner to ensure any results were not from an artifact from sample preparation.

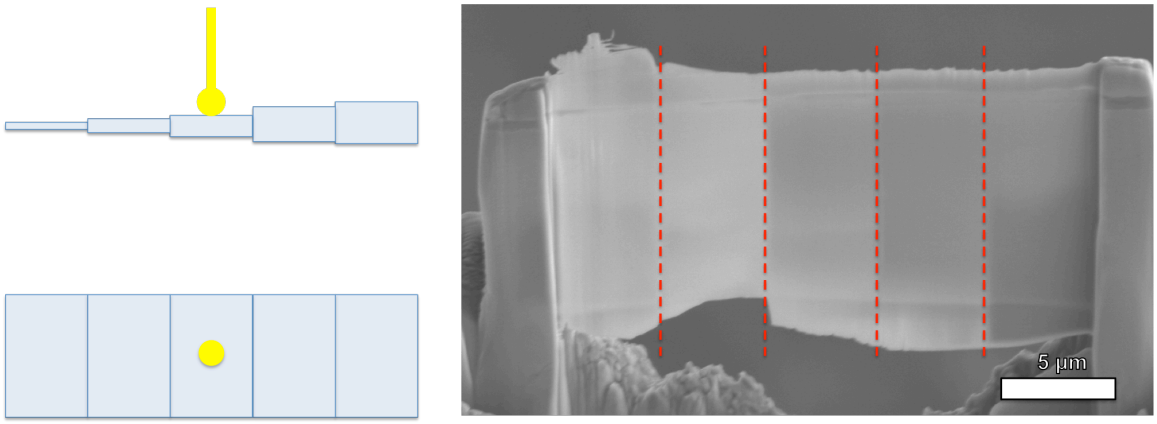

Figure 44: Schematic on the left illustrates the sample geometry used for stress stabilization studies, with the image on the left showing a sample prepared for analysis.

4.3 Precession Diffraction Conditions

In order to determine the phases present, precession diffraction was used in the same way it was used for all the preceding experiments. Each 5 um window in the sample was characterized by multiple scans at 30 kX covering the entire field of view, with a spot size of 15 nm and a step size of 2 nm by 2 nm when using the LaB6 JEOL 2100. All scans were taken to include the oxide-metal interface, as this region should have the highest occurrence of tetragonal ZrO_2. It was found that reliable data was only generated over two thinnest windows, with the reliability of the data being too low to be trustworthy in the 3 additional thicker regions once indexed, with the traditional indicator in my data being an unreasonably large percentage of the tetragonal ZrO_2 phase, which is

easily visually distinguished. For the two regions that showed reliable data in each sample, in all samples it was seen that in the thinnest window, the samples would show exclusively the presence of monoclinic ZrO_2 and the base metal HCP zirconium. In the thicker of the two windows, the data consistently shows a small concentration of tetragonal ZrO_2, especially at the metal-oxide interface, and within the bulk of the oxide, typically near features such as crack tips. These results seem to imply that there are definitely thickness effects on the percentage of tetragonal ZrO_2 present in the sample, and as such, sample preparation will be an important factor in determining the presence or absence of tetragonal ZrO_2. Based on these results, further work was done to try and quantify the level of strain present in the samples near the oxide-metal interface using Topspin strain analysis in the JEOL 2100 FEG. In addition, since the data generated using precession diffraction is prone to matching errors in this material system, electron energy loss spectroscopy (EELS) was used to both attempt to confirm the phase information generated, and to construct thickness maps for the samples so that the exact thickness of a given region was known.

4.4 Electron Energy Loss Spectroscopy

In order to determine the phases present in the samples, the oxygen edge in EELS was used. This is because there is a small change in the oxygen edge resulting from the different bonding in tetragonal ZrO_2 and monoclinic ZrO_2. The challenge with doing this type of analysis on these samples is the possible unreliability of data, as once samples begin to exceed a certain thickness threshold; it is no longer possible to deconvolute the information needed. In order to try this information, EELS scans were taken over each of the two thinnest regions of the samples covering a relatively large area of several

microns. Unfortunately, while this information did prove the already known presence of oxygen, the samples proved to be too thick for successful analysis to look at valence information from the spectrum. There was excess noise within the data, which prevented definitive conclusions as to the valence states of the oxygen.

However, these problems were not relevant for the use of EELS to measure the overall thickness of the sample in various regions. As such, the exact thickness of each step could be determined and related to the normalized percentage of tetragonal and monoclinic phase present in the precession diffraction scan for that step. Percentages were normalized so as to account for differences in the exact position of the oxide-metal interface within each scan regions. It was found that as sample thickness decreased, so did the fraction of tetragonal phase present in an almost linear manner as seen in the figure below illustrating the normalized percent tetragonal phase ZrO_2 versus sample thickness.

4.5 TOPSPIN strain analysis

Since it is thought that the stabilization of tetragonal phase is related to the stress present in the oxide, one of the best ways to determine how the oxide is affected by the change in sample thickness is to map the strain present within the sample. There are two major methods for doing this, the first being geometric phase analysis. In this technique, images are taken on zone axis at high resolution in an unstrained reference area, then in a corresponding area that is expected to have strain and compared to calculate the strain based on the shift in atomic positions. However, for this technique to work, the samples have to be able to be imaged at high resolution. Here we encounter the same problem with the EELS mapping for phase, that the samples are too thick to support good high-

resolution imaging, especially in the sample areas that appear to still have tetragonal phase in the precession diffraction phase mapping. The alternative method is to use an additional module for the precession diffraction system called TOPSPIN. This system works similarly to the idea behind geometric phase analysis, except that instead of using high-resolution TEM images, the system calculates strain based on a shift in diffraction spot positions. This technique is limited for the task at hand by several factors. The first is the need for the grain to be analyzed to be on zone axis, and in addition the grain must have both strained and unstrained regions. Finally, because of these first two factors, this means that this technique is only applicable to a single grain, and cannot be used over multiple grains. This in particular presents a problem since the oxide grain size is very small, so a reasonably sized scan would cover multiple grains, meaning the stress within the oxide cannot be effectively determined. This is in addition to the problem of finding an unstrained reference region within these small grains as well. Instead, the easier approach was to try and map the strain present in the underlying base metal, as the grain size of the zirconium was much larger than the oxide grain size. By conducting this same analysis over several samples, it should limit the chance of seeing effects due to conducting this analysis on a specific orientation.

Initial analysis was done near the boundary between the two steps so that the strain differences within the same image field of view could be quantified. For each area, the scan area was chosen such that the scanned area covered mostly base metal, but included a small amount of the oxide to ensure the information at the oxide-base metal interface was captured. Thus, when analysis was conducted, the proper area was selected as best as possible to only include the area for which there was a single grain. For comparison, the analysis was run over the entire scan area as well to see how the change

in orientation affected the strain mapping. It was expected that due to the orientation relationship between the oxide and base metal, the change in crystal orientation would cause the program to index the area with the oxide to show high strain, but not show a significant deviation that could easily be labeled. In practice, this showed to be the case, with the entire area indexing, but showing a very high strain region in both the area known to consist of the oxide and near the oxide metal interface. When the analysis between the full and area selected scans were compared, it was found that the refined scans showed lower overall strain values, but that the values were reversed from what was expected as shown in the figure below illustrating the results of the refined scans. That is to say the thinner region of the sample, which should have more opportunity to relax, showed a higher strain level than the thicker region of the sample. This implies that this technique is most likely needs further refinement to be used for this analysis in this material system.

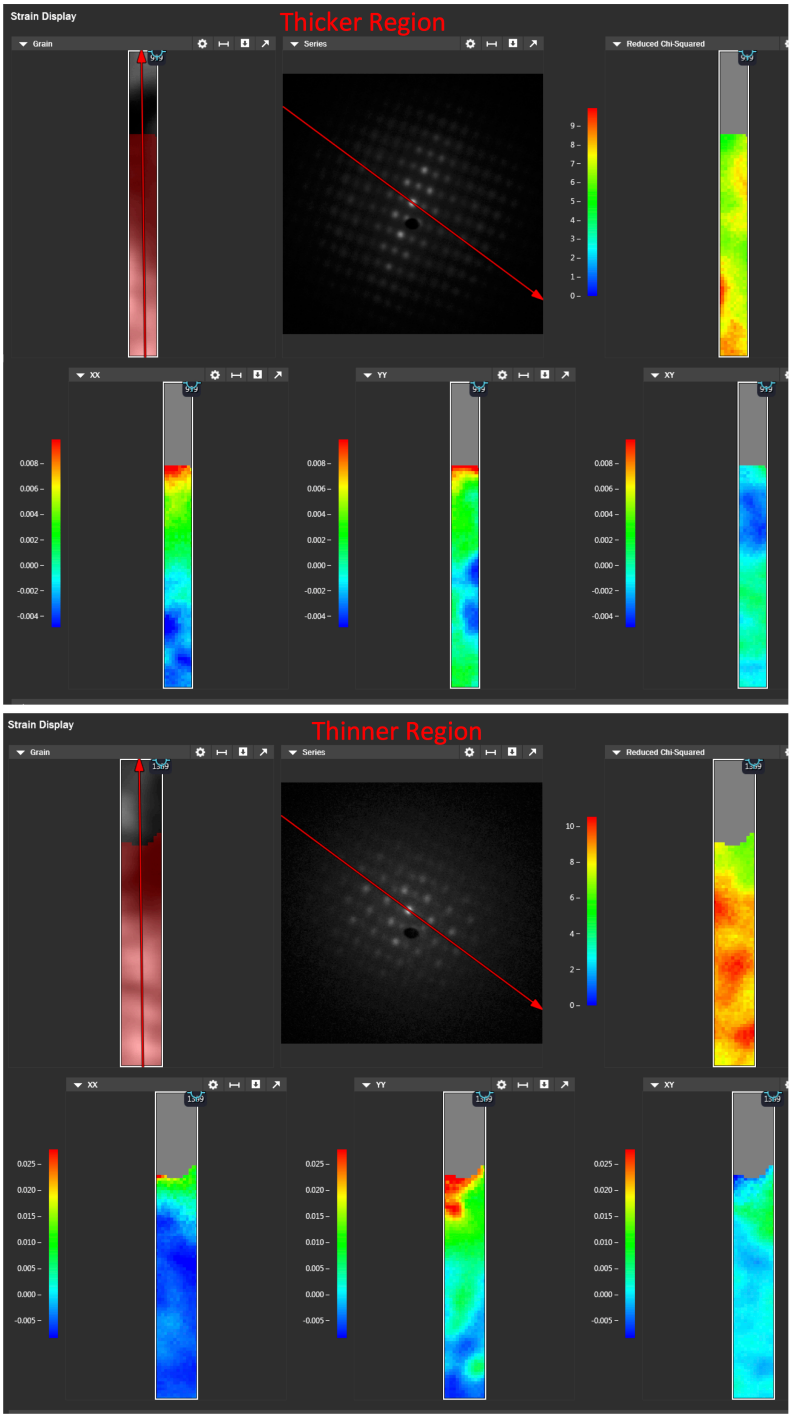

Figure 45:TopSpin Data set showing the unexpected result of higher strain in the thinner region with less tetragonal phase versus the thicker region with more tetragonal phase

One major reason that it is possible that the thinner region of the sample is showing higher strain than the thicker region is bending of the sample. As metal FIB samples

become very thin, often the samples will start to bow. In a system such as this, which uses diffraction information to generate strain information, the corresponding shift in diffraction pattern resulting from the bending of the sample acting to shift the diffraction pattern can account for a high strain value in a region where low to no strain might be expect.

To further address the use of TOPSPIN in this system and confirm this was sample related, another further samples were tried for analysis. Both of these samples were much thinner than the previous sample, approaching a 30 nm thickness. It was observed that in this case, the sample exhibited a large number of microrotations within the base metal in the thinnest region, precluding the use of TOPSPIN for the reasons discussed above with regard to the necessity of the sample remaining on zone-axis for the entirety of the scan. However, the information that it is possible to gain using TOPSPIN may prove to be a very valuable link between modeling efforts in the stability of tetragonal ZrO_2 and TEM studies, and further collaboration with the developers of the TOPSPIN system is underway to try and find a solution to the issues outlined above.

4.6 Precession Electron Diffraction Results and Discussion

In the thinnest window of all samples, PED measured the presence of exclusively monoclinic ZrO_2 and the base metal HCP zirconium.

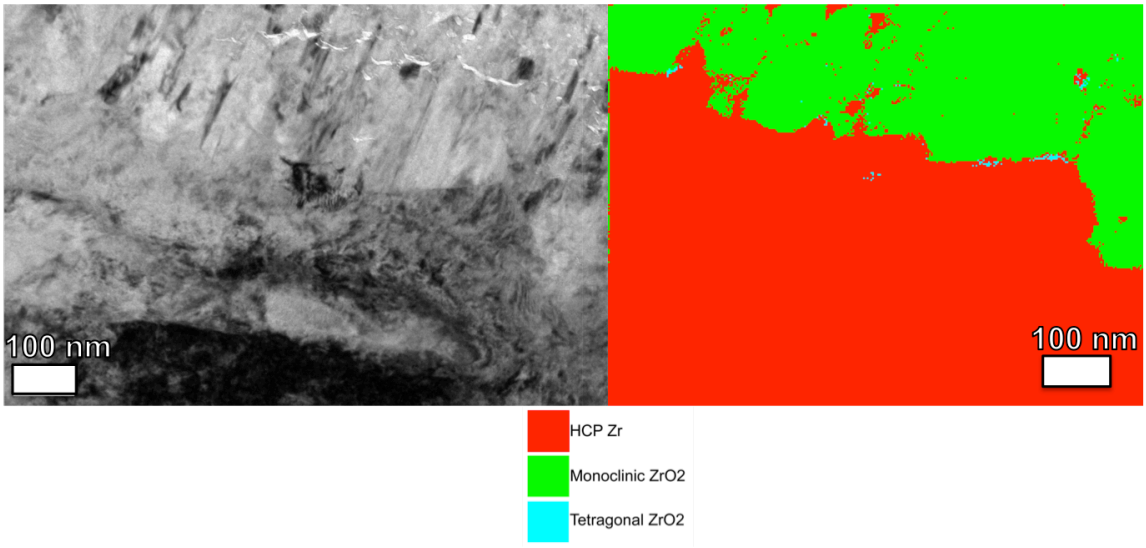

Figure 46: TEM image on left showing the region from which the precession diffraction scan on right, illustrating the absence of tetragonal phase in the thinnest sample region. EELS thickness map in this window provides a relative thickness of 0.59 imfp.

As can be seen in figure 46, even in regions where the presence of the tetragonal oxide phase is expected, such as the oxide-metal interface, easily visible in figure 46 as the intersection of the green monoclinic phase and the red HCP zirconium phase, precession diffraction shows almost no presence of the tetragonal phase.

Moving to thicker windows, the data consistently shows small concentrations of tetragonal ZrO_2, especially at the expected location of the metal-oxide interface, and within the bulk of the oxide, typically near features like cracks.

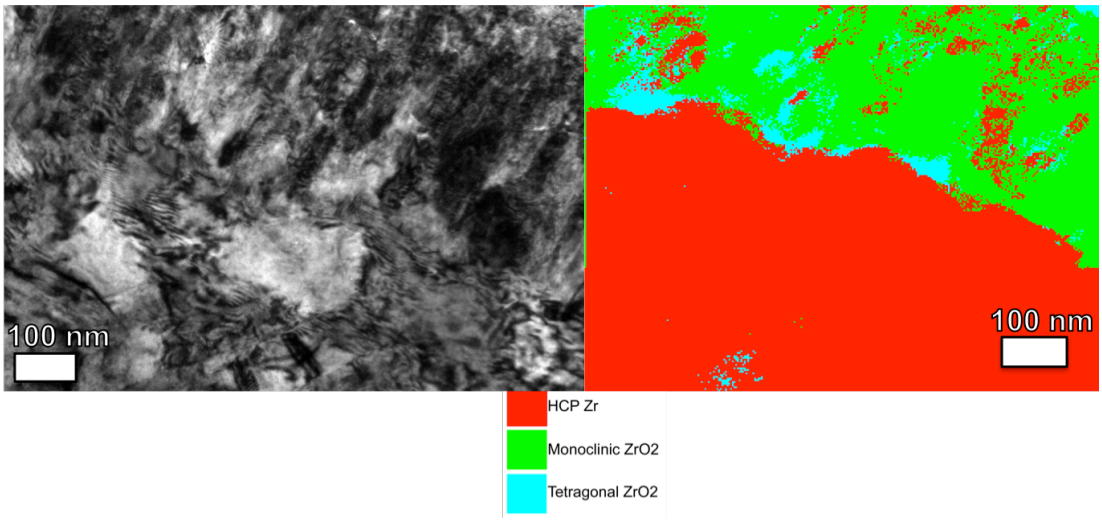

Figure 47: TEM image on left showing the area of the precession diffraction scan on right. Higher incidence of tetragonal phase is present in this sample area, especially at the oxide-metal interface. When measured using EELS, this windows approximate thickness was found to be 0.9 imfp.

These results imply that there are clear thickness effects on the percentage of tetragonal ZrO_2 present in the sample, and as such, sample preparation will be an important factor in determining the presence or absence of tetragonal ZrO_2. Figure 47 shows a thicker sample region as compared to figure 44, with a much higher occurrence of the tetragonal phase. When PED is combined with EELS to determine the relationship between the percent tetragonal ZrO_2 in the oxide layer and the relative sample thickness, it is clear that tetragonal ZrO_2 percent increases as thickness increases. At some value, a plateau would be expected, giving an accurate representation of the percent tetragonal in the bulk material, however with precession diffraction, the sample thickness exceeds the thickness allowable for reliable data prior seeing a plateau in the data.

As can be seen in figure 48, while there is significant scatter in the percentage of tetragonal phase recorded, the overall percentage of tetragonal phase generally increases as sample thickness increases.

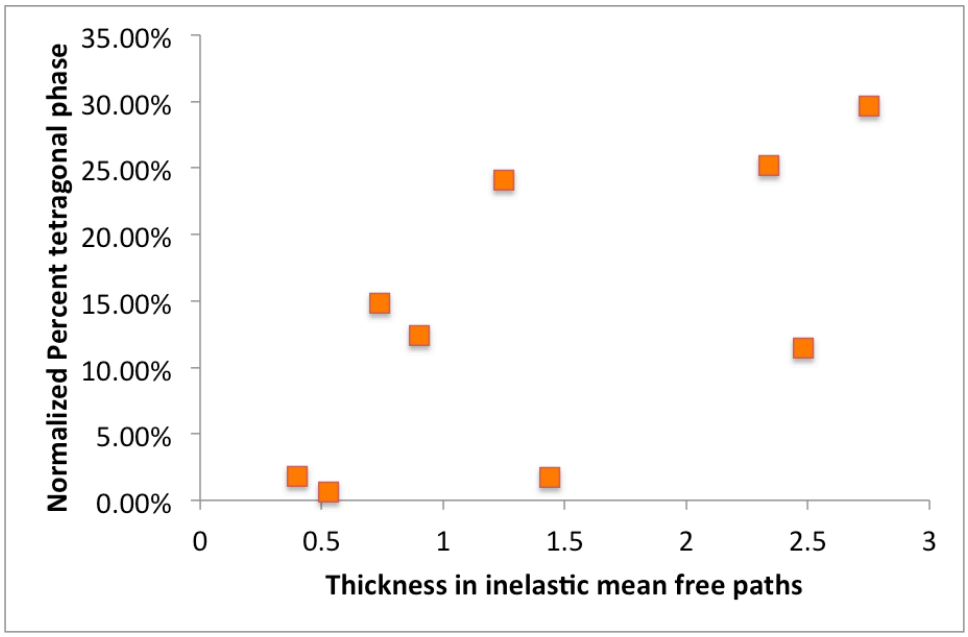

Figure 48: Percentage of tetragonal phase ZrO_2 as a function of a relative sample thickness, showing an increase in tetragonal phase as sample relative thickness increases.

Sample thickness can be converted to nanometers from inelastic mean free paths[143], which using a calculated effective atomic number of 35.71 for ZrO_2 leads to a conversion of 0.1 imfp to approximately 8.39 nm. This conversion relies upon many simplifications, and can have an error of up to 10%[143]. The results shown in figure 47 are indicative of two things. First, the thickness dependence suggests that there is a stress relaxation threshold at a certain thickness, which correlates with a phase transition. This corresponds well with past work, which has shown through modeling[146] and experiment[54,144] that stress can stabilize the tetragonal phase, and that the percentage of

this phase can decrease when the oxide relaxes. Second, the significant variability in reported percentage of tetragonal ZrO_2 phase found in literature could partially attributed to the variability of sample thickness, most notably in very thin samples. For our samples that show a significant amount of tetragonal phase, the location of the tetragonal phase is near the oxide metal interface, and near stress concentrators, which are the expected locations based on a wide range of previous work[22,23,49,81,89].

4.7 Conclusions on Stress Stabilization of Tetragonal ZrO_2

The question of stress stabilization of the tetragonal ZrO_2 phase has been a point of much debate in corrosion of zirconium-based alloys. For oxidized zirconium-based alloys, there is a large range of published values for the tetragonal ZrO_2 phase percentage, and TEM has been a major method of characterizing the phases in the oxide layer. We have shown that the tetragonal phase is indeed stress stabilized, and when using transmission electron microscopy to characterize this phase, care must be used to account for sample relaxation as sample thickness plays a vital role in determining the amount of tetragonal phase present. While the strain was not quantified, it is well known TEM samples relax depending on their thickness[91], and for a stress-stabilized phase such as tetragonal ZrO_2, this relaxation can result in a phase change to the room-temperature stable monoclinic ZrO_2 phase within the oxide. As such, we have shown that through a model sample, there exists a clear transition between monoclinic and tetragonal phase fraction that can be connected to stress stabilization. This further reinforces that the tetragonal phase of ZrO_2 is at least partially stress stabilized, and the cyclic oxidation behavior observed in long-term tests maybe connected to the destabilization of this phase during oxide growth. The implication here is that one must take caution in interpreting

TEM analysis of stress stabilized phases in Zirconium alloys as the very process of creating the sample may be responsible for the phase morphology present in a final TEM sample.

5 Conclusions

This work has pushed the development of a new TEM technique for studying corrosion behavior in samples prepared from bulk metals to fruition. In the process, much valuable insight has been gained, and the limitations of the system have been found.

It has been now shown that in-situ environmental TEM is a viable method for conducting corrosion experiments. A TEM holder was developed, product improvement took place, and is now commercially available. We have shown that using this system, samples can be oxidized to a limited extent, and not immediately though thickness, allowing for the gathering of information about how corrosion proceeds within a material. We have created a process by which a sample is exposed to high humidity environments using the environmental cell, allowing for the study of corrosion, particle agglomeration and collapse, and deliquescence/efflorescence reactions, at realistic atmospheric pressures.

A sample preparation path that allows for easy placement of FIB prepared samples onto thin ceramic membranes has been established, and a new FIB technique by which a FIB-prepared TEM sample can be cross-sectioned has be created. This new technique allows for the investigation of oxide thickness and structure perpendicular to the electron beam path through the sample after in-situ oxidation experiments and can be adapted for other information as well, such as making subsurface, parallel to sample

surface FIB samples. This is of particular interest for subsurface sampling of features such as Nano indents.

In zirconium-based alloys, we have shown that in-situ TEM oxidized samples compare well with those oxidized in an autoclave environment and will provide additional insight into the oxidation behavior of these alloys. It has been shown that oxidation at the TEM scale is not simply thin film effects with a different process than bulk oxidation, but rather that similar structures are formed, and helped to confirm the stress stabilization of the tetragonal ZrO_2 phase. We have also shown that while many TEM techniques provide limited information in this regard, using EELS for thickness mapping, especially if further combined with precession electron diffraction in larger grained samples, has the potential to provide a great amount of information about the initial oxidation behavior of an alloy, as well as the effect of varying crystal orientations and possibly features such as precipitates or grain boundaries.

The effects of sample preparation on the stability of tetragonal ZrO_2 has been investigated, and it has been found that using TEM to quantify the percentage of tetragonal ZrO_2 within an oxidized sample will result in considerable variation depending upon the sample thickness. This has also further confirmed that the tetragonal ZrO_2 phase is at least partially stress stabilized, and not wholly stabilized by grain size.

6 Future Work

Moving forward, the work I have done allows for great advancements in a number of fields. In oxidation of zirconium-based alloys, now that a method that allows for comparison of relative corrosion rates during initial oxidation has been developed, future studies can be done to establish the effect of crystal orientation on oxidation rate to

help determine if there is a preferential texture for reduced corrosion, which would in turn open the door to adventures in grain boundary engineering of zirconium-based alloys. In addition, studies can be done to compare the oxidation performance of different alloys, which may inform the field to the effect of certain alloying elements on initial behavior, allowing for improved alloys to be developed.

Perhaps more importantly, because this technique to study oxidation behavior uses small FIB prepared samples, samples that have been irradiated in-reactor can be prepared and compared to non-irradiated samples to study the effect of real irradiation conditions on corrosion performance. By using this in-situ TEM technique, concerns about radioactive contamination of large autoclave systems are effectively removed, which is one of the major barriers to studying the effects of irradiation on corrosion performance.

This technique is not material dependent, except for oxidizing conditions, which I have laid the groundwork for finding in other systems, and this means that the technique can be utilized across the entire oxidation field, which may give new insight into oxidaiton processes in new alloys such as high entropy alloys. In these alloys this technique may allow for the determination of the effect of various alloying elements on oxide structure, as well as when combined with my FIB cross section technique allow for investigation to the uniformity of composition in the initial oxide layers.

Further development based on my initial work in the area of high humidity environments will also provide another new technique for multiple fields. After further work is done to confirm the humidity levels inside the microscope and a system for better control of the relative humidity on the inlet side is created, this technique can be used for wide variety of applications. Oxidation studies can be conducted in both dry gas and wet

environments, with heat applied to better replicate a steam like environment, in order to study directly the effect of environment on the first stages of oxidation. The effect of humidity levels on soot particles and their collapse/densification can be studied in detail, along with the determination of the factors relevant to the collapse of these particles, and how this process occurs, which has never before been possible. Moving further, this high humidity system would possibly have great interest in the field of polymers, as not only could samples be imaged at atmospheric pressure, thus eliminating high vacuum effects, but also for studying how certain polymers react to the presence of water, and exactly how these processes occur.

1. DOE-NERAC. ***A Technology Roadmap for Generation IV Nuclear Energy Systems***. (2002). doi:GIF-002-00

2. Idaho National Lab. ***DOE-NE Light Water Reactor Sustainability Program and EPRI Long-Term Operations Program – Joint Research and Development Plan***. (2015). doi:INL/EXT-12-24562 Revision 2

3. Whitmarsh, C. L. ***Review of Zircaloy-2 and Zircaloy-4 Properties Relevant to N.S. Savannah Reactor Design***. **4500,** (1962).

4. Holt, M., Campbell, R. J. & Nikitin, M. B. ***Fukushima Nuclear Disaster***. (2012).

5. Peng, Q., Gartner, E., Busby, J. T., Motta, A. T. & Was, G. S. Corrosion Behavior of Model Zirconium Alloys in Deaerated Supercritical Water at 500°C. ***Corrosion* 63,** 577–590 (2007).

6. Watanabe, T. An approach to grain boundary design for strong and ductile polycrystals. ***Res Mech.* 11,** 47–94 (1984).

7. Watanabe, T. Grain boundary engineering: historical perspective and future prospects. ***J. Mater. Sci.* 46,** 4095–4115 (2011).

8. Schuh, C. A., Kumar, M. & King, W. E. Analysis of grain boundary networks and their evolution during grain boundary engineering. ***Acta Mater.* 51,** 687–700 (2003).

9. Lin, P. & Wright, S. Grain Boundary Engineering for Improved Resistance to Intergranular Degradation. 5–8

10. Bechtle, S., Kumar, M., Somerday, B. P., Launey, M. E. & Ritchie, R. O. Grain-boundary engineering markedly reduces susceptibility to intergranular hydrogen embrittlement in metallic materials. ***Acta Mater.* 57,** 4148–4157 (2009).

11. Read, W. T. & Shockley, W. Dislocation Models of Crystal Grain Boundaries. ***Phys. Rev.* 78,** 275–289 (1950).

12. Reed-Hill, R. E. & Abbaschian, R. ***Physical Metallurgy Principles***. (PWS Publishing Company, 1973).

13. Tan, L., Sridharan, K. & Allen, T. R. Altering Corrosion Response via Grain Boundary Engineering. ***Mater. Sci. Forum* 595–598,** 409–418 (2008).

14. Manikrishna, K. ***et al.*** Resistance to hydride formation in zirconium: An emerging possibility. ***Acta Mater.* 54,** 4665–4675 (2006).

15. Ambat, R., Aung, N. N. & Zhou, W. Evaluation of microstructural effects on

corrosion behaviour of AZ91D magnesium alloy. ***Corros. Sci.* 42,** 1433–1455 (2000).

16. Jeong, Y. H., Lee, K. O. & Kim, H. G. Correlation between microstructure and corrosion behavior of Zr–Nb binary alloy. ***J. Nucl. Mater.* 302,** 9–19 (2002).

17. Cox, B. Some thoughts on the mechanisms of in-reactor corrosion of zirconium alloys. ***J. Nucl. Mater.* 336,** 331–368 (2005).

18. Ploc, R. A. Transmission Electron Microscopy of Thin (<2000A) Thermally Formed ZrO_{2} Films. ***J. Nucl. Mater.* 28,** 48–60 (1968).

19. Ni, N. ***et al.*** How the crystallography and nanoscale chemistry of the metal / oxide interface develops during the aqueous oxidation of zirconium cladding alloys. ***Acta Mater.* 60,** 7132–7149 (2012).

20. Zinkle, S. J. & Was, G. S. Materials challenges in nuclear energy. ***Acta Mater.* 61,** 735–758 (2013).

21. Allen, T. R., Konings, R. J. M. & Motta, A. T. Corrosion of Zirconium Alloys. ***Compr. Nucl. Mater.* 5,** 49–68 (2012).

22. Chollet, M. ***et al.*** Synchrotron X-ray diffraction investigations on strains in the oxide layer of an irradiated Zircaloy fuel cladding. ***J. Nucl. Mater.* 488,** 181–190 (2017).

23. Kurpaska, L., Jozwik, I. & Jagielski, J. Study of sub-oxide phases at the metal-oxide interface in oxidized pure zirconium and Zr-1.0% Nb alloy by using SEM / FIB / EBSD and EDS techniques. ***J. Nucl. Mater.* 476,** 56–62 (2016).

24. Motta, A. T. Waterside corrosion in zirconium alloys. ***Jom* 63,** 59–63 (2011).

25. Marquis, E. A. ***et al.*** Nuclear reactor materials at the atomic scale. ***Mater. Today* 12,** 30–37 (2009).

26. Yueh, H. K. ***et al.*** Improved ZIRLO Cladding Performance through Chemistry and Process Modifications. in ***Zirconium in the Nuclear Industry: Fourteenth International Symposium*** (eds. Rudling, P. & Kammenzind, B.) 330–346 (American Society for Testing and Materials, 2005).

27. Kim, H. H. ***et al.*** High-temperature Oxidation Behavior of Zircaloy-4 and Zirlo in Steam Ambient. ***J. Mater. Sci. Technol.* 26,** 827–832 (2010).

28. Andersson, T. & Versterlund, G. Beta Quenching of Zircaloy Cladding Tubes in Intermediate or Final Size-Methods to Improve Corrosion and Mechanical Properties. in ***Zirconium in the Nuclear Industry: Fifth Conference, ASTM STP 754*** (ed. Franklin, D. G.) 75–95 (American Society for Testing and Materials,

1982).

29. Bangaru, N. V., Busch, R. A. & Schemel, J. H. Effect of Beta Quenching on Microstructure and Corrosion of Zircaloys. in ***Zirconium in the Nuclear Industry: Seventh International Symposium, ASTM STP 939*** (eds. Adamson, R. B. & Van Swam, L. F. P.) 341–363 (American Society for Testing and Materials, 1987).

30. Yao, M. Y. ***et al.*** A superior corrosion behavior of Zircaloy-4 in lithiated water at 360°C/18.6MPa by β-quenching. ***J. Nucl. Mater.*** **374,** 197–203 (2008).

31. Glavicic, M. G. Development and Application of Techniques for the Microstructural Characterization of Hydrogen Permeability in Zirconium Oxides. (McGill University, 1998).

32. Proff, C., Abolhassani, S., Dadras, M. M. & Lemaignan, C. In situ oxidation of zirconium binary alloys by environmental SEM and analysis by AFM, FIB, and TEM. ***J. Nucl. Mater.*** **404,** 97–108 (2010).

33. Fruchart, D., Convert, P. & Lelievre, G. Characterisation by neutron diffraction in high temperature pressurised water of the surface corrosion and hydrogen embrittlement of zircaloy-4. **347,** 288–294 (2002).

34. Woolsey, I. S. & Morris, J. R. A Study of Zircaloy-2 Corrosion in High Temperature Water Using Ion Beam Methods. ***Corrosion*** **37,** 575 (1981).

35. Abolhassani, S., Dadras, M., Leboeuf, M. & Gavillet, D. In situ study of the oxidation of Zircaloy-4 by ESEM. ***J. Nucl. Mater.*** **321,** 70–77 (2003).

36. Li, H., Glavicic, M. G. & Szpunar, J. a. A model of texture formation in ZrO2 films. ***Mater. Sci. Eng. A*** **366,** 164–174 (2004).

37. Bakradze, G., Jeurgens, L. P. H., Acartürk, T., Starke, U. & Mittemeijer, E. J. Atomic transport mechanisms in thin oxide films grown on zirconium by thermal oxidation, as-derived from \n 18O-tracer experiments. ***Acta Mater.*** **59,** 7498–7507 (2011).

38. Grovenor, R. ***et al.*** Mechanisms of Oxidation of Fuel Cladding Alloys Revealed by High Resolutino APT, TEM and SIMS Analysis. in ***Materials Research Society Symposium*** **1383,** 101–112 (2012).

39. Clark, B. G. ***et al. Final LDRD Report : Nanoscale Mechanisms in Advanced Aging of Materials During Storage of Spent ' High Burnup ' Nuclear Fuel***. (2013).

40. Coleman, C. E. & Hardie, D. The hydrogen embrittlement of α-zirconium—A review. ***J. Less Common Met.*** **11,** 168–185 (1966).

41. Yilmazbayhan, A. ***et al.*** Structure of zirconium alloy oxides formed in pure water studied with synchrotron radiation and optical microscopy: relation to corrosion rate. ***J. Nucl. Mater.*** **324,** 6–22 (2004).

42. Polatidis, E. ***et al.*** Residual stresses and tetragonal phase fraction characterisation of corrosion tested Zircaloy-4 using energy dispersive synchrotron X-ray diffraction. ***J. Nucl. Mater.*** **432,** 102–112 (2013).

43. Motta, A. T., Yilmazbayhan, A., Comstock, R. J., Partezana, J. & George, P. Microstructure and Growth Mechanism of Oxide Layers Formed on Zr Alloys Studied with Micro-Beam Synchrotron Radiation. ***J. ASTM Int.*** **2,** 1–26 (2012).

44. Yilmazbayhan, A., Breval, E., Motta, A. T. & Comstock, R. J. Transmission electron microscopy examination of oxide layers formed on Zr alloys. ***J. Nucl. Mater.*** **349,** 265–281 (2006).

45. Garner, A. ***et al.*** The microstructure and microtexture of zirconium oxide films studied by transmission electron backscatter diffraction and automated crystal orientation mapping with transmission electron microscopy. ***Acta Mater.*** **80,** 159–171 (2014).

46. Moya, J. S. ***et al.*** Zirconium Oxide Film Formation on Zircaloy by Water Corrosion. ***Acta Mater.*** **48,** 4749–4754 (2000).

47. Hutchinson, B. & Hallstadius, L. Oxidation of Zircaloy-2 studied using a wedge-shaped specimen. ***J. Nucl. Mater.*** 437–443 (2013).

48. Lakshmi, N., Yoo, H.-I. & Martin, M. Oxidation Kinetics of Zirconium Examined by In Situ X-ray Diffraction. ***J. Electrochem. Soc.*** **160,** C136–C141 (2013).

49. Motta, A. T. ***et al.*** Zirconium alloys for supercritical water reactor applications: Challenges and possibilities. ***J. Nucl. Mater.*** **371,** 61–75 (2007).

50. Motta, A. T., Couet, A. & Comstock, R. J. Corrosion of Zirconium Alloys Used for Nuclear Fuel Cladding. ***Annu. Rev. Mater. Res.*** **45,** 150504161757009 (2015).

51. Yardley, S. S. ***et al.*** An investigation of the oxidation behaviour of zirconium alloys using isotopic tracers and high resolution SIMS. ***J. Nucl. Mater.*** 436–443 (2013). doi:10.1016/j.jnucmat.2013.07.053

52. Gosmain, L., Valot, C., Ciosmak, D. & Sicardy, O. Study of stress effects in the oxidation of Zircaloy-4. ***Solid State Ionics*** **141–142,** 633–640 (2001).

53. Lin, J. ***et al.*** Analysis of zirconium oxide formed during oxidation at 623 K on Zr – 2 . 5Nb and Zircaloy-4. ***Mater. Sci. Eng. A*** **381,** 104–112 (2004).

54. Spengler, D. J., Motta, A. T., Bajaj, R., Seidensticker, J. R. & Cai, Z.

Characterization of Zircaloy-4 corrosion films using microbeam synchrotron radiation. ***J. Nucl. Mater.*** **464,** 107–118 (2015).

55. Qin, W., Nam, C., Li, H. L. & Szpunar, J. A. Tetragonal phase stability in ZrO 2 film formed on zirconium alloys and its effects on corrosion resistance. ***Acta Mater.*** **55,** 1695–1701 (2007).

56. Hulme, H. ***et al.*** An X-ray absorption near-edge structure (XANES) study of the Sn L3 edge in zirconium alloy oxide films formed during autoclave corrosion. ***Corros. Sci.*** **105,** 202–208 (2015).

57. Sundell, G., Thuvander, M. & Andrén, H. O. Tin clustering and precipitation in the oxide during autoclave corrosion of Zircaloy-2. ***J. Nucl. Mater.*** **456,** 409–414 (2015).

58. Schefold, J., Lincot, D., Ambard, a. & Kerrec, O. The Cyclic Nature of Corrosion of Zr and Zr-Sn in High-Temperature Water (633 K). ***J. Electrochem. Soc.*** **150,** B451 (2003).

59. Barberis, P. & Frichet, A. Characterization of Zircaloy-4 oxide layers by impedance spectroscopy. ***J. Nucl. Mater.*** **273,** 182–191 (1999).

60. Dong, Y., Motta, A. T. & Marquis, E. a. Atom probe tomography study of alloying element distributions in Zr alloys and their oxides. ***J. Nucl. Mater.*** **442,** 270–281 (2013).

61. Broy, Y., Garzarolli, F., Seibold, A. & Van Swam, L. F. Influence of Transition Elements Fe, Cr, and V on Long-Time Corrosion in PWRs. in ***Zirconium in the Nuclear Industry : Twelfth International Symposium, ASTM STP 1354*** (eds. Sabol, G. P. & Moan, G. D.) 609–622 (American Society for Testing and Materials, 2016).

62. Hashimoto, H., Naiki, T., Eto, T. & Fujiwara, K. High temperature gas reaction specimen chamber for an electron microscope. ***Jpn. J. Appl. Phys.*** **7,** 946–952 (1968).

63. Wagner, J. B., Cavalca, F., Damsgaard, C. D., Duchstein, L. D. L. & Hansen, T. W. Exploring the environmental transmission electron microscope. ***Micron*** **43,** 1169–1175 (2012).

64. Kamino, T. ***et al.*** Development of a gas injection/specimen heating holder for use with transmission electron microscope. ***J. Electron Microsc. (Tokyo).*** **54,** 497–503 (2005).

65. Lee, T. C., Dewald, D. K., Eades, J. a., Robertson, I. M. & Birnbaum, H. K. An environmental cell transmission electron microscope. ***Rev. Sci. Instrum.*** **62,** 1438 (1991).

66. Robertson, I. M. & Tetter, D. Controlled environment transmission electron microscopy. ***Microsc. Res. Tech.*** **42,** 260–9 (1998).

67. Gai, P. L. Development of Wet Environmental TEM (Wet-ETEM) for In Situ Studies of Liquid-Catalyst Reactions on the Nanoscale. ***Microsc. M croanalysis*** 21–28 (2002).

68. Boyes, E. D. & Gai, P. L. Environmental high resolution electron microscopy and applications to chemical science. ***Ultramicroscopy*** **67,** 219–232 (1997).

69. Gai, P. L. Developments in in situ environmental cell high-resolution electron microscopy and applications to catalysis. ***Top. Catal.*** **21,** 161–173 (2002).

70. Swift, J. A. & Brown, A. C. An environmental cell for the examination of wet biological specimens at atmospheric pressure by transmission scanning electron microscopy. ***J. Phys. E.*** **3,** 924–6 (1970).

71. Sharma, R. & Weiss, K. Development of a TEM to study in situ structural and chemical changes at an atomic level during gas-solid interactions at elevated temperatures. ***Microsc. Res. Tech.*** **42,** 270–80 (1998).

72. Sharma, R. An Environmental Transmission Electron Microscope for in situ Synthesis and Characterization of Nanomaterials. ***J. Mater. Res.*** **20,** 1695–1707 (2011).

73. Creemer, J. F. ***et al.*** Atomic-scale electron microscopy at ambient pressure. ***Ultramicroscopy*** **108,** 993–8 (2008).

74. Jonge, N. De & Ross, F. M. Electron microscopy of specimens in liquid. ***Nat. Nanotechnol.*** **6,** 695–704 (2011).

75. Evans, J. E., Jungjohann, K. L., Browning, N. D. & Arslan, I. Controlled growth of nanoparticles from solution with in situ liquid transmission electron microscopy. ***Nano Lett.*** **11,** 2809–13 (2011).

76. Mehraeen, S. ***et al.*** A (S) TEM Gas Cell Holder with Localized Laser Heating for In-Situ Experiments. ***Microsc. Microanal.*** (2012).

77. Sharma, R. & Crozier, P. A. in ***Environmental Transmission Electron Microscopy in Nanotechnology*** 531–565

78. Westerman, R. E. High-Temperature Oxidation of Zirconium and Zircaloy-2 in Oxygen and Water Vapor. ***J. Electrochem. Soc.*** **111,** 140 (1964).

79. Rosa, C. J. Oxidation of Zirconium- A Critical Review of Literature. ***J. Less-Common Met.*** **16,** 173–201 (1968).

80. Dali, Y. ***et al.*** Corrosion kinetics under high pressure of steam of pure zirconium and zirconium alloys followed by in situ thermogravimetry. ***J. Nucl. Mater.*** **426,** 148–159 (2012).

81. Gong, W. ***et al.*** Grain morphology and crystal structure of pre-transition oxides formed on Zircaloy-4. ***Corros. Sci.*** **74,** 323–331 (2013).

82. Suzuki, M. & Kawasaki, S. Oxidation of Zircaloy Cladding in Air. ***J. Nucl. Mater.*** **140,** 32–43 (1986).

83. Pétigny, N., Barberis, P., Lemaignan, C., Valot, C. & Lallemant, M. In situ XRD analysis of the oxide layers formed by oxidation at 743 K on Zircaloy 4 and Zr–1NbO. ***J. Nucl. Mater.*** **280,** 318–330 (2000).

84. Causey, R., Cowgill, D. & Nilson, R. ***Review of the Oxidation Rate of Zirconium Alloys***. (2005).

85. Porter, D. A., Easterling, K. E. & Sherif, M. Y. ***Phase Transformations in Metals and Alloys***. (CRC Press, 2009).

86. Ross, I. M. ***et al.*** Electron energy-loss spectroscopy (EELS) studies of an yttria stabilized TZP ceramic. **24,** 2023–2029 (2004).

87. McComb, D. W. Bonding and electronic structure in zirconia pseudopolymorphs investigated by electron energy-loss spectroscopy. ***Phys. Rev. B*** **54,** 7094–7102 (1996).

88. Yao, M. Y. ***et al.*** The effect of final annealing after β-quenching on the corrosion resistance of Zircaloy-4 in lithiated water with 0.04M LiOH. ***J. Nucl. Mater.*** **435,** 63–70 (2013).

89. Godlewski, J. & Cadalbert, R. A New Method for Residual Stress Distribution Analysis of Corroded Zircaloy-4 Cladding. in ***International Symposium on Material Chemistry in Nuclear Environment*** 1–9 (1992).

90. Jones, D. A. ***Principles and Prevention of Corrosion***. (Prentice Hall, 1996).

91. Treacy, M. M. J. & Gibson, J. M. The effects of elastic relaxation on transmission electron microscopy studies of thinned composition-modulated materials. ***J. Vac. Sci. Technol.*** **4,** 1458–1466 (1986).

92. Lukatskaya, M. R. ***et al.*** Cation Intercalation and High Volumetric Capacitance of Two-Dimensional Titanium Carbide. ***Science (80-.).*** **2,** (2013).

93. Naguib, M. ***et al.*** Two-Dimensional Nanocrystals Produced by Exfoliation of Ti 3 AlC 2. ***Adv. Mater.*** **23,** 4248–4253 (2011).

94. Naguib, M. ***et al.*** Two-Dimensional Transition Metal Carbides. ***ACS Nano* 6,** 1322–1331 (2012).

95. Fujishima, A. TiO2 photoelectrochemistry and photocatalysis. **213,** 8656 (2001).

96. Zhang, H., Chen, G. & Bahnemann, D. W. Photoelectrocatalytic materials for environmental applications. ***J. Mater. Chem.*** 5089–5121 (2009). doi:10.1039/b821991e

97. Lai, Z. ***et al.*** A new insight into regulating high energy facets of rutile TiO2. ***J. Mater. Chem. A* 1,** 4182–4185 (2013).

98. Hong, Z. & Wei, M. Layered titanate nanostructure and their derivatives as negative electrode materials for lithium-ion batteries. ***J. Mater. Chem. A* 1,** 4403–4414 (2013).

99. Gratzel, M. Photoelectrochemical cells. ***Nature* 414,** (2001).

100. Chen, J. S., Liu, H., Qiao, S. Z. & Lou, X. W. (David). Carbon-supported ultra-thin anatase TiO 2 nanosheets for fast reversible. ***J. Mater. Chem.*** 5687–5692 (2011). doi:10.1039/c0jm04412a

101. Akpan, U. G. & Hameed, B. H. Applied Catalysis A : General The advancements in sol – gel method of doped-TiO 2 photocatalysts. ***Appl. Catal. A* 375,** 1–11 (2010).

102. Li, G., Bono, A., Krishnaiah, D. & Collin, J. G. Preparation of titanium dioxide photocatalyst loaded onto activated carbon support using chemical vapor deposition : A review paper. ***J. Hazard. Mater.* 157,** 209–219 (2008).

103. Barsoum, M. W. ***et al.*** One-step synthesis of nanocrystalline transition metal oxides on thin sheets of disordered graphitic carbon by oxidation of MXenes. ***Chem. Commun.* 50,** (2014).

104. Onuma, A., Kiyono, H., Shimada, S. & Desmaison, M. High temperature oxidation of sintered TiC in an H2O-containing atmosphere. ***Solid State Ionics* 172,** 417–419 (2004).

105. Shimada, S. & Kozeki, M. Oxidation of TiC at low temperatures. ***J. Mater. Sci.* 27,** 1869–1875 (1992).

106. Ghassemi, H. ***et al.*** In situ environmental transmission electron microscopy study of oxidation of two-dimensional Ti 3 C 2 and formation of carbon-supported TiO 2. ***J. Mater. Chem. A* 2,** 14339 (2014).

107. Popovicheva, O. ***et al.*** Water interaction with hydrophobic and hydrophilic soot particles. ***Phys. Chem. Chem. Phys.* 10,** 2332–2344 (2008).

108. Rayez, Collignon, Picaud & Hoang. Clustering of water molecules on model soot particles: an ab initio study. ***Comput. Lett.*** **1,** 277–287 (2005).

109. Giordano, M. & Espinoza, C. Experimentally measured morphology of biomass burning aerosol and its impacts on CCN ability. 1807–1821 (2015). doi:10.5194/acp-15-1807-2015

110. Khalizov, A. F. ***et al.*** Formation of highly hygroscopic soot aerosols upon internal mixing with sulfuric acid vapor. ***J. Geophys. Res. Atmos.*** **114,** 1–15 (2009).

111. Zhang, R. ***et al.*** Variability in morphology , hygroscopicity , and optical properties of soot aerosols during atmospheric processing. **105,** 10291–10296 (2008).

112. Semeniuk, T. A., Wise, M. E., Martin, S. T., Russell, L. M. & Buseck, P. R. Hygroscopic behavior of aerosol particles from biomass fires using environmental transmission electron microscopy. 259–273 (2007). doi:10.1007/s10874-006-9055-5

113. Freney, E. J., Martin, S. T. & Buseck, P. R. Deliquescence and Efflorescence of Potassium Salts Relevant to Biomass-Burning Aerosol Particles. ***Aerosol Sci. Technol.*** **43,** 799–807 (2009).

114. Adams, J. R. & Merz, A. R. Hygroscopicity of Fertilizer Materials and Mixtures. ***Ind. Eng. Chem.*** **21,** 305–307 (1929).

115. Wise, M. E., Biskos, G., Martin, S. T., Russell, L. M. & Buseck, P. R. Phase Transitions of Single Salt Particles Studied Using a Transmission Electron Microscope with an Environmental Cell. ***Aerosol Sci. Technol.*** **39,** 849–856 (2005).

116. Wise, M. E., Martin, S. T., Russell, L. M. & Buseck, P. R. Water Uptake by NaCl Particles Prior to Deliquescence and the Phase Rule. 281–294 (2008). doi:10.1080/02786820802047115

117. Harris, V. G. ***et al.*** High coercivity cobalt carbide nanoparticles processed via polyol reaction: a new permanent magnet material. ***J. Phys. D. Appl. Phys.*** **43,** 165003 (2010).

118. Koch, G. H., Michiel, B. P. H., Thompson, N. G., Virmani, Y. P. & Payer, J. H. ***Corrosion Costs and Preventive Strategies in the United States***. ***Nace International*** (2002).

119. Harlow, W., Ghassemi, H. & Taheri, M. L. Determination of the initial oxidation behavior of Zircaloy-4 by in-situ TEM. ***J. Nucl. Mater.*** **474,** 126–133 (2016).

120. Luo, L. ***et al.*** Scripta Materialia In-situ transmission electron microscopy study of surface oxidation for Ni – 10Cr and Ni – 20Cr alloys. ***SMM*** **114,** 129–132 (2016).

121. Zhou, G. & Yang, J. C. Temperature effect on the Cu2O oxide morphology created by oxidation of Cu(0 0 1) as investigated by in situ UHV TEM. ***Appl. Surf. Sci.*** **210,** 165–170 (2003).

122. Yang, J. C., Kolasa, B., Gibson, J. M. & Yeadon, M. Self-limiting oxidation of copper. ***Appl. Phys. Lett.*** **73,** 2841–2843 (1998).

123. Giannuzzi, L. a. & Stevie, F. a. A review of focused ion beam milling techniques for TEM specimen preparation. ***Micron*** **30,** 197–204 (1999).

124. Platt, P. ***et al.*** A study into stress relaxation in oxides formed on zirconium alloys. ***J. Nucl. Mater.*** **456,** 415–425 (2015).

125. Viladot, D. ***et al.*** Orientation and phase mapping in the transmission electron microscope using precession-assisted diffraction spot recognition: State-of-the-art results. ***J. Microsc.*** **252,** 23–34 (2013).

126. Humphreys, F. J. Characterisation of fine-scale microstructures by electron backscatter diffraction (EBSD). ***Scr. Mater.*** **51,** 771–776 (2004).

127. Arslan, I., Marquis, E. A., Homer, M., Hekmaty, M. A. & Bartelt, N. C. Towards better 3-D reconstructions by combining electron tomography and atom-probe tomography. ***Ultramicroscopy*** **108,** 1579–1585 (2008).

128. De Gabory, B., Dong, Y., Motta, A. T. & Marquis, E. A. EELS and atom probe tomography study of the evolution of the metal/oxide interface during zirconium alloy oxidation. ***J. Nucl. Mater.*** **462,** 304–309 (2015).

129. Hu, J. ***et al.*** Identifying suboxide grains at the metal – oxide interface of a corroded Zr – 1 . 0 % Nb alloy using (S) TEM , transmission-EBSD and EELS. **69,** 35–42 (2015).

130. Sun, M., Wu, X., Han, E. & Rao, J. Microstructural characteristics of oxide scales grown on stainless steel exposed to supercritical water. ***Scr. Mater.*** **61,** 996–999 (2009).

131. Ghosh, S., Kumar, M. K. & Kain, V. Applied Surface Science High temperature oxidation behavior of AISI 304L stainless steel — Effect of surface working operations. ***Appl. Surf. Sci.*** **264,** 312–319 (2013).

132. Huntz, A. M., Reckmann, A., Haut, C. & Herbst, M. Oxidation of AISI 304 and AISI 439 stainless steels. **447,** 266–276 (2007).

133. Wang, S. G., Sun, M., Han, H. B., Long, K. & Zhang, Z. D. The high-temperature oxidation of bulk nanocrystalline 304 stainless steel in air. ***Corros. Sci.*** **72,** 64–72 (2013).

134. Kim, J. ***et al.*** The role of grain boundaries in the initial oxidation behavior of austenitic stainless steel containing alloyed Cu at 700 ° C for advanced thermal power plant applications. ***Corros. Sci.*** **96,** 52–66 (2015).

135. ***Introduction to Focused Ion Beams: Instrumentation, Theory, Techniques and Practice***. (Springer Science+Business Media, Inc., 2004).

136. Rooyen, I. J. Van. ***EBSD Characterization of Tubular Cladding Plasticity after Bend Testing : A Feasibility Study***. (2013).

137. Akhiani, H. & Szpunar, J. A. Effect of surface roughness on the texture and oxidation behavior of Zircaloy-4 cladding tube. ***Appl. Surf. Sci.*** (2013). doi:10.1016/j.apsusc.2013.08.137

138. Gabory, B. De & Motta, A. T. Structure of Zircaloy-4 Oxides Formed During Autoclave Corrosion. in ***ANS LWR Fuel Performance Meeting, TopFuel 2013*** (2013).

139. Platt, P., Frankel, P., Gass, M., Howells, R. & Preuss, M. Finite element analysis of the tetragonal to monoclinic phase transformation during oxidation of zirconium alloys. ***J. Nucl. Mater.*** **454,** 290–297 (2014).

140. Kim, H. G., Kim, T. H. & Jeong, Y. H. Oxidation characteristics of basal (0002) plane and prism (11-20) plane in HCP Zr. ***J. Nucl. Mater.*** **306,** 44–53 (2002).

141. Adamson, R., Garzolli, F., Cox, B., Strasser, A. & Rudling, P. ***Corrosion Mechanisms in Zirconium Alloys***. (2007).

142. Egerton, R. F. Application of electron energy-loss spectroscopy to the study of solid catalysts. **21,** 185–190 (2002).

143. Egerton, R. F. & Cheng, S. C. Measurement of local thickness by electron energy-loss spectroscopy. ***Ultramicroscopy*** **21,** 231–244 (1987).

144. Qin, W., Nam, C., Li, H. L. & Szpunar, J. A. Effects of local stress on the stability of tetragonal phase in ZrO 2 film. ***J. Alloys Compd.*** **437,** 280–284 (2007).

145. Godlewski, J., Bouvier, P., Lucazeau, G. & Fayette, L. Stress Distribution Measured by Raman Spectroscopy in Zirconia Films Formed Oxidation of Zr-Based Alloys. in ***Zirconium in the Nuclear Industry: Twelfth International Symposium ASTM STP 1354*** (eds. Sabol, G. P. & Moan, G. D.) 877–900 (American Society for Testing and Materials, 2000).

146. Glazoff, M. V., Tokuhiro, A., Rashkeev, S. N. & Sabharwall, P. Oxidation and hydrogen uptake in zirconium, Zircaloy-2 and Zircaloy-4: Computational thermodynamics and ab initio calculations. ***J. Nucl. Mater.*** **444,** 65–75 (2014).

Vita

Wayne Harlow received his bachelor's degree from the University of Illinois in Materials Science and Engineering in 2012, and received his master's degree in Materials Science and Engineering from Drexel University in 2014. During his PhD work at Drexel, he presented at a number of conferences, including: M&M 2014 and 2015, TMS 2015 and 2016, MS&T 2015 and 2016, and is authored on several publications. In addition, he was active within the department, assisting with visit days and instructing for both MATE 100 Transmission electron microscopy lab and MATE 366, an undergraduate materials processing course.